

Experimentelle Physik

**Spin-wave instabilities
on the
nanoscale**

Inaugural-Dissertation
zur Erlangung des Doktorgrades
der Naturwissenschaften im Fachbereich Physik
der Mathematisch-Naturwissenschaftlichen Fakultät
der Westfälischen Wilhelms-Universität Münster

vorgelegt von
Henning Ulrichs

aus
Oldenburg

2014

Dekan:	Prof. Dr. M. Donath
Erster Gutachter:	Prof. Dr. S. O. Demokritov
Zweiter Gutachter:	Prof. Dr. D. Grundler
Tag der mündlichen Prüfung:
Tag der Promotion:

Kurzfassung

Die vorliegende Arbeit beschäftigt sich mit der Anregung und Beobachtung von Spinwelleninstabilitäten. Bei einer Spinwelle handelt es sich um eine niederenergetische, wellenartige Anregung eines magnetischen Systems. Als solche werden hier wenige Nanometer dicke Filme aus einem metallischen Ferromagneten betrachtet, welche zudem lateral strukturiert sind. Ausreichend starke, tangential statische Magnetfelder richten die Magnetisierung in diesen Systemen weitgehend homogen aus. Die räumliche Begrenzung führt zu einer Quantisierung der erlaubten Wellenzahlen, und somit zu einer Diskretisierung des Spektrums. Zur experimentellen Beobachtung der Spinwellen wurde der physikalische Effekt der Brillouin-Lichtstreuung ausgenutzt. Mittels der hierbei angewandten, beugungsbeugten Mikroskopie konnte frequenz-, orts-, und zeitaufgelöste Information über magnetische Dynamik gewonnen werden.

Alle experimentellen Versuche wurden bei Raumtemperatur durchgeführt. Ohne weitere Manipulation gehorchen die dynamischen Amplituden aller Moden dann einer thermischen Gleichgewichtsverteilung. Instabilität einer bestimmten Spinwellenmode bedeutet, dass ein Übermaß an Energie in diesem spektralen Zustand akkumuliert. Notwendige Voraussetzung, um einen solche nichtthermische Besetzung aufrecht zu halten, ist eine Überkompensation der magnetischen Verluste. Um dem System Energie zuzuführen wurden zwei verschiedene Ansätze verfolgt.

Bei der induktiven Methode wurden magnetische Wechselfelder mit Hilfe von Mikrowellenströmen erzeugt. Liegt das Wechselfeld senkrecht zum statischen Feld, so kann eine magnetische Schwingung mit der Frequenz der Mikrowellen direkt erzwungen werden. Homogene dynamische Felder koppeln hierbei am effizientesten an die fundamentale Schwingungsmode. Es wird gezeigt, dass bei hinreichend großer dynamischer Amplitude der primär angeregten Mode, Moden höherer Ordnung instabil werden. Bei noch höherer dynamischer Amplitude kommt es zu einer Überbevölkerung eines spektralen Zustands, dessen Frequenz unterhalb des Frequenzbandes linearer Spinwellen liegt. Die Instabilität beruht in beiden Fällen auf einer Wechselwirkung zwischen verschiedenen Spinwellenmoden. Das zweite diskutierte Experiment zeigt, wie Instabilität durch parametrische Anregung direkt erzwungen werden kann. In diesem Fall liegt das dynamische Feld parallel zum statischen Feld.

Im dritten experimentellen Teil dieser Arbeit wird gezeigt, wie durch eine lokal begrenzte Injektion von Spinströmen in einen magnetischen Film das thermische Gleichgewicht der Spinwellen gestört, und letztlich eine spezielle Mode

destabilisiert werden kann. Diese Mode zeichnet sich durch eine charakteristische laterale Größe von unter 100 Nanometern aus. Desweiteren liegt auch bei dieser Instabilität die Frequenz unterhalb des Frequenzbandes linearer Spinwellen. Der Spinstrom wurde hierbei durch den sogenannten Spin-Hall-Effekt in einem nichtmagnetischen Leiter erzeugt. Im Gegensatz zur induktiven Methode ist dieser Ansatz nur schwach spektral selektiv. Insbesondere vor der Instabilität wird allen Moden gleichzeitig Energie zugeführt. Die lokale Spinstrominjektion impliziert die Anwesenheit von Strahlungsverlusten. Der Intuition widersprechend sind es gerade diese Verluste, welche die Instabilität ermöglichen. Die Untersuchung der Eigenschaften der instabilen Mode wurde ergänzt durch mikromagnetische Simulation. Alle Befunde sind im Einklang mit dem maßgeblichen theoretischen Modell, welches die Instabilität einer sogenannten stehenden Spinwellenkugel vorhersagt.

Abstract

The topic of this thesis is the excitation and observation of spin-wave instabilities. A spin wave is a low-energetic wave-like excitation of a magnetic system. As such, ferromagnetic films with a thickness of a few nanometres will be considered, which are in addition laterally confined. An almost homogeneous orientation of the magnetization is guaranteed by sufficiently strong, tangential static magnetic fields. The spatial confinement leads to a quantization of the wave numbers, which implies a discrete spectrum. The physical effect of Brillouin-Light scattering is exploited for the experimental investigations. The here applied diffraction-limited microscopic approach provides frequency-, space-, and time-resolved information about magnetization dynamics.

All experiments discussed here were conducted at ambient temperature. Without further manipulations, the dynamic amplitudes of all modes then obey a thermal equilibrium distribution. Instability of a particular spin-wave mode implies that excess energy accumulates in this state. As a necessary prerequisite to sustain such a non-thermal population, the dynamic magnetic losses have to be overcompensated. To pump energy into the magnetic system, two approaches were followed.

The inductive method relies on alternating, dynamic magnetic fields, induced by microwave currents. When this dynamic field is oriented perpendicular to the static field, the magnetic system can then be forced to oscillate with the frequency of the microwaves. Homogeneous dynamics fields couple most efficiently to the fundamental spin-wave mode. It will be shown that when the primarily pumped mode's amplitude exceeds a certain level, higher order modes go unstable. At

even larger amplitude, an overpopulation of a specific spin-wave mode appears, which is not part of the linear spin-wave spectrum. In both of the two former cases, the instability is a consequence of interaction between different spin-wave modes. The second experiment demonstrates how a spin-wave instability can be directly provoked by means of parametric excitation. In this case the dynamic field is parallel to the static field.

In the third experimental part of this thesis, I will show how a locally confined injection of a spin current into a magnetic film can perturb the thermal equilibrium of the spin waves, and can finally lead to the instability of a particular mode. This mode has a characteristic lateral size of less than 100 nanometres. The frequency of this mode lies below the frequencies of linear spin waves. The spin-current itself was generated inside a non-magnetic conductor, by the so-called spin-Hall effect. In contrast to the inductive method, this approach to achieve instability has only a weak spectral selectivity. In particular prior to the onset of instability, energy is pumped into all possible modes. The local spin-current injection implies the existence of radiative losses. Counterintuitively, the radiation enables the instability. Micromagnetic simulation is performed to assist the experimental investigation of the unstable mode. All findings agree well with the relevant theoretical model, which predicts the instability of a so-called spin-wave bullet.

Contents

1	Introduction	1
2	Theoretical considerations	4
2.1	Spin waves in a thin magnetic film	4
2.2	Spin-wave modes in a confined element	9
2.2.1	Classifying different modes	9
2.2.2	Ferromagnetic Resonance in a confined element	11
2.2.3	Exemplary spectrum	12
2.3	Spin-wave instabilities	14
2.3.1	Classical instability processes	15
2.3.2	Spin current-induced instability	23
3	Methods	31
3.1	Micro-focus Brillouin Light Scattering	31
3.1.1	Focussing optics	34
3.1.2	Interferometer	36
3.1.3	Micro BLS measurement of magnetization dynamics in confined structures	37
3.2	Micromagnetic simulation	39
3.2.1	Eigenmode spectra	40
3.2.2	Characterizing excited systems	40
4	Experiments	41
4.1	Non-linear scattering processes in confined elements	41
4.1.1	The sample	42
4.1.2	Eigenmode spectrum	42
4.1.3	Suhl instability	44
4.1.4	Overpopulation	51
4.1.5	Discussion	61
4.2	Parametric instability	66
4.2.1	The sample	66

4.2.2	Eigenmode spectrum	67
4.2.3	Experimental results	68
4.2.4	Discussion	75
4.3	Spin current-induced instability	78
4.3.1	The sample	78
4.3.2	Thermal fluctuations under the influence of STT	83
4.3.3	Instability	88
4.3.4	Micromagnetic model	93
4.3.5	Discussion	101
5	Supplement	104
5.1	Thermal magnetic fluctuations in a device with uniform spin current injection	104

Tables with acronyms and symbols

Notation in text	Meaning
BEC	Bose-Einstein condensate
BLS	Brillouin Light Scattering
FMR	Ferromagnetic Resonance
FWHM	Full width at half maximum
LLGS	Landau-Lifshitz-Gilbert-Slonczewski equation
Py	Permalloy. Alloy of the ferromagnetic 3d transition metals $\text{Ni}_{80}\text{Fe}_{20}$. Polycrystalline, no significant anisotropy, $A = 1.3 \times 10^{-6} \text{ erg/cm}$, $4\pi M_0 = 10 \text{ kG}$, $\alpha = 0.008$, $\gamma/2\pi = 2.8 \text{ MHz/Oe}$.
SEM	Scanning Electron Microscopy
SHE	Spin-Hall effect
SHNO	Spin-Hall nano-oscillator
STT	Spin-transfer torque
YIG	Yttrium iron garnet, a ferrimagnetic insulator with small damping $\alpha < 10^{-4}$.

Table 1: Commonly used acronyms. The given material parameters for Py are those which are typically assumed for micromagnetic modelling [33].

Notation in text	Meaning
A	Exchange constant
α	Gilbert damping constant
$f = \frac{\omega}{2\pi}$	Frequency
g	g-factor
$\gamma = g\mu_B/\hbar$	Gyromagnetic ratio
Γ	Losses
H and h	Static and dynamic magnetic field
I	Current
I_{BLS}	BLS intensity
l_{ex}	Exchange length
λ	Wave length
M_0	Saturation magnetization
\mathbf{M}	Magnetization vector
m_i	Dynamic part of the magnetization, Cartesian component $i = x, y, z$
NA	Numerical aperture
ν	Growth rate of an unstable spin-wave mode
P_{mw}	Microwave power
$P(\omega)$	Fourier power at frequency ω
ϕ	Angle of magnetic precession
ϕ_H	Spin-Hall angle
χ	Susceptibility
$\omega = 2\pi f$	Radial frequency
t	Thickness

Table 2: Commonly used symbols.

Chapter 1

Introduction

In the last decade physicists investigating magnetization dynamics strongly participated in establishing spintronics [131] as a new paradigm for future information technologies. In a spintronic device, the electron's spin is exploited as an additional degree of freedom in order to save or process information. The discovery of the giant magneto-resistance by Grünberg and Fert in 1988 [6, 10], and the subsequent, rapid implementation of this effect in read-heads of magnetic storage devices by IBM, is an unprecedented example for the development of a commercially successful spintronic application.

As an emerging sub field of spintronics, magnonics [97, 70] aims to utilize the spin-magnetic moment carried by spin waves to convey information. In the beginning, in particular tailoring the spin-wave dispersion by patterning a magnetic material [67, 96] was in the focus of this research. In analogy to photonic crystals,[58] the notion of a magnonic crystal was introduced for such structures. Since a few years, scientific interest in this field continuously increases. For example, in 2013 more than 100 publication directly referred to magnonics as a topic. This is also caused by the fact that today, a wider scope is envisaged by the notion of magnonics:

'...includes not only the traditional branches of spin waves research, but also the area of quantum properties of magnons, physics of artificial magnonic crystals, magnetic excitations at nano-scale, and ultrafast magnetization dynamics.'

(from the preface of 'Magnonics' [32])

The richness of the physics of magnetism constantly bears new opportunities for research and practical applications. In recent years, effects related to spin-orbit coupling have aroused much attention. As an example, after the discovery of magnetic skyrmions in 2009 [92, 102], it was recently demonstrated [42] that they might be useful as information carriers. Magnetic skyrmions are caused by

the Dzyaloshinskii-Moriya interaction, which can arise at interfaces between ferromagnets and non-magnetic metals with strong spin-orbit coupling [41]. The spin-Hall effect (SHE) [35, 52, 53], which is exploited in some experiments presented in this thesis, is also a consequence of spin-orbit coupling. The spin-Hall effect can be utilized in order to generate a pure spin current. When injected into a ferromagnet, such spin-currents exert a spin-transfer torque (STT) on the magnetization in the ferromagnet. From a phenomenological point-of-view, the STT can act like negative damping. Thereby the SHE provides practical means for controlling magnetic damping [4, 77, 26, 38] in magnonic devices. In the spin-Hall nano-oscillator (SHNO) [28, 78], the spin current generated by the SHE is strong enough to fully compensate magnetic losses: a spin-wave instability is induced. The operational principle of this device, and the unstable dynamic modes will be elucidated in detail in this thesis.

Already before the spin-Hall effect as a method to generate spin currents was explored, spin-transfer devices exploiting spin-polarized currents were in the focus of attention [61, 65, 106, 103, 25]. Their appeal in the context of spintronics derives from their potential as nano-sized microwave source, or in the more specific context of magnonics as local spin-wave emitters [79, 126]. Spin transfer oscillators combine two challenging aspects: they have nano-scale dimensions, and such devices typically display magnetization dynamics with very large amplitude. A typical dynamic mode which goes unstable in such oscillators is the standing spin-wave bullet [111]. The dynamic amplitude of this mode is so large that the magnetization is locally reversed. One particular experimental drawback (circumvented by the SHNO) is that spin-transfer devices operating with spin-polarized charge currents do not provide optical access to the active area.

In such a situation it can be instructive to investigate a simplified system, made of the same magnetic material, i.e. thin permalloy (Py, $\text{Ni}_{80}\text{Fe}_{20}$) films. In comparison with other metallic ferromagnets, magnetic damping of Py is relatively small ($\alpha = 0.008$). Therefore it is widely used as a working medium in all kinds of magnonic devices: spin-torque oscillators (including the SHNO), [106, 68, 86, 103, 25, 28] magnonic crystals [96, 71, 120, 16], spin-wave logic circuits [63]. Spatial confinement of the dynamics is realized by patterning the film into elements which have a characteristic lateral size of less than $1\text{ }\mu\text{m}$. The confinement enables a very efficient inductive excitation. Large dynamic amplitudes, comparable to the situation encountered in spin-torque devices, can be achieved, while optical access is guaranteed. Furthermore, the inductive excitation allows to precisely control the intensity of magnetization dynamics, and especially acts only on few spectral states simultaneously. A significant part of this thesis is devoted to

the investigation of spin-wave instabilities in confined elements, appearing at different degrees of non-linearity. Note that from the very beginnings of experimental research in magnetization dynamics in the 1950s, experimentalists were faced with such phenomena [12, 13]. The theories [3, 118] developed to explain their findings are carefully adapted in order to understand the experiments discussed here.

The optical technique of micro-focus Brillouin Light Scattering [29], which is applied for the experimental investigations presented in this thesis, is limited by diffraction. When confronted with dynamics on smaller spatial scales, micromagnetic simulation is performed to assist in the interpretation of experimental data. The presentation of the experiments in this thesis follows the chronological order, in which the experiments were conducted and published.

Chapter 2

Theoretical considerations

2.1 Spin waves in a thin magnetic film

Due to the exchange interaction, the spin system in a ferromagnetic material is not balanced. On a microscopic scale the resulting net spins spontaneously align when the temperature drops below the Curie point. On a macroscopic scale a domain structure will be established, which minimizes the free energy. Only when the ferromagnetic material is exposed to a sufficiently strong magnetic field \mathbf{H} , the spins in all domains align to the latter, as shown in Figure 2.1(a). The wave-like excitations (see 2.1(b)) of this equilibrium state are called spin waves. An early derivation of the dispersion law given by Bloch in 1930 [11] included only exchange interaction. One well-known result of this theory is Bloch's $T^{3/2}$ law, which explains the temperature dependence of the magnetization by spin waves. Ten years later, Holstein and Primakoff [54] published a theory including dipolar interaction. Both of these early theories rely on a picture of localized spins.

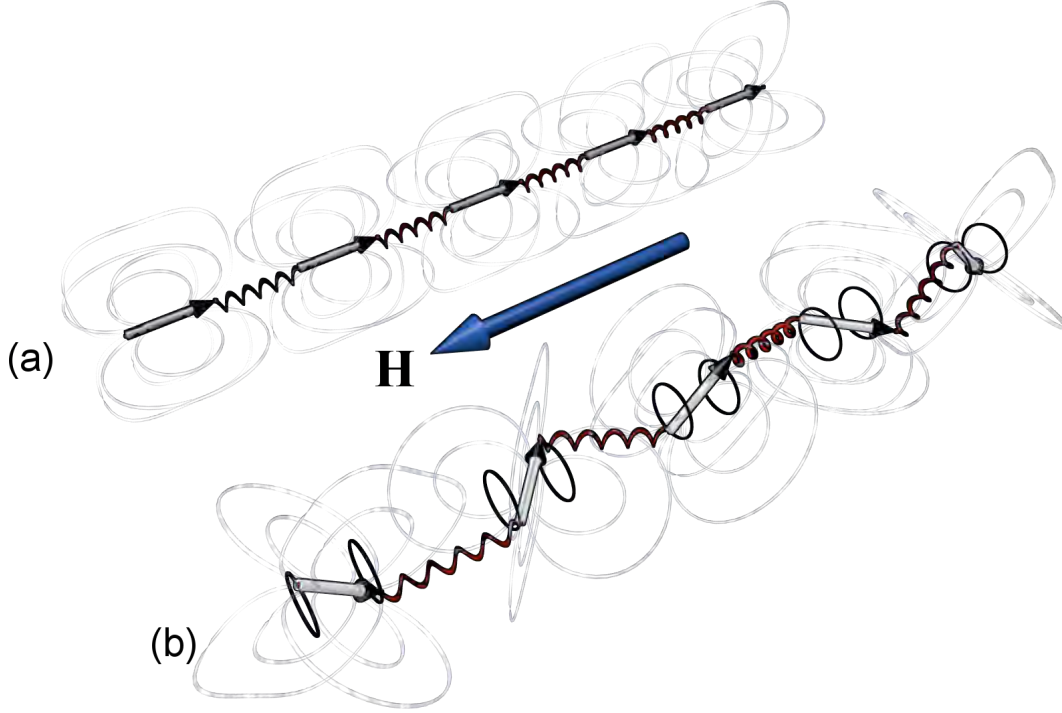


Figure 2.1: One dimensional section through a ferromagnetically ordered material and its excitation. (a) A chain of spins exposed to a magnetic field \mathbf{H} in equilibrium. (b) Wave-like excitation of the spins. Red spirals represent the short-range exchange force between adjacent spins, blue lines the long-range dipolar field induced by each spin.

In the micromagnetic approach followed by Herring and Kittel [51], a continuously differentiable vector field \mathbf{M} - the magnetization - instead of individual spins \mathbf{s} is considered. The magnetization is microscopically constituted by the spin-magnetic moments $\mathbf{m}_s = -|g| \mu_B \mathbf{s} / \hbar$. The dynamics is described by the Landau-Lifshitz equation (see pp. 278 [74]):

$$\dot{\mathbf{M}} = -\gamma \mathbf{M} \times \mathbf{H}_{eff}. \quad (2.1)$$

This equation is analogous to the torque equation of a gyroscope, and describes a precessional motion of \mathbf{M} . The field torque $\tau_H = -\gamma \mathbf{M} \times \mathbf{H}_{eff}$ refers to the effective field $\mathbf{H}_{eff} = \mathbf{H} + \mathbf{H}_{ani} + \mathbf{H}_d + \mathbf{H}_{ex} + \dots$ which comprises all relevant energetic contributions. Usually Zeemann, anisotropy, dipolar and exchange energy are considered.

In the simple case of a small-angle uniform magnetization precession ($\mathbf{k} = 0$) in an isotropic bulk ferromagnet, the external field \mathbf{H} provides the only energetic

contribution. Then $H_{eff} = H$, and accordingly

$$\omega_0 = \gamma H. \quad (2.2)$$

When passing from this translationally invariant bulk system to a tangentially magnetized, extended film with finite thickness, in addition the dipolar energy has to be taken into account. E.g. for the uniform precession mode a dynamic dipolar field $\mathbf{h}_{d\perp}$ arises, whenever the dynamic magnetization points out-of-plane during the course of the precession. Then the divergence of the magnetization at the top and bottom surface gives rise to fictitious magnetic charges. The corresponding Kittel formula [66]

$$\omega_0 = \gamma \sqrt{H(H + 4\pi M_0)} \quad (2.3)$$

differs from the bulk equivalent Eq.(2.2). For finite wave lengths λ the dipolar field also contains a tangential dynamic contribution, which is spatially anisotropic. In the magneto-static approximation, this field reads $\mathbf{h}_{d\parallel} \approx -\frac{4\pi}{k^2} \mathbf{k}(\mathbf{m} \cdot \mathbf{k})$. E.g. for waves with $\mathbf{H} \parallel \mathbf{k} \perp \mathbf{m}$, this contribution vanishes. Taking into account this field, but yet neglecting exchange, the dispersion theory by Damon and Eshbach [21] describes so-called magneto-static waves. Note that although ferromagnetism is based upon the exchange effect, the corresponding energetic contribution to the spin-wave dispersion dominates over the dipolar contribution only for wave lengths smaller than the exchange length¹ $l_{ex} = \sqrt{\frac{A}{2\pi M_0^2}}$. For Py the standard parameter in table 1 yield $l_{ex} \approx 6$ nm. If $\lambda < l_{ex}$, but larger than the lattice constant, and the exchange is isotropic, the dispersion is quadratic in \mathbf{k} . Especially when describing such waves as quasi-particles, the notion of a magnon instead of a spin wave is commonly used.

In this thesis, the spin waves are a mixture of exchange and magneto-static waves. The case of a tangentially magnetized thin film with thickness t is of particular interest. Spin waves in this system propagate in-plane, characterized by a two-dimensional wave vector \mathbf{k} . The calculation of the dipole-exchange spin-wave spectrum [22, 60] is rather complicated. Here, I will only sketch the assumptions typically made in the theoretical descriptions. The starting point is the linearised LL equation. In the Maxwell equations, the magneto-static approximation is made. The electro-magnetic boundary conditions are complemented by exchange boundary conditions [104]. Note that the final dispersion inherits the anisotropy of the dipolar contribution.

¹ The notion of exchange length is not well-defined in literature. I follow the definition according to Eq. 3 in [1].

For spin-waves with $\lambda > t$, the mode profile across the thickness direction is approximately uniform. The theory developed by Kalinikos and Slavin [60] describes in zeroth order² such spin waves. The dispersion reads:

$$\omega(\mathbf{k}) = \sqrt{A_k^2 - B_k^2}, \quad (2.4)$$

with the abbreviations (see [129])

$$A_k = \omega_H + l_{ex}^2 \omega_M k^2 - 1/2 \omega_M (P_0(1 - \sin^2 \phi) - 1), \quad (2.5)$$

and

$$B_k = 1/2 \omega_M (P_0(1 + \sin^2 \phi) - 1). \quad (2.6)$$

Note that only for tangential magnetization, and in-plane propagating waves as considered here, B_k is strictly real. In the preceding expressions $\omega_H = \gamma H$, $\omega_M = \gamma 4\pi M_0$, $P_0 = \frac{1-e^{-kt}}{kt}$, and ϕ is the angle between \mathbf{H} and \mathbf{k} . Figure 2.2 shows the spin-wave spectrum of a $t = 10$ nm thick Py film, tangentially magnetized by a field $H = 900$ Oe. For $\mathbf{k} \parallel \mathbf{H}$, the dispersion runs through a minimum for increasing k . The negative tangent at $k = 0$ physically implies a negative group velocity, as expressed in the commonly used term Backward-Volume mode (BWVM). The BWVM dispersion branch hosts the mode with lowest frequency $\omega_{bottom} = \min \{\omega(\mathbf{k})\}$ (open red circle in 2.2 (a) and (b)). For $\mathbf{k} \perp \mathbf{H}$, the dispersion instead grows monotonously with k . In theory [21] this so-called Damon-Eshbach (DE) modes have a non-uniform mode profile, described by an exponential localization at the top or bottom surface. Since the characteristic length scale for the localization is proportional to the wave length λ , this feature practically vanishes for $\lambda \gg t$.

² In lowest order, which is evaluated here only, the mode profiles are assumed to be constant across the thickness of the film. This simplifies the implementation of the electro-magnetic boundary conditions in the calculation. As a result, instead of having to find numerical solutions of implicit equations (which has to be done in the Damon-Eshbach theory [21]), the dispersion law is given explicitly for every in-plane angle of \mathbf{k} with respect to \mathbf{H}_{ext} . In [60] exchange boundary conditions are taken into account. Calculations for thin Py usually give good results assuming no pinning. Spin waves of higher perpendicular order have in thin films frequencies $\omega_n(k) \gg \omega_0$. In the experiments considered in this thesis, such waves are not important.

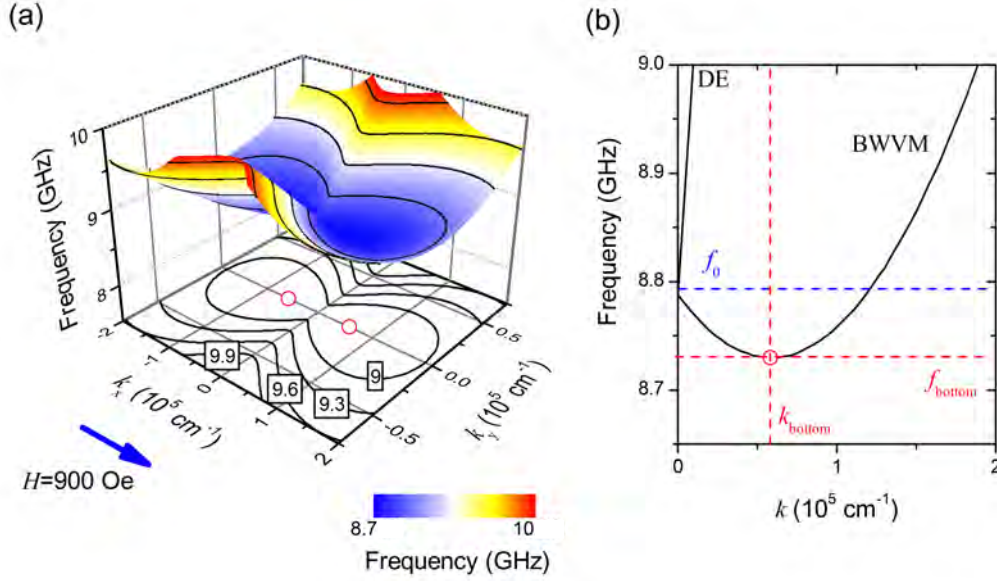


Figure 2.2: Spin-wave dispersion for a thin, tangentially magnetized film (10 nm thick Py, $H = 900$ Oe). (a) Three-dimensional spin-wave manifold. The projection on the k_x - k_y -plane shows iso-frequency curves for the indicated frequencies (in GHz). (b) One-dimensional sections along the k_x axis ($k_y=0$, dispersion shows BWVM spin waves), and along the k_y axis ($k_x=0$, dispersion shows DE spin waves).

To allow losses, the LL equation can be augmented by the Gilbert torque [43]

$$\tau_G = \frac{\alpha}{M_0} \mathbf{M} \times \dot{\mathbf{M}}, \quad (2.7)$$

in order to obtain the LLG equation. For small α and small dynamic amplitudes, the solution $m(t) \propto \exp i\omega t$ of the undamped, linearised LL equation can be inserted in the linearised LLG equation as a first approximation. Then the form of the linearised LL equation can be regained by substitution of $H + i\alpha\omega/\gamma$ for the field H . With the same substitution, also the dispersion law Eq.(2.4) can still be used. The dispersion can be regarded as a function of $\omega_H = \gamma H$, and be expanded in this parameter, if $\alpha\omega(\omega_H) \ll \omega_H$:

$$\omega(\omega_H + i\alpha\omega) \approx \omega(\omega_H) + i\alpha\omega(\omega_H) \frac{\partial\omega}{\partial\omega_H}. \quad (2.8)$$

At this point one can either directly identify $\omega_r = \alpha\omega(\omega_H) \frac{\partial\omega}{\partial\omega_H}$ with an imaginary part of the frequency. The relaxation rate ω_r describes temporal decay, or the spectral linewidth. Alternatively, one can define a complex wave number $k' + ik''$.

The inverse of the imaginary wave number $\xi = k''^{-1}$ has the physical meaning of a propagation length. If $k'' \ll k'$, one can express ξ via ω_r and the group velocity $\mathbf{v} = \nabla_{\mathbf{k}}\omega(\mathbf{k})$:

$$\xi = \frac{|\mathbf{v}|}{\omega_r}. \quad (2.9)$$

2.2 Spin-wave modes in a confined element

In this section, a theoretical description of magnetization dynamics in laterally confined magnetic elements, made of thin magnetic films is presented. The description in particular applies to (sub-)micrometer sized, tangentially magnetized Py structures, with a thickness of a few nanometres. A rectangular Py element with side lengths l_x and l_y , whose thickness t is much smaller than the lateral dimensions, will now be considered as a generic model. Exposed to a sufficiently strong, tangential external magnetic field $\mathbf{H} \parallel \mathbf{e}_x$, this element can be magnetized to saturation, at least in a central part. One can formally introduce a magnetic charge density $\rho_M = -\nabla_x \mathbf{M}$. In an idealized case $\mathbf{M} \parallel \mathbf{H}$ everywhere inside the sample, and $\rho_M \propto \delta(x - \frac{l_x}{2}) + \delta(x + \frac{l_x}{2})$. From this charge density, a tangential static dipolar field $\mathbf{H}_d \parallel \mathbf{e}_x$ arises, which is spatially non-uniform[57] in non-ellipsoidal geometries like the rectangular dot. Since \mathbf{H}_d opposes the magnetization, it is also called demagnetizing field.

2.2.1 Classifying different modes

When the aspect ratio $t/l_x \ll 1$, one can distinguish two sets of eigenmodes: center modes, with strong dynamic amplitudes in the center, and edge modes, which are localized close to the outer edges which are orthogonal to \mathbf{H} (at $x \pm \frac{l_x}{2}$).

To calculate the eigenfrequencies of the center modes, one can neglect the regions of strong field reduction close to the edges at $\pm \frac{l_x}{2}$, and approximate the internal field by its average value (over y and z) in the center at $x = 0$:

$$\mathbf{H}_{int} \approx \frac{1}{tl_y} \int_0^t dz \int_{-\frac{l_y}{2}}^{\frac{l_y}{2}} dy \mathbf{H}_{int}(0, y, z). \quad (2.10)$$

When using plane waves $\exp(ik_x x + ik_y y)$ as basis functions, the lateral confinement leads to a quantization of the wave vector

$$\mathbf{k}_{mn} = \left[\frac{(m+1)\pi}{l_x}, \frac{(n+1)\pi}{l_y} \right]. \quad (2.11)$$

Here, we have applied the Dirichlet boundary condition of vanishing dynamic amplitude at the lateral edges. A more precise treatment should instead incorporate dipolar boundary conditions [48]. Nevertheless, for in-plane sizes much larger than the thickness, these conditions indeed predict a vanishing dynamic amplitude at the edges. The dispersion equation (2.4) for infinitely extended films is applied to compute the eigenfrequencies

$$\omega_{mn} = \omega(k_{mn}, H_{int}). \quad (2.12)$$

The frequencies of edge modes ω_e can be estimated by evaluating a quantization integral[8], as described in the following. The basic assumption is the local validity of the thin film dispersion law [60]. Since $\partial \frac{H_{int}}{\partial y} \approx 0$, one may assume $k_y = \frac{(n+1)\pi}{l_y}$, as in the case of center modes. In the other direction, the phase φ instead of k_x will be quantized: k_x adapts locally to the internal field. For a given internal field $H_{int}(x)$ (averaged over y and z), the equation $\omega_e = \omega(k_x, \frac{n+1\pi}{l_y}, H_{int}(x))$ can be solved for k_x for every $x \in L_x = [-l_x/2, +l_x/2]$. The edge mode only exists inside two regions $\Lambda_1, \Lambda_2 \subset L_x$ ($\Lambda = \int_{\Lambda_1} dx$), where k_x is not imaginary. It was shown [8] that $k_x(x)[\omega_e, H_{int}]$ obeys a quantization integral condition, when the correct edge mode frequency ω_e is assumed:

$$\varphi_{mn} = \int_{\Lambda_1} k_x(x)[\omega_e, H_{int}]dx = (m+1)\pi \quad (2.13)$$

Similar to the center modes, one can assign a wave number

$$k_{mn} = \sqrt{\left(\frac{(m+1)\pi}{\Lambda}\right)^2 + \left(\frac{(n+1)\pi}{l_y}\right)^2} \quad (2.14)$$

to each index pair mn and edge-mode frequency $\omega_{e,mn}$. Note that edge-mode frequencies related to different indices are often rather close together. Taking into consideration the linewidth caused by damping,³ they usually merge into a band of edge modes.

As the aspect ratio $\frac{t}{l_x}$ increases or the external field is lowered, the inhomogeneity of the internal field extends further and further into the center. Then, the center modes are compressed, and the edge modes are less localized. At a certain point, the distinction between edge and center modes becomes impossible.

³ Typically the losses in the edge regions are larger than inside the element, which further increases the linewidth.

2.2.2 Ferromagnetic Resonance in a confined element

In a Ferromagnetic Resonance experiment, usually the linear response of the dynamic magnetization m_i to an external dynamic field $\mathbf{h} \perp \mathbf{H}$ is probed.⁴ In a confined element, each center and edge mode is an independent resonance mode, which contributes to the susceptibility $\chi(\omega) = \sum_{mn} \chi_{mn}(\omega)$ with a factor

$$\chi_{mn}(\omega) = \omega_M \frac{\omega_{mn}}{\omega_{mn}^2 - \omega^2} \quad (2.15)$$

Losses are taken into account by substituting $\omega_H + i\alpha\omega$ for ω_H in $\omega_{mn}(\omega_H)$, as discussed before. The resulting complex frequency $\omega_{mn} + i\omega_{r,mn}$ enters the susceptibility. As usual, we define $\chi_{mn} = \chi'_{mn} - i\chi''_{mn}$. The expansion of the dispersion law provides an explicit form for χ''_{mn} :

$$\chi''_{mn}(\omega) = \omega_M \frac{\omega(\omega_{mn}^2 + (1 + \alpha^2)\omega^2)}{D}, \quad (2.16)$$

with the denominator $D = (\omega_{mn}^2 - (1 + \alpha^2)\omega^2)^2 + 4\omega_{r,mn}^2\omega^2$, and $\omega_{r,mn} = \alpha\omega_{mn} \frac{\partial \omega_{mn}(\omega_H)}{\partial \omega_H}$. When a confined sample is excited by a spatially homogeneous dynamic field h , the power P_{mn} absorbed by a given eigenmode m_{mn} is proportional to

$$P_{mn} \propto \chi''_{mn} h^2 |\hat{m}_{mn}(\mathbf{k} = 0)|^2, \quad (2.17)$$

where $\hat{m}_{mn}(\mathbf{k} = 0)$ is the Fourier coefficient for $\mathbf{k} = 0$ of the mode profile m_{mn} . Since the eigenmodes are spatially confined, this particular coefficient is finite for all symmetric modes, which thus absorb energy. In contrast, spatially antisymmetric modes do not respond to a homogeneous dynamic field h .

When the Gilbert damping constant α is large enough, the frequency spacing $\omega_{mn} - \omega_{m'n'}$ can become smaller than the linewidth of neighbouring modes. With increasing lateral sample size, this situation is reached inevitably. The individual (center) resonance modes become so dense in $\mathbf{k} - \omega$ space that the continuous dispersion of an infinitely extended film is approximated.

⁴ With m_i the dynamic components of the magnetization \mathbf{M} are meant. For small deviations from the equilibrium ($\mathbf{M} \parallel \mathbf{H} = H\mathbf{e}_x$), these are the components m_y and m_z . The resonant-like solution of the LLG equation is a right-hand circularly polarized precessional motion, driven by a right-hand circularly polarized dynamic field. Note that a linearly polarized field (as applied in the experiments) can be written as a superposition of left- and right-hand circularly polarized fields. Here we will neglect the small contribution of a left-hand circularly polarized precession to the susceptibility. Furthermore, the change of the ellipticity ($\frac{|m_y|}{|m_z|}$ is slightly different for different eigenmodes) will be neglected.

2.2.3 Exemplary spectrum

As an example, we will construct the spectrum of a rectangular element with $l_x = l_y = 1\mu\text{m}$ and a thickness of $t = 5\text{nm}$. The external magnetic field of $H = 900\text{Oe}$ points along \mathbf{e}_x . The internal magnetic field $\mathbf{H}_{int} = \mathbf{H} - \mathbf{H}_d$ is analytically computed, using formulas published by Joseph and Schlömann [57], assuming $\mathbf{M} \parallel \mathbf{H}_{ext}$. The dipolar field \mathbf{H}_d is dominated by the component parallel to \mathbf{e}_x , which will from now on be considered only, and is shown in Figure 2.3(a). Figure 2.3(b) shows the dependence of the H_{int} (averaged along y and z) on x . In the center, the internal field is lowered down to 880Oe . As described in the previous section, this value now enters Eq.(2.12). For each pair of indices mn , we assign an effective wave number k_{mn} to the frequency ω_{mn} . This allows to plot the center modes in the dispersion diagram shown in Figure 2.3(c). The local amplitude of the center modes in the framework of our simple model is given by sinusoidal functions (see Figure 2.3(d)).

The frequency and approximate wave number of the principal edge mode (quantization index $m = n = 0$) is computed by evaluating Eq.(2.13). The procedure depends on many assumptions, therefore the determined value of $\omega_{e,00}/2\pi = 8.73\text{GHz}$ should be considered as a coarse approximation only. The result nevertheless reflects the main property of edge modes: due to the low internal field in the region of their existence, their frequency can be below the bottom of the center mode spectrum. The local amplitude $a(x) \propto \sin \int_0^{x'} dx' k_x(x')$ (shown in Figure 2.3(d)) of the edge mode follows from Eq.(2.13).

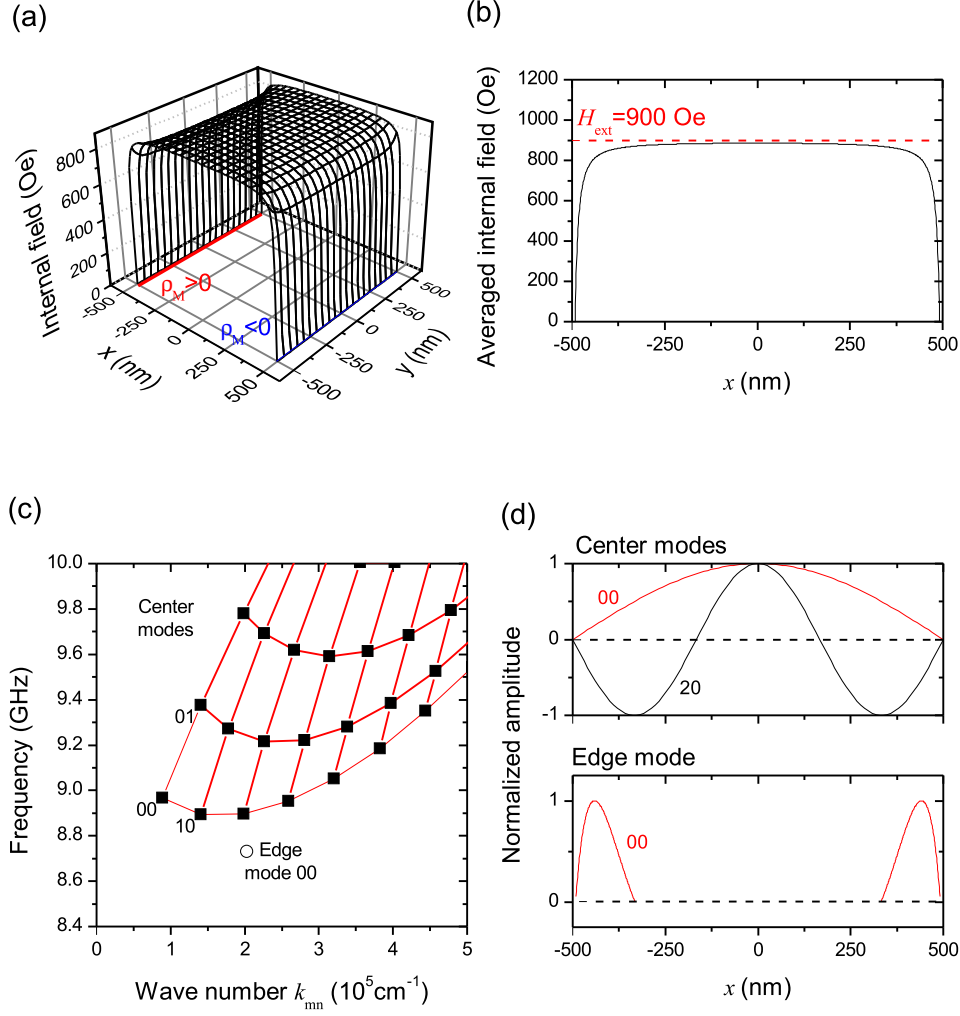


Figure 2.3: (a) Internal magnetic field H_{int} (x -component only) of a confined element ($1000 \text{ nm} \times 1000 \text{ nm} \times 5 \text{ nm}$), made of a Py thin film, exposed to an in-plane external field of $H = 900$ Oe. Red and blue lines indicate the responsible magnetic charge density. (b) Averaged internal field along central x -section. (c) Dispersion diagram showing center modes (filled rectangular dots) and the principal edge mode (open circular dot). The numbers indicate the quantization indices m and n . Red lines connecting center modes with neighbouring indices as a guide to the eye. (d) Mode profiles for center modes 00 and 20 and for the principal edge mode 00.

2.3 Spin-wave instabilities

For the description of spin-wave instability processes, it is convenient to pass from the LLG equation, which considers the magnetization, to rate equations for the normal modes of the system. Following Suhl's semiclassical treatment [118], first one passes from the dynamic magnetic moment m_y, m_z to dimensionless complex variables a_k and a_{-k} :

$$a_k = \frac{1}{M_0} (m_{ky} + im_{kz}) \quad (2.18)$$

$$a_{-k}^* = \frac{1}{M_0} (m_{ky} - im_{kz}) \quad (2.19)$$

Inserting this into the Landau-Lifshitz equation, the linear terms describe two coupled harmonic oscillators:

$$-i\dot{a}_k = A_k a_k + B_k a_{-k} \quad (2.20)$$

The final step is to decouple the two oscillators by means of the third Holstein-Primakoff (Bogoliubov) transformation. Thereby new variables c_k are introduced via:

$$a_k = u_k c_k + v_k c_k^* \quad (2.21)$$

$$a_{-k}^* = v_k^* c_k + u_k c_{-k}^*, \quad (2.22)$$

where $u_k = \frac{1}{\sqrt{2}} \sqrt{\frac{A_k}{\omega_k} + 1}$, and $v_k = \frac{1}{\sqrt{2}} \sqrt{\frac{A_k}{\omega_k} - 1}$. The dispersion is given by $\omega^2(k) = A_k^2 - B_k^2$. (see Eqs. (2.4), (2.5), and (2.6)). Furthermore, if we consider a confined element, the model sketched in chapter 2.2 will be used, introducing quantized wave numbers. The linear equation of motion for the variable c_k without driving force, but including dissipation reads:

$$\dot{c}_k = (i\omega_k - \omega_{rk}) c_k \quad (2.23)$$

$$\dot{c}_{-k}^* = -(i\omega_k - \omega_{rk}) c_{-k}^* \quad (2.24)$$

In these equation, non-linear terms are so far omitted. They will be introduced, depending on the particular kind of instability process under consideration. The onset of a instability of a particular spin-wave mode means that the amplitude $|c_k(t)| \propto \exp(\nu t)$ increases in time ($\nu > 0$). For this purpose, the losses have to be compensated. Usually, the amplitude growth is limited by non-linear processes. In the simplest case, the final dynamic state is a stationary large amplitude

oscillation.

2.3.1 Classical instability processes

Parametric instability

In oscillator theory (see e.g. [94]), one speaks of a parametric excitation, when a system is excited by means of a modulation of an internal parameter, instead of applying an external force. Mathematically, the differential equation describing a parametrically excited system contains a time-dependent coefficient. In the simplest case, a periodic modulation with the modulation frequency being twice of one of the system's eigenfrequencies is applied. If the system-specific parametric resonance condition is fulfilled, the addressed mode gets unstable. First experimental reports date back to Faraday [39] in 1831. Concerning magnetization dynamics, the S-theory [133, 134, 83], developed by Zhakarov, Starobinets and L'vov in the 1970s, should be mentioned here. This theory provides a rigorous mathematical treatment of parametric instability processes in the framework of classical Hamiltonian equations. Although primarily aiming at magnetization dynamics in low-loss YIG, the S-theory is applicable to a broad range of weakly-dissipative Hamiltonian systems. The properties of the above threshold state are in the focus of the S-theory. In particular the amplitude limitation above the threshold is explained by the so-called phase mechanism. In the metallic ferromagnet Py, instead non-linear damping dominates over this process.

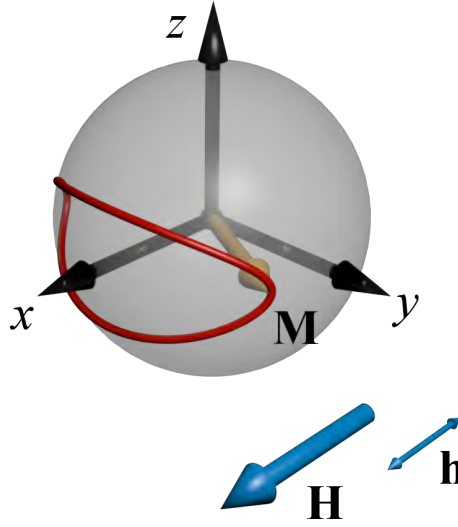


Figure 2.4: Consequence of ellipticity of magnetic precession. When m_y and m_z oscillate with frequency ω , and have different amplitudes, the dynamic component m_x fluctuates with 2ω . Therefore the system can be destabilized by a field $\mathbf{h} \parallel \mathbf{H}$ oscillating with frequency 2ω .

In a magnetic system, the most obvious parameter to implement a parametric excitation is the external field \mathbf{H} . In this section, so-called parallel pumping, realized by a dynamic field $\mathbf{h} \parallel \mathbf{H}$, will be described. To see, why such a field can initiate an instability process, one has to take a look at the ellipticity of magnetic precession. In a tangentially magnetized film without crystalline anisotropy, this ellipticity is a consequence of the dynamic dipolar fields. When during the course of the precession the magnetization vector points out-of-plane (m_z is maximal), the consequently induced magnetic charges at the opposing surface create a strong demagnetizing field. If we shift the precession phase by $\frac{\pi}{2}$, m_y is maximal. For dipolar modes, whose wavelength $\lambda \gg t$, the now tangential demagnetizing field will be much weaker. Referring to the dynamic magnetization $m_{y,z}$ (neglecting the rapidly oscillating exponential factor), the ratio $|\frac{m_y}{m_z}|$ is given by:

$$|\frac{m_y}{m_z}| = |\frac{A_k + B_k}{A_k - B_k}|. \quad (2.25)$$

For small wave numbers k , B_k can be comparable to A_k , and the ellipticity is strongest. For large k , the exchange effect dominates, so that $A_k \gg B_k$ and the magnetic precession becomes circular. Consider now a sample, whose FMR mode with frequency ω_0 is weakly excited, i.e., the dynamic amplitudes $|\frac{m_{y,z}}{M_0}| \ll 1$. Conservation of magnetic moment implies that the magnitude the magnetization vector $|\mathbf{M}|$ is constant. Basic trigonometry and an expansion yields a $2\omega_0$ time-

dependence for the magnetic component m_x ($e_x \parallel \mathbf{H}$):

$$\begin{aligned} m_x &= \sqrt{M_0^2 - m_y^2 \cos^2 \omega t - m_z^2 \sin^2 \omega t} \\ &\approx M_0 - \frac{m_y^2 + m_z^2}{4M_0} + \frac{m_y^2 - m_z^2}{4M_0} \cos(2\omega_0 t). \end{aligned} \quad (2.26)$$

Note that the second term on the right side of Eq. (2.26) describes the effect of negative non-linear frequency shift. The reduced static component $M_{eff} = M_0 - \frac{m_y^2 + m_z^2}{4M_0}$ (effective magnetization) can be substituted for M_0 in the dispersion equation (2.4), to introduce a non-linear correction. For a tangentially magnetized film, $\frac{\partial \omega}{\partial \omega_M} > 0$. Therefore a reduction of the effective magnetization implies a decrease in the frequency. In parallel pumping, the dynamic magnetic component m_x couples to the periodic field $h \propto \cos(\omega_p t)$. Figure 2.4 schematically shows the elliptical precession which enables the parametric excitation. When addressing a particular spin-wave mode c_k ($\omega_p \approx 2\omega_k$), in the equation of motion a coupling term appears:

$$\dot{c}_k = (i\omega_k - \omega_{rk})c_k + i\gamma h \frac{B_k}{\omega_k} c_{-k}^* \quad (2.27)$$

$$\dot{c}_{-k}^* = -(i\omega_k - \omega_{rk})c_{-k}^* - i\gamma h \frac{B_k}{\omega_k} c_k \quad (2.28)$$

From the time-dependence of the term $hc_{-k}^* \propto \exp(i(2\omega_k - \omega_k)t)$ one can directly see, why this term couples to $c_k \propto \exp(i\omega_k t)$. When the energy pumped into the system by the dynamic field h compensates the losses, always a pair of spin waves with equal but opposite wave vectors goes unstable. As a results a standing wave pattern is established. The coupling parameter can be expressed as $V_k = \gamma \frac{B_k}{2\omega_k}$. The growth rate follows from inserting the ansatz $c_k(t) = c_k^0 \exp(\nu t + i\omega_k t)$ into Eq.(2.28):

$$\nu_k(h, \omega_p) = -\omega_{rk} + \sqrt{|hV_k|^2 - \left(\omega_k - \frac{\omega_p}{2}\right)^2}. \quad (2.29)$$

Equating Eq.(2.29) to zero yields the threshold field:

$$h_{th}(\omega_p) = \frac{\sqrt{(\frac{\omega_p}{2} - \omega_k)^2 + \omega_{rk}^2}}{V_k}. \quad (2.30)$$

Recall that in a tangentially magnetized film, the spectrum is generally strongly degenerate (see Figure 2.2). For each frequency $\omega_p > 2\omega_{bottom}$, an iso-frequency curve describes the corresponding subset of degenerate modes, which respond

to the parametric stimulus.⁵ Due to the double mirror symmetry, always four equivalent modes with the same growth rate ν_k can be found ($\mathbf{k} = [k_x; k_y]$, $-\mathbf{k}$, $\mathbf{k}' = [-k_x; k_y]$, \mathbf{k}'). When the pumping frequency is variable, the FMR mode ($k = 0$) has at resonance ($\omega_p = 2\omega_0$) the lowest threshold, and largest growth rate. As soon as this lowest-possible threshold is exceeded, the continuous nature of the spin-wave spectrum implies that always an ensemble of pairs goes unstable simultaneously. Interaction of this ensemble assures that in the later non-linear stage of the parametric growth process, only the pair with largest initial growth rate survives (see chapter 5 in [83]).

We will now take into account lateral confinement. The resonance modes of a confined system can be constructed as a superposition of the aforementioned, four frequency-degenerate partial waves. Compared to the extended film, the now quantized spectrum is strongly depleted. The quantization scheme discussed in section 2.2 can be extended to compute the coupling factor V_{mn} , and the corresponding growth rate ν_{mn} . When a particular mode of a confined sample is excited parametrically, all four partial waves respond equally. The two pairs $(\mathbf{k}_{mn}, -\mathbf{k}_{mn})$, and $(\mathbf{k}'_{mn}, -\mathbf{k}'_{mn})$ are not independent. The boundary conditions fix their relative phases, so that the sinusoidal profile is established.

Similar to the film, the eigenmode with lowest indices $m = n = 0$, which is the FMR mode, has at resonance the smallest threshold h_{th} . When deviating from the resonance condition for the FMR mode ($h > h_{th}$, $\omega_p \neq 2\omega_{00}$), one has to compare $\nu_{mn}(h, \omega_p)$ for all indices mn . Generally, the discreteness of the spectrum enables the existence of several contiguous subsets in the h - ω_p -plane, where only a particular eigenmode is unstable. When several modes are allowed to be unstable simultaneously, their interaction greatly complicates the dynamics. The dynamic state then resembles the situation encountered in extended films. After a transient phase, only the mode with largest growth rate survives. How fast the system settles into the final single mode state is determined by the interaction strength, and by the difference of the growth rates of the competing modes.

⁵ For simplicity, we neglect here how losses broaden this curve.

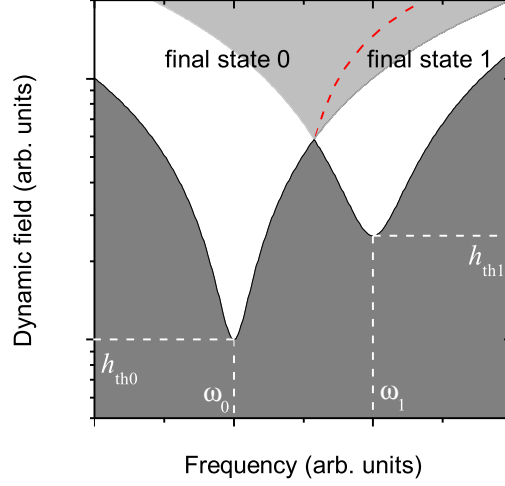


Figure 2.5: Hypothetical dynamic phase diagram of a parametrically excited system with two modes. The continuous line shows the dependence of the threshold field on the half pumping frequency. At resonance ($\omega_p = 2\omega_0$, or $\omega_p = 2\omega_1$), a minimum threshold h_{th0} or h_{th1} has to be exceeded.

To illustrate these theoretical considerations, a dynamic phase diagram of a hypothetical two-mode system is shown in Figure 2.5. In this system $\omega_0 < \omega_1$, $\omega_{r0} < \omega_{r1}$, and $V_0 > V_1$. The curves with $\nu_{0,1}(\omega_p, h) = 0$ (continuous lines in Figure) are defined by Eq.(2.30). A transient phase, where the system is initially not locked to a single mode, can be found in the light gray region. The dashed curve marks the line where $\nu_0 = \nu_1$, which is where an infinitely long transient can be expected.

The existence of these subsets allow the experimental investigation of certain higher order eigenmodes. Recall that in a FMR experiment of a confined sample only spatially symmetric modes respond to the spatially uniform dynamic field \mathbf{h} . With increasing order, the excitation efficiency quickly decreases. Since in parametric excitation, the parallel component $m_x \propto \exp(2i\omega t)$ is addressed, a phase-shift of π in the transverse components $m_{y,z} \propto \exp(i\omega t)$ (as established for adjacent dynamic maxima in antisymmetric modes), shifts the phase of m_x by 2π . With other words, compared to a standard FMR excitation of a confined sample, where $\mathbf{h} \perp \mathbf{H}$, the parametric excitation is free from symmetry restrictions. Therefore antisymmetric modes can be addressed.

Suhl instability

Two unexpected experimental results puzzled experimental physicists, when analysing FMR experiments in the 1950s [12, 13]. In these experiments the pumping frequency ω_p was fixed, and the static field H was swept. The nowadays so-called first order Suhl instability process, also termed subsidiary absorption, manifests in the appearance of a absorption peak for $H < H_{res}$. It was theoretically shown by Anderson and Suhl [3, 118] that this finding is caused by the instability of a pair of spin waves which obey $\omega_p = \omega_k + \omega_{-k}$. This process is only operative, when the dynamic field h exceeds a certain threshold, and when the spin-wave manifold extends to small enough frequencies, as guaranteed by a small enough static field H . If the first order instability is inoperative, the second order Suhl instability can manifest in a saturation of the resonance at large excitation fields. Experimentally, the imaginary part of the susceptibility χ'' begins to decrease with increasing dynamic field h , before the magnetization itself starts to decrease. This effect is caused by the instability of spin-wave mode which is in frequency degenerate with the directly addressed FMR mode:

$$2\omega_p = 2\omega_0 = \omega_k + \omega_{-k} \quad (2.31)$$

The second order Suhl instability is of particular interest in this thesis, and will from now on be referred to as Suhl instability. For circularly polarized dynamic fields h , as e.g. considered by Suhl [118], the equation of motion for the unstable spin-wave mode c_k reads (see Eqs. (10.15) and (10.24) in [47]):

$$\dot{c}_k = (i\omega_k - \omega_{rk})c_k + i\xi_k a_0^2 c_{-k}^*, \quad (2.32)$$

where $\xi_k = \frac{\omega_k + A_k}{\omega_k} (\omega_M \cos \phi_k + a\omega_M k^2)$. The instability takes place because $a_0^2 c_{-k}^* \propto \exp(i(2\omega_p - \omega_p)t)$ can couple to $c_k \propto \exp(i2\omega_p t)$. The threshold field for a particular mode is given by the expression

$$h_{th} = \sqrt{\frac{\omega_{rk}\omega_{r0}^2}{\gamma^2 \xi_k}} \approx \sqrt{\frac{\omega_{r0}^3}{\gamma^2 \omega_M}} \propto \alpha^{3/2} \quad (2.33)$$

Concerning the spin-wave manifold, the iso-frequency curve related to the FMR frequency hosts the potentially unstable modes (see blue line in Figure 2.6). Similar to the case of parametric excitation, the mode with the smallest threshold goes unstable. Note that for a linearly polarized pumping field, which can be written as a sum of left- and right-hand polarized fields, the absolute value of the

threshold field differs by a factor of two. A general derivation of the threshold fields for parallel pumping instability, first, and second order Suhl instability for arbitrary pumping field polarization and orientation, can be found in [95].

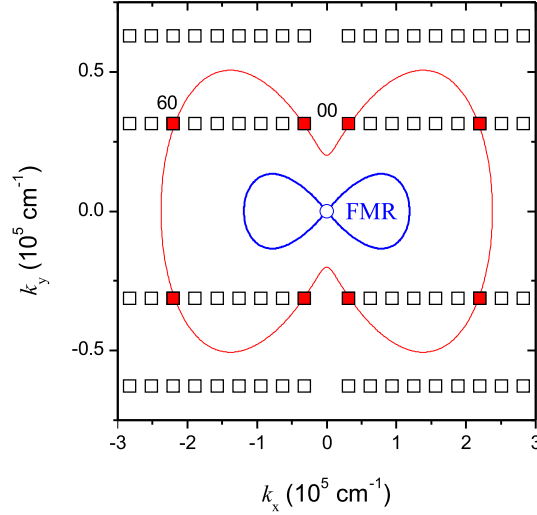


Figure 2.6: Iso-frequency curves for a tangentially magnetized, thin Py film ($t = 10$ nm, $H = 900$ Oe), and quantized wave numbers (open symbols) of a confined sample ($l_x = l_y = 1$ μ m). In case of the extended film, the blue iso-frequency curve for the FMR frequency describes the set of modes which is potentially unstable due to second order Suhl instability. In case of a confined element, modes connected by the red iso-frequency-curve corresponding to the frequency of the first-order eigenmode, are most prone to second order Suhl instability.

So far, no elaborate theory exists for confined samples. There, the pumping field h addresses the first-order principal eigenmode, whose frequency ω_{00} is different from the FMR frequency of the extended film. If the frequency of some higher-order eigenmode $\omega_{mn} = \omega_{00}$, a Suhl-like instability can be expected. The iso-frequency-curve related to ω_{00} can be used as a guide to find potentially unstable modes (see red line in Figure 2.6). Clearly, in a confined sample exact degeneracy of a higher order eigenmode with the first-order mode can a priori not be expected. The situation depicted in Figure 2.6 shows the exceptional case, where the mode with $m = 6$, $n = 0$ is has the same frequency $\omega_{60} = \omega_{00}$ as the mode with $m = n = 0$. Nevertheless, in Py the substantial linewidth of the individual resonance modes enables a non-resonant instability process, which resembles the second order Suhl instability.

From kinetic instability to Bose-Einstein condensation

Experiments carried out with massive YIG samples in the 1980s [72, 73], showed microwave radiation, whose frequency ω_1 is below the frequency ω_0 of the primarily pumped spin wave modes. One explanation [72], based on the framework of S -theory [83], terms the underlying process kinetic instability (KI). As an example, consider a tangentially magnetized film. Let this system be strongly excited at a particular mode with frequency ω_0 . The number $n_0 = |c_0|^2 \gg n_i = |c_i|^2$ of this primary spin-wave mode (PSW) is assumed to be much larger than the number n_i of all other, only thermally excited modes. Four-magnon processes with $2\omega_0 = \omega_1 + \omega_2$ lead to a modification of the effective attenuation $\tilde{\omega}_{r,k_1}$ of these modes.⁶

$$\tilde{\omega}_{r,k_1} = \omega_{r,k_1} - 2\pi \int |T_{1200}|^2 n_0^2 \delta(\omega_1 + \omega_2 - 2\omega_0) \delta(\mathbf{k}_1 + \mathbf{k}_2 - 2\mathbf{k}_0) d^2\mathbf{k}_2, \quad (2.34)$$

where T_{1200} is a matrix element describing four-magnon interaction. The simple consequence of (2.34) is that when the PSW reaches a certain occupation number $n_0 = n_c$, the effective damping of a secondary spin wave mode (SSW) vanishes. Then this SSW becomes unstable, and grows substantially above the thermal level. Note that no phase relation between the participating modes is imposed. The adjective kinetic thus distinguishes this process from a parametric instability, where a particular phase relation is established. The kinetic instability or overpopulation happens first for the mode with the lowest attenuation ω_{r,k_1} . In a tangentially magnetized film, this is the bottom spin-wave mode. The experimentally observed radiation of electro-magnetic waves occurs, when the unstable SSW with relatively small k_1 impinges some inhomogeneity. The high frequency SSW with much larger wave number k_2 cannot radiate energy, because the mismatch between the spin-wave dispersion $\omega(k_2)$ and the free-space photon dispersion is too large. The process described by Eq.(2.34) is of second order. If three-magnon splitting is allowed, also a first-order kinetic instability is possible [81]. A first attempt to adopt the theory of second order KI for confined structures can be found in reference [91].

The theory of kinetic instability is one model to interpret the observed radiation. Around 1990 it was recognized [59, 90] that also a Bose-Einstein condensation (BEC) of magnons can explain the experimentally observed low frequency radiation. By this time, it was assumed that cryogenic temperatures would be necessary. In 2006 it turned out that indeed magnon BECs can be realized at

⁶ Eq.(2.34) is a simplification of Eq.(2) in [72]

room temperature [30]. In this experiments, KI was excluded by a proper choice of the external field.

In the first step, the creation of a magnon-BEC involves the thermalization of the primarily pumped spin-wave mode with all neighbouring spin-wave states. This happens due to four magnon scattering. Only if the intrinsic thermalization time is smaller than the extrinsic thermalization with the lattice, the bottom of the spectrum will be reached. Since the system has to be continuously pumped, the spin-wave distribution $n(k)$ is essentially in a quasi-equilibrium, described by a Bose-Einstein distribution with non-zero chemical potential μ :

$$n(\mathbf{k}) = \frac{1}{\exp \frac{\hbar\omega(k)-\mu}{k_B T} - 1} \approx \frac{k_B T}{\hbar\omega(k) - \mu}, \quad (2.35)$$

where the temperature T exceeds the lattice temperature T_0 , and characterizes the quasi-equilibrium. In an infinitely extended film ($\frac{t}{l} \approx 0$), the spin-wave modes are so dense in the phase-space that a practically continuous scattering path from the pumped mode down to the bottom of the dispersion at ω_{bottom} is possible. If the chemical potential $\mu = \hbar\omega_{bottom}$, condensation sets in. A magnon-BEC has a macroscopic occupation number of the lowest-frequency state. In a tangentially magnetized YIG-film, this state is degenerate ($k = \pm k_{bottom}$). Both components interfere, resulting in a standing wave pattern [98]. The spectral linewidth $\delta\omega/2\pi < 6$ MHz [36] is extremely small (theoretically it should vanish).

2.3.2 Spin current-induced instability

In this section I will briefly discuss the so-called spin-Hall effect (SHE), and in particular how it can be exploited to excite magnetization dynamics. Theoretical considerations related to semiconductors were first published by D'yakonov and Perel' [35] in 1971. In 1999 Hirsch [52] extended this ideas to paramagnetic metals. Experimental observations in semiconductors followed in 2004 by Kato et al. [62], in metals by Valenzuela and Tinkham [127] in 2006.

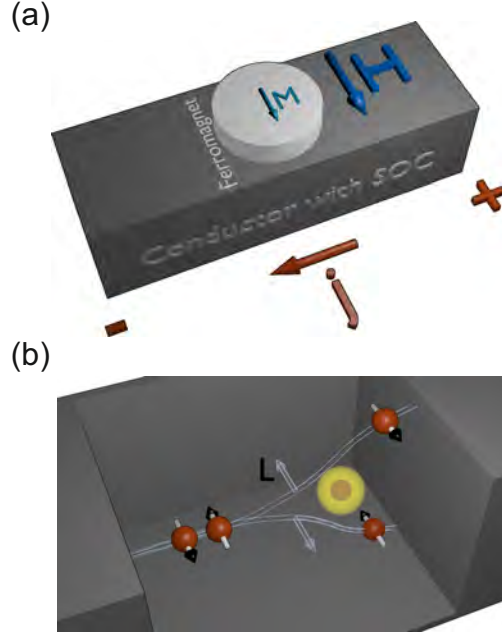


Figure 2.7: Working principle of magnetic oscillators driven by spin-currents generated by the spin-Hall effect. (a) Typical device geometry as used in reference [27]. (b) View inside the conductor. Note that the spin-magnetic moment $\mathbf{m}_s = -1/2g\mu_B\mathbf{s}$ is opposite to the spin indicated by the vectors inside the red spheres representing electrons. Scattering at the yellow location either deflects the electrons up- or downwards. The blue vectors indicates the orbital moment \mathbf{L} connected with this directions.

The essential idea behind SHE is that if a charge current \mathbf{j}_c , consisting of a priori unpolarized electrons, experiences scattering influenced by spin-orbital coupling, the deflection direction in this scattering process (connected in a simple picture with an orbital moment \mathbf{L}), depends on the spin-orientation \mathbf{s} (see Figure 2.7). The notion of spin-Hall effect actually encompasses a range of physical mechanisms, therefore it is more precise to speak them in plural. An introductory overview can be found in [53]. Spin skew scattering [116] at impurities is an example for an extrinsic contribution. Relativistic band structure calculations [46] show that also intrinsic contributions can give rise to a SHE. In analogy with the classical Hall effect, one can theoretically introduce a spin current $\mathbf{j}_s \perp \mathbf{j}_c$, which flows till a certain non-equilibrium spin-polarization at the boundaries of the conductor is established. In a more precise description, the spin current should be considered as a tensor, combining the vectorial spin current density with the vectorial spin moment. In this thesis experimental devices are considered, where only a particular spin-current flow direction (z -direction) is of interest. Thus we

will treat the spin current j_s as a scalar quantity. Using semi-classical Boltzmann-transport equation [135], the length scale of this induced magnetization can be connected with the spin-diffusion length λ_{sf} . In Pt used in the samples discussed in this thesis, $\lambda_{sf} = 1.25(2)$ nm [123].

If a ferromagnetic material is in touch with the conductor, the spin-polarization will diffuse into the ferromagnet. Spin-magnetic moment is adsorbed by the magnetic system, when one states that a spin-current flows into the ferromagnet. This spin current exerts a torque on the magnetization (spin-transfer torque, STT). The spatial scale of the action of the STT in the metallic ferromagnet can be related to spin diffusion and spin dephasing [85]. Especially the latter effect limits the length scale to a few atomic layers. In thick systems, where the dynamic modes have a vertically inhomogeneous profile, like in several μm thick YIG, this has to be taken into account, when trying to describe the influence of the STT on the dynamic magnetization [132]. In the thin film systems considered in this thesis, like a few nm thick Py, the mode profiles of experimentally accessible spin-wave modes are vertically homogeneous. Therefore the action of the STT practically extends throughout the whole thickness.

The dimensionless spin-Hall angle ϕ_H describes the conversion efficiency between spin- and charge current. The sign and magnitude of the spin-Hall angle characterize the spin-current generation in the non-magnetic conductor. For platinum ($\phi_H = 0.068(5)$ [77]) or gold ($\phi_H = 0.0035(3)$ [93]) it is a positive quantity, for tantalum ($\phi_H = -0.02(2)$ [49]) or tungsten ($\phi_H = 0.30(2)$ [101]) the spin-Hall angle is negative. Several methods exist to determine ϕ_H , yielding results which differ in case of Pt by one order of magnitude ($\phi_H = 0.0120(6)$ [40] versus $\phi_H = 0.11$ [2]). Up to now, no consensus is established, which method provides the more reliable value. The variance of the determined values also reflects a methodological problem: although often being referred to as the spin-Hall angle in a given material, the experimental measurement often utilizes a second magnetic material, which absorbs the spin current. Thus the spin-dependent reflection and transmission properties of the interface become decisive for the magnitude of the spin-Hall angle. Moreover, proximity induced magnetism in the conductor further complicates the situation [5, 55, 76].

The investigations discussed in this thesis focus on a practical aspect of the physics involved in SHE, which is the effect of a spin-current on the magnetization. Within this more phenomenological picture, the spin current exerts a torque on the magnetization. This torque can be described by a Slonczewski-term (see Eq. (15) in [114]). The conventional micromagnetic implementation, added to the usual Landau-Lifshitz-Gilbert (LLG) equation, describes a thin film of thickness

t , floated by a charge current j_c with a polarization \mathbf{p} of the spin-magnetic moment, and spin-polarization efficiency ϵ . The spin-transfer torque τ_{STT} is given by:

$$\tau_{STT} = -\frac{\beta}{M_0} \mathbf{M} \times \mathbf{M} \times \mathbf{p}, \quad (2.36)$$

where

$$\beta = j_c \frac{\epsilon g \mu_B}{2e M_0 t} \quad (2.37)$$

has the dimension of a frequency. It's physical meaning is the growth rate of STT induced magnetization oscillations. Although this term was developed to describe the effect of spin-polarized charge currents, the definition of β Eq.(2.37) explicitly only considers the spin-magnetic moment carried by the electrons. Therefore it is also a valid description when considering pure spin-currents generated by the SHE. Then the spin Hall angle ϕ_H has to be substituted for the spin polarization efficiency ϵ . The full equation of motion - the Landau-Lifshitz-Gilbert-Slonczewski (LLGS) equation is given by

$$\dot{\mathbf{M}} = \tau_H + \tau_G + \tau_{STT}, \quad (2.38)$$

where the torque τ_H of the effective field is

$$\tau_H = -\gamma \mathbf{M} \times \mathbf{H}_{eff}, \quad (2.39)$$

and

$$\tau_G = \frac{\alpha}{M_0} \mathbf{M} \times \dot{\mathbf{M}}. \quad (2.40)$$

For certain situations, the STT term can be written as an additional Gilbert-like damping term (see chapter 38 in [108]). Consider for instance a small angle precession of the magnetization $\mathbf{M} = [m_x, m_y, M_0]$, with $m_{x,y} \ll M_0$ in an infinity extended ferromagnet saturated by a magnetic field $\mathbf{H} \parallel \mathbf{e}_z$, subject to a spin current with polarization $\mathbf{p} \parallel \mathbf{H}$. The corresponding torques are shown schematically in Figure 2.36. The Gilbert damping torque is then approximately

$$\tau_G \approx -\alpha \omega_H (m_x \mathbf{e}_x + m_y \mathbf{e}_y), \quad (2.41)$$

which is collinear with the spin-transfer torque

$$\tau_{STT} \approx -\beta (m_x \mathbf{e}_x + m_y \mathbf{e}_y). \quad (2.42)$$

In principle one can define an effective damping constant $\alpha' = \alpha + \frac{\beta}{\omega_H}$ to retain

again the LLG equation. Note that in confined systems with eigenfrequencies ω_{mn} , the factor $\alpha\omega_H = \alpha\gamma H$ in Eq.(2.41) is replaced by $\omega_{r,mn} = \alpha\omega_{mn} \frac{\partial\omega_{mn}}{\partial\omega_H}$. The spin-transfer torque instead is not affected.

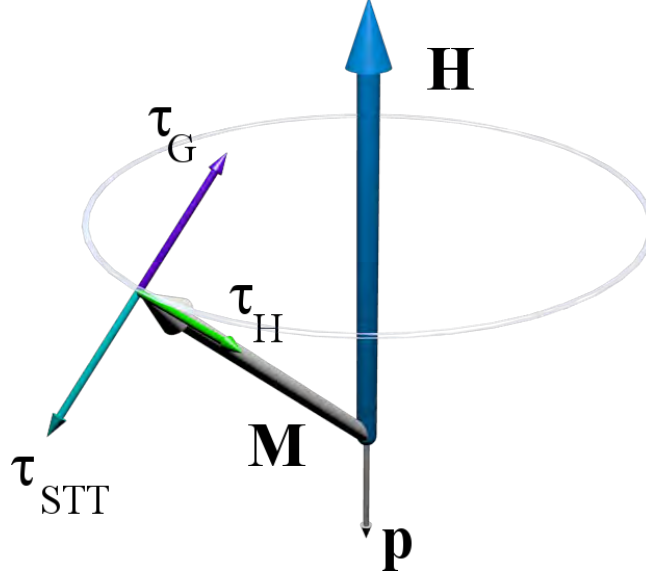


Figure 2.8: Effect of the spin torque τ_{STT} on the dynamic magnetization \mathbf{M} . For $\mathbf{p} \parallel -\mathbf{H}$, τ_{STT} opposes the Gilbert damping torque τ_G , which tends to realign \mathbf{M} with the external field \mathbf{H} .

Suppression of auto-oscillations in devices with non-local spin-current injection

Initial investigations [27, 26, 38] of magnetization dynamics induced by a pure spin-current focussed on a device geometry (see Figure 2.7), in which the ferromagnet as a whole is subject to the spin-current due to SHE. The main results of this investigations is that the spin-current induced dynamics is incoherent. No coherent auto-oscillation can be excited.

Consider now a confined magnetic structure, as described in chapter 2.2, and used in the aforementioned experiments. In the presence of thermal magnetic fluctuations, the STT amplifies or attenuates these oscillations. The non-equilibrium nature of the magnetic system is reflected by the average energy per mode, which is given by [27]

$$\langle E_i \rangle = k_B T \frac{\Gamma_i}{\Gamma_i - \beta}, \quad (2.43)$$

where $\Gamma_i = \omega_r = \alpha\omega_i \frac{\partial\omega_i}{\partial\omega_H}$. Generally, the losses Γ_i are mode-dependent. As a rule of thumb, larger frequency implies larger Γ_i . Therefore, for $\beta > 0$, modes with

low frequency, which are in the dipolar part of the spin-wave spectrum, will be stronger affected than the high-frequency exchange part.

For $\beta = 0$, the system is in thermal equilibrium. In accordance with the equipartition theorem (2.43) states that $\langle E_i \rangle = k_B T$ for all modes. Instead in the presence of STT $\beta \neq 0$, and (2.43) can be interpreted as a definition of a mode-dependent temperature $T_i = T \frac{\Gamma_i}{\Gamma_i - \beta}$. Depending on the sign of β , SHE can suppress or enhance thermal fluctuations. Furthermore, if $\beta = \Gamma_i$ Eq. (2.43) predicts that the energy $\langle E_i \rangle$ diverges. This should first happen for the mode with the lowest frequency and losses Γ_i , which then experiences a spin-current induced instability. In a confined system, the typical candidate is the FMR mode. But in fact, this divergence is not observed [27]. What goes wrong? When the mode's amplitudes strongly differ from thermal equilibrium, the notion of a constant Gilbert damping factor α fails [121]. Instead, α effectively increases. It was argued in [27] that in particular scattering of the FMR mode with short-wavelength exchange spin-wave modes increases. Therefore the losses Γ_0 of the FMR mode increase, and the instability is suppressed. In the supplement 5.1 a qualitative analysis of the experimental data [27] is discussed.

In summary, in a global spin-current injection geometry, the inherently weak spectral dependence of the STT is not sufficient to sustain coherent auto-oscillations, due to non-linear damping. To enable such an instability, a device structure is needed, where the STT selectively amplifies a particular mode only.

Enabling auto-oscillations in a device with local spin-current injection

Coherent auto-oscillations (spin-current induced spin-wave instabilities) were observed in devices, where the spin-current injection is locally restricted [106, 25, 84]. Such devices, called spin-torque nano-oscillators (STNO), usually operate with spin-polarized charge currents. With other words, the spin current \mathbf{j}_s is conveyed by a charge current $\mathbf{j}_c \parallel \mathbf{j}_s$. In a STNO, the electrical contact is restricted to a small area (e.g. $20 \text{ nm} \times 20 \text{ nm}$). Figure 2.9 shows a sketch of a STNO, as used in [25]. The polarization of the current occurs in the small elliptical CoFe element (the polarizer) on top of the extended Py film (the free layer). Due to the shape anisotropy, the magnetization in the polarizer is not parallel to the applied field, in contrast to the magnetization in the free layer.

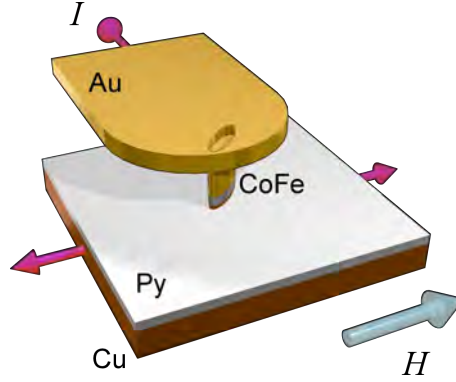


Figure 2.9: Typical device geometry of a magnetic oscillator [25] driven by a spin-polarized charge current.

Underneath the contact, a spin-torque is exerted on the magnetization in the free layer. Note that although the physical origin of the STT is different compared to the spin-Hall devices, the effect on the magnetization is the same. In chapter 4.3, I will show how a point contact for a pure spin-current can be realized. Considering thermal magnetic fluctuations described by Eq. (2.43), the losses $\Gamma_i = \omega_r + R$ now include a contribution from radiation R . This in particular affects the exchange spin-wave modes, which generally suffer from larger radiative losses. Their amplitudes therefore remain small inside the active area, which prevents scattering into these modes, and enables the instability process.

Slonczewski predicted [115] that for an out-of-plane magnetized film, a circular, isotropic spin-wave mode should become unstable. The wave length of this mode is connected with the diameter of the active area. In tangentially magnetized films, the dominant auto-oscillation mode is the so-called standing spin-wave bullet mode [111] - a solitonic solution of the LLGS equation. In theory, this magnetic soliton is closely related to optical solitons [110].

The following considerations can be found in more detail in [113]. To simplify the equations, spin-waves are there considered in the limit $t \rightarrow 0$. Then the factor $P_0 \approx 1$ in Eqs.(2.5) and (2.6), and the dipolar anisotropy drops out of the dispersion. The simplification of Eq.(2.4) only contains isotropic exchange:

$$\omega(\mathbf{k}) \approx \omega_0 + Dk^2, \quad (2.44)$$

where $D = \frac{\partial \omega}{\partial k^2}$ is the dispersion coefficient. To understand why a solitonic mode exists, it is instructive to write down the corresponding rate equation for it's

amplitude $c(t) \propto \exp(i\omega t)$:

$$\dot{c} = i(\omega_0 + N|c|^2 - D\nabla^2)c - (\Gamma_0 - \beta(1 - |c|^2))c, \quad (2.45)$$

where $N = \frac{\partial\omega}{\partial|c|^2}$ is the non-linearity coefficient. Without the dissipation and STT term, this equation is the non-linear Schrödinger equation. According to the Lighthill criterion [75], a solitonic solution exists for $ND < 0$. In a tangentially magnetized film this condition is satisfied because $N < 0$, and $D > 0$. The bullet is not part of the linear spin-wave spectrum, since its frequency $\omega_b < \omega_{bottom} \approx \omega_0$. For Eq.(2.44) this implies a purely imaginary wave number k . The immediate consequence is a stationary localization, reflected by the notion of a standing spin-wave bullet. Without the STT term, the bullet would not be stable [110]. Including this term, amplitude growth and spatial collapse due to the non-linearity, and dispersive spreading and amplitude decrease can be prohibited.

Before it was recognized that spin-wave bullets are important dynamic modes in spin-torque oscillators, propagating non-linear spin-wave packets also called bullets were studied in YIG films ([7], see [31] for a review). These packets also obey the non-linear Schrödinger equation, but lack in important property demanded by a soliton: two bullets do not survive a collision [15]. Moreover in YIG the envelope amplitude of such a propagating wave packet is typically restricted to a few percent of M_0 . In contrast in the Py-based spin-torque devices discussed in this thesis, the amplitude of the standing spin-wave bullet usually reaches 50 to 100 percent of M_0 . To understand the spatial properties of the standing spin-wave bullet mode, it can be decomposed in a Gedanken experiment into a static and a dynamic part. The static part describes a local reversion of the magnetization $\mathbf{M} \parallel -\mathbf{e}_x \parallel -\mathbf{H}$, on a scale of a few ten nanometres. This reversion is superimposed by a strong oscillation. When defined with respect to \mathbf{e}_x , the oscillation angle $\phi > \pi$. Such large angles were also found in simulations [18], where non-linear damping according to [121] was taken into account. Note that in BLS experiment, one measures the squared dynamic amplitude of the out-of-plane magnetization component m_z . As a counter-intuitive consequence of extreme oscillation angles, when $\phi = \pi$, any further increase of ϕ results in a decrease of the BLS intensity.

Chapter 3

Methods

3.1 Micro-focus Brillouin Light Scattering

The study of dynamic magnetic excitations allows to learn about the specific properties of the underlying magnetic system. When using magneto-optical methods, two approaches can be distinguished. One can either illuminate a sample stroboscopically in a pump-probe experiment, and obtains time-resolved information about the dynamic oscillation's phase. Note that only coherent oscillations, with a fixed initial phase can be investigated. The time-resolution is determined by the duration of the light pulses (fs to ps). To realize a time-shift Δt between the pump and probe event, optical delay stages are used. Practical limitations typically allow maximum $\Delta t \approx 1$ ns. Then the frequency resolution is $\Delta f \approx 1$ GHz. In conclusion, pump-probe experiment are best-suited to investigate coherent, ultra-fast transient dynamic processes.

The complementary spectroscopic technique is the so-called Brillouin Light Scattering (BLS) - the inelastic scattering of photons from magnons.⁷ Consider now a continuous, monochromatic light wave with frequency ω_i , and initial wave vector \mathbf{q}_i impinging on a magnetic specimen. In a classical picture one may interpret the presence of a magnon with wave vector \mathbf{k}_m , and frequency ω_m as a spatio-temporal modulation of the permittivity tensor ϵ . The off-diagonal components of ϵ which describe the interaction of the light with the magnetic system can be related to classical magneto-optic effects, such as Faraday rotation and ellipticity [130]. From a practical point-of-view it is important to realize that the scattered light has a different polarization than the impinging light: linearly polarized light will be rotated by 90° . A more exhaustive treatment can be found in [20].

Besides the above mentioned specific details, the scattering can be understood

⁷ Here only processes compromising one magnon and two photons are considered.

in a similar way as Raman scattering of photons from phonons: the magnon (phonon) constitutes a moving grating. The usual Bragg condition implies momentum conservation in the scattering event:

$$\mathbf{q}_{sc} = \mathbf{q}_i \pm \mathbf{k}_m. \quad (3.1)$$

Since the grating moves with phase velocity $v_{ph} = \omega/k$, the frequency of the scattered light will be Doppler-shifted. This is equivalent to the statement that in the particle picture, the magnon can either be annihilated or created. In this process the total energy is conserved. Therefore

$$\omega_{sc} = \omega_i \pm \omega_m. \quad (3.2)$$

The + sign in Equations (3.1), and (3.2) refers to magnon annihilation (Anti-Stokes process), the – sign to magnon creation (Stokes process). Compared to the stroboscopic time-domain approach, there is no demand for coherency of the magnetic dynamics in BLS. Instead the spectroscopic approach is characterized by a high frequency resolution, and low time resolution. Thus BLS is best-suited to investigate stationary, incoherent dynamics with many spectral contributions.

The experimental setup used in our laboratories is schematically shown in Figure 3.1. Before the light approaches the sample, a lambda-half wave-plate sets the polarization direction. The beam is subsequently expanded, and the profile is reduced to it's homogeneous central part by means of a diaphragm. In micro-focus BLS [29], the laser light is focussed into a diffraction limited spot on the surface of the magnetic sample. The scattering of the photons from magnons occurs upon reflection. To discriminate between light elastically scattered from the sample's surface, which maintains it's polarization, and light inelastically scattered from magnons, with rotated polarization, a polarizing beam splitter is used in order to send only the inelastically scattered light towards an interferometer.

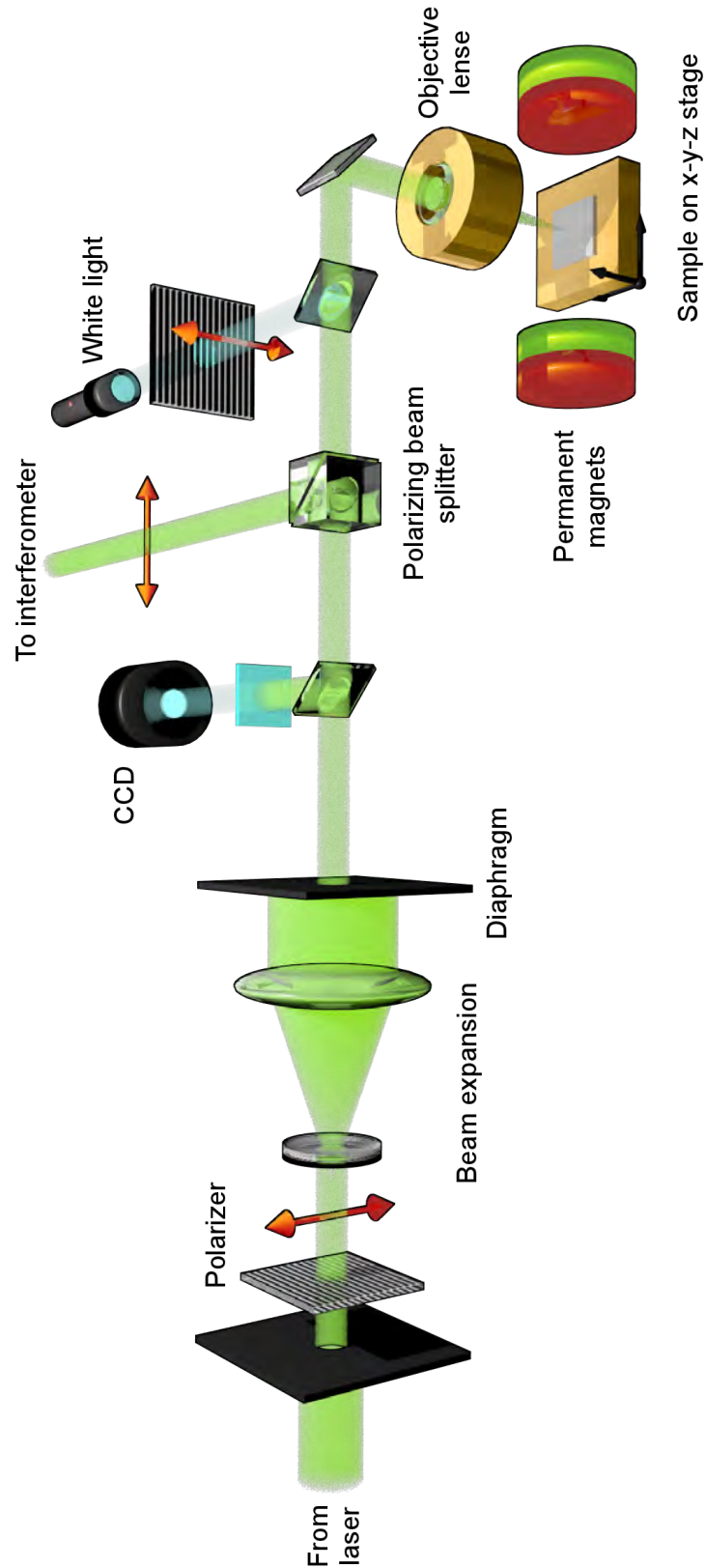


Figure 3.1: Schematic drawing of the micro-focus BLS setup.

The permanent magnets typically used in the setup create at the position of the sample fields H between 20 Oe and 2 kOe, controlled via the their distance. In addition a CCD camera and a white light source are integrated into the optical path. They allow to monitor the sample, to correct the focus, and to stabilize the lateral position. The polarizer behind the light source is a polarizing foil. Note that the sample is mounted on a piezoelectric x-y-z stage. 'Scanning the laser spot over the sample' therefore practically means to laterally move the sample with respect to the fixed focal position of the laser spot.

The laser probes the surface of the sample. In metals, the light can penetrate about 10 nm. The samples discussed in this thesis have a comparable thickness t . Therefore the question arises, whether a vertical variation of the dynamic magnetization has to be taken into account. When investigating for example surface waves with $\lambda < t$ (see [21]), this dependence cannot be ignored [14, 50]. In the following it will become clear that for thin Py investigated by micro BLS, vertically inhomogeneous profiles will not be encountered.

3.1.1 Focussing optics

The objective lens focusses the laser light onto a diffraction-limited spot. The electric field $E(x,y)$ can be described by (see Eq. (4.13) in chapter 4.1 in [99])

$$E(\mathbf{r}) = E_0 \frac{2J_1(x')}{x'}, \quad (3.3)$$

with $x' = \frac{2\pi NA}{\lambda} \sqrt{x^2 + y^2}$, and $J_1(x')$ being the first order Bessel function. In the experimental setup described here, typically a lens with numerical aperture $NA = 0.75$ is used, and green laser light with wave length $\lambda = 532$ nm. In Figure 3.2 the intensity $I(\mathbf{r}) = E^2(\mathbf{r})$ is shown along a radial section through the center, which can be approximated by a Gaussian function.

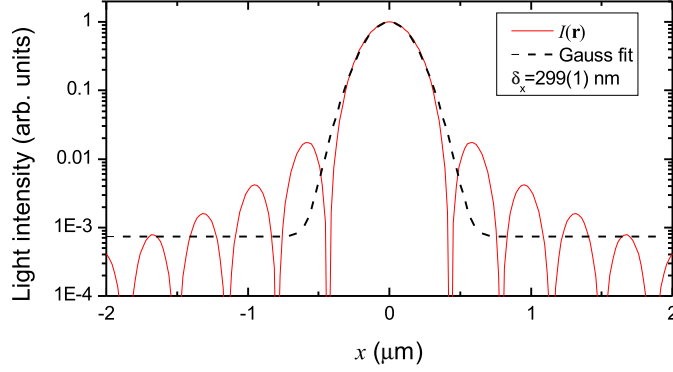


Figure 3.2: Light field of a diffraction limited laser spot in terms of intensity (red line), and Gauss fit (dashed line).

For later purposes it is instructive to take a look at the momentum representation $\hat{E}(\mathbf{q})$ of the light field, where q describes a transverse wave number. It is given by the circular function

$$\hat{E}(\mathbf{q}) = E_0 \text{circ}_{q_{max}}(q), \quad (3.4)$$

with $q_{max} = \frac{2\pi NA}{\lambda}$, and $\text{circ}_{q_{max}}(q) = 1$ for $q \leq q_{max}$, and $\text{circ}_{q_{max}}(q) = 0$ for $q > q_{tot}$. The q -space distribution of the scattered light $I_{sc}(\mathbf{q})$ is given by [56, 17, 45]:

$$I_{sc}(\mathbf{q}) = \left| \int d^2\mathbf{r} m(\mathbf{r}) E(\mathbf{r}) e^{i\mathbf{q}\mathbf{r}} \right|^2. \quad (3.5)$$

For strictly vertical incidence, $m = m_z$ refers to the out-of-plane component only. The integral in Eq.(3.5) is basically a Fourier transform

$$\mathcal{FFT} \{m(\mathbf{r}) \times E(\mathbf{r})\}(\mathbf{q}) = \hat{m}(\mathbf{q}) * \hat{E}(\mathbf{q}), \quad (3.6)$$

which can also be written as a convolution product. The wave number q refers to the in-plane momentum transferred into the light by means of the magnon creation or annihilation process. After this scattering, the objective lens collects all light with transverse wave numbers up to $q_{max} = \frac{2\pi NA}{\lambda} \approx 0.89 \times 10^5 \text{ cm}^{-1}$. The effective full scattering cross section σ is given by the integral:

$$\sigma = \int_{q \leq q_{max}} d^2\mathbf{q} I_{sc}(\mathbf{q}). \quad (3.7)$$

We have now all necessary formula, to estimate the wave number sensitivity in

micro BLS. Consider for instance an infinity extended film, which hosts a spin wave with some finite wave vector \mathbf{k}_0 . The lateral variation of the light field leads, via the convolution in Eq. (3.6), to a significant spreading of the scattered light into different momenta. This enables a sensitivity to spin waves with wave numbers up to $k_0 = 2q_{max}$. For larger k_0 , the convolution in Eq. (3.6) provides no contribution to the integral in Eq. (3.7). Note that although being sensitive for $k \leq k_0$, after being collected by the objective lens, the scattered light cannot be related to a particular wave number k anymore. Compared to standard BLS, in micro-BLS the k -space resolution is sacrificed in favour of having spatial resolution.

In the experiments discussed in this thesis, the thickness of the magnetic films $t \leq 10$ nm. In this situation, spin-wave modes with inhomogeneous vertical profile have $k \approx 10^7 \text{ cm}^{-1} \gg q_0$. Micro-BLS is not sensitive to such modes. This justifies a posteriori the disregard of any vertical variation of the scattered light.

3.1.2 Interferometer

The scattered light is sent to a Fabry-Pérot interferometer. The basic component of this instrument is a pair of mirrors with tunable distance d . Transmission occurs, when the distance is a multiple of the half wave length $\lambda/2$ of the investigated light. The transmission function is given by

$$\mathcal{T}(d, \lambda) = \frac{1}{1 + \frac{4\mathcal{F}^2}{\pi^2} \sin^2(2\pi dn/\lambda)}, \quad (3.8)$$

with n being the index of refraction of the medium between the mirrors, and \mathcal{F} being the finesse. Eq. (3.8) describes a band pass filter for light, whose band width $\delta\lambda$ is connected with the finesse $\mathcal{F} = \frac{\lambda}{\delta\lambda}$. The finesse is determined by the reflectivity and flatness of the mirrors. The transmitted light is sent onto a photo-multiplier.

The magnon signal is weak compared to elastically scattered light, and light inelastically scattered from phonons. To remove this background, an interferometer with high contrast

$$\mathcal{C} = \frac{I_{max}}{I_{min}} = 1 + \frac{4\mathcal{F}^2}{\pi^2} \quad (3.9)$$

is needed. Here I denotes the the intensity of the transmitted light. The interferometer design developed by Sandercock [107] in the 1970s and 1980s compromises two mirror pairs, whose optical axes are not collinear. One mirror of each pair is mounted on the same base plate, so that the transmission condition can be fulfilled simultaneously for both pairs. Furthermore, the light passes three times through

each mirror. For a mirror with given finesse, the contrast after six passes scales with $\mathcal{C}^6 \propto \mathcal{F}^{12}$. Then spin waves can be seen in the light scattering spectrum. Note that the output spectrum $S_{out}(\omega)$ of the interferometer is always a convolution of the input spectrum $S_{in}(\omega)$ with the instrumental function $\mathcal{I}(\omega) \approx A\mathcal{T}^6(\omega)$:

$$S_{out}(\omega) = S_{in} * \mathcal{I}(\omega). \quad (3.10)$$

The instrumental function can be directly seen in the shape of the spectral peak corresponding to the elastically scattered light. Also if a monochromatic forced oscillation is investigated ($S_{in}(\omega) = \delta(\omega - \omega_0)$), the full BLS spectrum $S_{out}(\omega) = I(\omega)$ depicts this instrumental function (shifted to ω_0). At a mirror distance of $d = 5$ mm, the FWHM of the instrumental function \mathcal{I} typically ranges between 200 MHz and 300 MHz, depending on the quality of optical alignment. The amplitude parameter A in the instrumental function \mathcal{I} models parameters related to processes without significant spectral dependence, like losses from optics inside the spectrometer, or the dead time of the final diode. Since absolute numbers are practically not demanded, and the physical meaning of A is usually not important, this parameter appears as a normalization constant only.

3.1.3 Micro BLS measurement of magnetization dynamics in confined structures

The lateral sizes (l_x, l_y) of the structures discussed in this thesis are comparable to the characteristic size of the laser spot. This basically introduces additional uncertainty for the wave number of the scattered light, apart from the uncertainty caused by the finite size of the laser spot. Mathematically the convolution in Eq.(3.5) can be factorized into a contribution from the laser light field, and a contribution of the shape of the structure.

The eigenmodes with quantization indices m and n can be regarded as standing waves (see chapter 2.2). That means, one has to insert a purely real mode profile $m_{mn}(\mathbf{r})$ into Eq. (3.5). For each eigenmode the effective scattering cross section follows from

$$\sigma_{mn} = \int_{q \leq q_{max}} d^2\mathbf{q} \, | \hat{m}_{mn}(\mathbf{q}) * \hat{E}(\mathbf{q}) |^2. \quad (3.11)$$

Note that Eq. (3.11) implicitly depends on the lateral position of the laser spot. Consider now as an example the mode $m = 1, n = 0$ in a rectangular structure with $l_x = l_y = 1 \mu\text{m}$. We assume that only this mode is excited. The

squared theoretical profile $m_{10}^2(\mathbf{r})$ is shown in Figure 3.3.

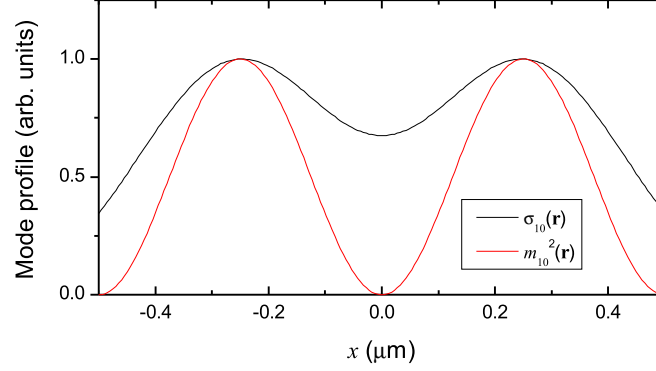


Figure 3.3: Emulated BLS measurement $I_{BLS}(\mathbf{r}) \propto \sigma_{10}(\mathbf{r})$ (black line) of a central section through the profile of the eigenmode with $m = 1$, $n = 0$ of a rectangular sample. The red line shows the squared theoretical profile $m_{10}^2(\mathbf{r})$.

By scanning the laser spot over the sample ($E(\mathbf{r}) \rightarrow E(\mathbf{r} - \mathbf{r}_0)$), the BLS intensity is proportional to the local, effective scattering cross section $\sigma_{10}(\mathbf{r}_0)$. Figure 3.3 shows a calculated section along \mathbf{e}_x through the center of this profile. The nodal line at $x = 0$, which can be seen in $m_{10}^2(\mathbf{r})$, manifest in $\sigma_{10}(\mathbf{r}_0)$ as a local minimum. The convolution of the input spectrum with the instrumental function $\mathcal{I}(\omega)$ is neglected so far. This convolution gains importance, if dynamics with spectral features below the FWHM of \mathcal{I} are investigated. An example for such an investigation (thermally activated magnetic fluctuations enhanced by STT) will be given in chapter 4.3.

3.2 Micromagnetic simulation

The central idea in contemporary numerical micromagnetics is to map the LLG(S) equation on a discrete lattice and perform a time integration. Similar to analytic micromagnetic theories, also here the quantum-mechanical origin of magnetism is not considered, but instead the magnetization as a microscopic consequence. Magnetic phenomena on time scales from ps to μm , and on spatial scales from nm to mm can be described. The upper limits have only practical reasons (computational time, memory available).

In the finite difference approach, the geometric volume of a given sample is discretized into a number of $N = N_x N_y N_z$ small cubic cells of equal size. The magnetization in each cell is assumed to be constant. The contribution of each energy term (exchange, anisotropy, Zeeman, and dipolar energy) to the local effective field has to be determined using discrete formulations. The computational effort differs, depending on the contribution. E.g., for the exchange field, the second derivative of the magnetization in a given cell with respect to its nearest neighbouring cells has to be evaluated. The numerical algorithm is of order $\mathcal{O}(N)$. The dipolar field is computationally most complicated, since this long range interaction couples all cells with each other ($\mathcal{O}(N^2)$). The numerical schemes can benefit from spatial Fourier transformation, reducing the algorithm's order in N to $\mathcal{O}(N \log N)$ [87]. Recent performance improvements were achieved by exploiting parallel computation with graphic cards [128, 80].

Micromagnetic simulation has become an important tool in the field of magnonics (see [64] for a review). Apart from assisting in interpretation of experimental data, this tool also allows to test conceptual ideas prior to their realization. For example, it was numerically shown by S. Gliga et al. [44] that in chains of sub-micrometer-sized stadium-shaped Py elements forming an artificial spin ice, edge mode frequencies depend on the relative orientation of the magnetization in adjacent elements. This allows to infer on the existence of artificial magnetic monopoles by analysing the spectrum of magnetic fluctuations.

In the context of this thesis micromagnetic simulations are conducted for three purposes: a) determination of eigenmode spectra of confined elements, b) investigations of dynamic spatial features smaller than the diffraction limit, and c) accessing profiles of the magnetization and internal field. Simulation is not used as a primary experimental method, but rather as an auxiliary tool for the interpretation of experimental data obtained by BLS.

3.2.1 Eigenmode spectra

Consider as an example a confined element made of a tangentially magnetized thin film. A typical simulation task is to determine the normal mode spectrum. For this, first-of-all the equilibrium magnetization configuration has to be found. As an initial guess, one can assume $\mathbf{M} \parallel \mathbf{H}$. Time integration after setting an artificially large damping constant leads to a fast approach of the static equilibrium. Once the system is settled, a realistic damping constant is assumed, and a short field pulse $\mathbf{h} \perp \mathbf{H}$ is applied. Thereby, many modes are excited simultaneously. The field pulse has to be small enough in magnitude, in order to avoid a non-linear response. For Py, a few Oe should not be exceeded.

The micromagnetic spectral imaging technique was introduced by McMichael and Stiles [88] in 2005. During the temporal integration following the field pulse, the vector field \mathbf{M} is saved at equidistant instants of time. Due to damping, the oscillations will decrease exponentially. Local spectral information can be obtained by performing a Fourier transformation of the time series $m_i(t)$ of each cell. For a tangentially magnetized system, it is most convenient to analyse the out-of-plane magnetization component m_z , because $\langle m_z \rangle_t = 0$, and therefore the spectrum automatically is free from contributions at $\omega = 0$. The result is a set of power maps $P(\omega, \mathbf{r})$, which resemble experimentally obtained maps of BLS intensity. Note that instead of the Fourier power, also the complex Fourier amplitude or Fourier phase can be inspected. A global spectrum $P(\omega)$ can be obtained by spatially integrating the power maps.

3.2.2 Characterizing excited systems

Power maps can as well be obtained by Fourier transforming stationary dynamics, sustained by a continuously applied dynamic field h or STT. Then, the influence of experimental parameters (strength of h , or of the current causing the STT) on spatial properties of dynamic modes can be studied. In such a situation it can be interesting to access the effective magnetic field \mathbf{H}_{eff} , and the magnetization \mathbf{M} itself. Time averaging these vector fields provides direct access to the static internal magnetic field $\mathbf{H}_{int} = \langle \mathbf{H}_{eff} \rangle_t$, and the effective magnetization $M_{eff} = \langle m_x \rangle_t$ (for $\mathbf{H} = H\mathbf{e}_x$). Experimentally, such information can only be inferred indirectly.

Chapter 4

Experiments

4.1 Non-linear scattering processes in confined elements

In this section spin-wave instabilities in micron-sized confined, ferromagnetic elements are investigated, experimentally and numerically. Qualitatively identical results were obtained for two elliptically shaped Py discs. These instabilities appear when driving the system into non-linear Ferromagnetic Resonance, by means of large dynamic fields h . Two processes are discussed, characterized by moderate and strong non-linearity. The experimental results are published in [23]. A theoretical interpretation can be found in [91]. In this work, the process at moderate excitation level is explicitly identified as second order Suhl instability. This interpretation will be adopted here. Also in [91], the overpopulation process at large excitation level is interpreted as kinetic instability. I will reason, how far this idea can hold. Following our publication [23], I finally suggest a different view of the overpopulation in terms of a magnon-BEC.

The numerical model, implemented with the software package MuMax2 [128], adapts the nominal geometry of the elliptical Py discs. Standard material parameters for Py were assumed (see table 1). If not explicitly mentioned, an external field of $H = 900$ Oe was applied along the long axis. As I will show, the simulations are able to reproduce the Suhl instability and the overpopulation. The motivation to perform the simulations is a) to characterize spatial properties, which are beyond the experimentally limited resolution, and b) to get direct access to the effective magnetization and internal field.

4.1.1 The sample

The investigated sample consists of a Au microstripline, which has a width of $w = 1\ \mu\text{m}$, and thickness of 160 nm. On top, elliptical ferromagnetic micro-discs were patterned from a 10 nm thick Py film ($1000\ \text{nm} \times 500\ \text{nm}$ and $500\ \text{nm} \times 250\ \text{nm}$). The long axis of the discs is oriented parallel to the edge of the stripline. Figure 4.1 shows a sketch of the sample. The Py structures are magnetized to saturation by means of an external magnetic $H = 400 - 900\ \text{Oe}$, applied tangentially along the long axis. When a microwave current, with frequency ω_{mw} , and power $P_{mw} = 0.01 - 100\ \text{mW}$, flows through the microstripline, a dynamic field $\mathbf{h} \perp \mathbf{H}$ is induced inside the microdiscs. A good impedance matching between microwave source, outer microwave transmission lines, and the inner antenna structure allows large h at relatively low P_{mw} , which enables the investigation of non-linear processes. To obtain BLS spectra, the incident light was positioned in the center of the elements. To avoid heating, the microwave current was pulsed with pulse length 100 ns and period $2\ \mu\text{s}$.

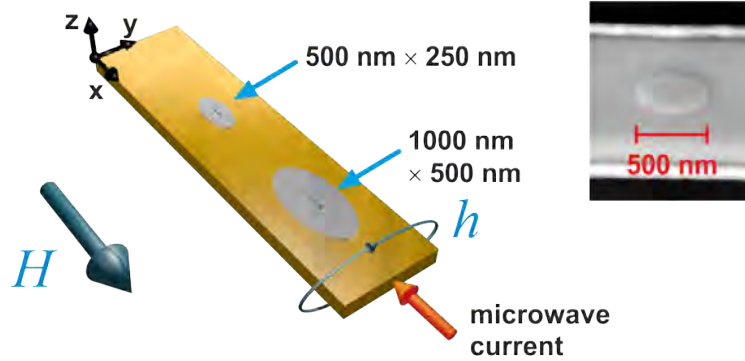


Figure 4.1: Sketch of the sample. On top of a Au microstripline, elliptical structures were patterned from a Py thin film ($t = 10\ \text{nm}$). The field H is applied along the long axis of the ellipses. The dynamic magnetic field h is perpendicular to the static field. The inset shows a SEM image.

4.1.2 Eigenmode spectrum

Before the experimental data is discussed, a micromagnetic determination of the eigenmode spectrum is presented. The procedure is adapted from [88]. The advantage in the numerical experiment is that higher order (antisymmetric) eigenmodes can be excited efficiently, so that a more complete picture will be established, than can be obtained experimentally.

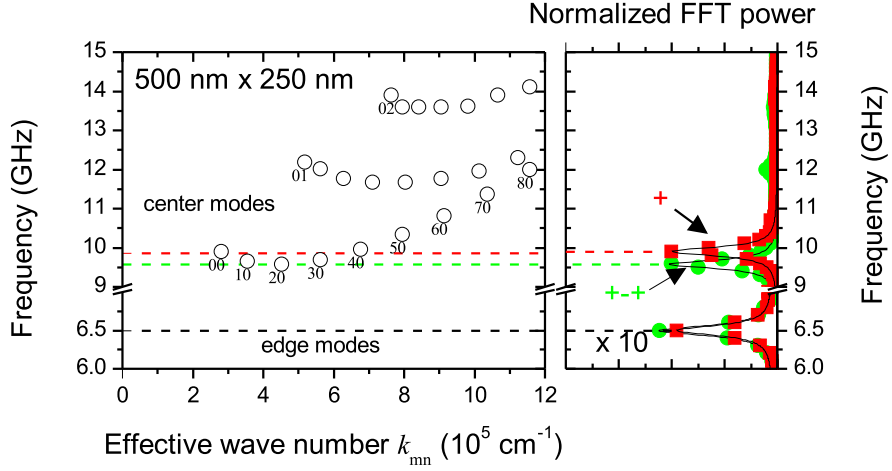


Figure 4.2: Left panel shows the eigenmode spectrum of the elliptical element with lateral size $500 \text{ nm} \times 250 \text{ nm}$. Right panel shows two representative power spectra, from which the eigenfrequencies $f_{mn} = \frac{\omega_{mn}}{2\pi}$ were extracted.

A short, spatially homogeneous field pulse $\mathbf{h} \perp \mathbf{H}$ was applied to a previously computed equilibrium state. The Fourier power of the dynamic response shows a maximum at a frequency of $\omega_{00}/2\pi = 9.9 \text{ GHz}$ (see curve denoted by symbol $+$ in right panel in Figure 4.2). In accordance with the uniform mode profile, we associate this maximum with the main resonance mode (the FMR analogue of the confined sample). The frequencies ω_{mn} of higher order modes were determined by applying field pulses which display the corresponding spatial symmetry ($+-$, $+ - +$ etc.). The lowest eigenfrequency $\omega_{20}/2\pi = 9.58 \text{ GHz}$ corresponds to a mode with spatial symmetry $+ - +$. Below the center modes, one finds a band of edge modes around 6.5 GHz . In between, no other eigenmodes exist. The field dependence of the FMR frequency and of the principal edge mode frequency is shown in Figure 4.9. Using standard parameters for Py slightly overestimates the experimentally obtained frequencies.

The spectrum for the sample with lateral size $1000 \text{ nm} \times 500 \text{ nm}$ is shown in Figure 4.3. Here, the FMR mode has a frequency of $\omega_{00}/2\pi = 9.4 \text{ GHz}$, and the lowest center mode has a frequency $\omega_{40}/2\pi = 9 \text{ GHz}$. The edge modes exist around 5 GHz .

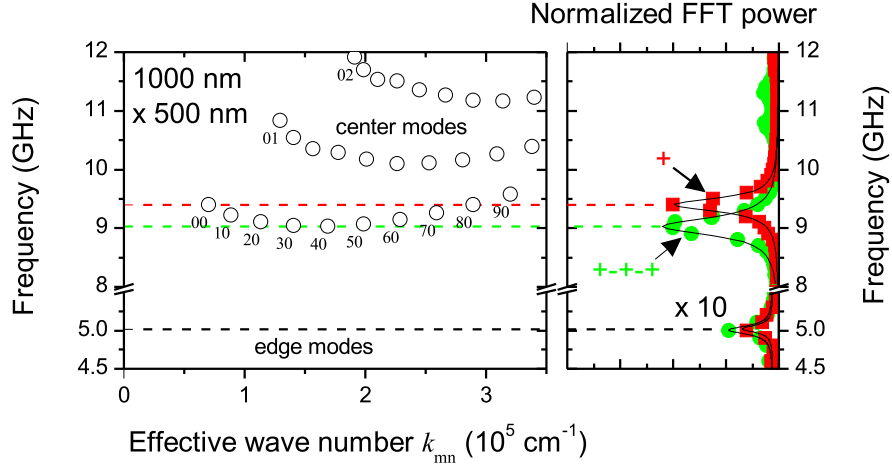


Figure 4.3: Left panel shows the eigenmode spectrum of the elliptical element with lateral size $1000 \text{ nm} \times 500 \text{ nm}$. Right panel shows two representative power spectra, from which the eigenfrequencies $f_{mn} = \frac{\omega_{mn}}{2\pi}$ were extracted.

4.1.3 Suhl instability

Experimental results

The spectral data discussed in the following refers to the structure with in-plane dimensions of $500 \text{ nm} \times 250 \text{ nm}$. At small microwave powers P_{mw} , the frequency-swept resonance curves are well described by a Lorentzian function, as shown in Figure 4.4(a) for $P_{mw} = 0.01 \text{ mW}$. The single peak at frequency $f_0 = 9.7 \text{ GHz}$ is connected with the sample's FMR mode. From the linewidth $\delta\omega/2\pi = 230 \text{ MHz}$ (measured in terms of the full-width half-maximum), a Gilbert damping factor of $\alpha = \frac{\delta\omega}{2\gamma(H+2\pi M_0)} = 0.008$ can be estimated, assuming standard material parameters. When increasing the microwave power (see resonance curve for $P_{mw} = 1 \text{ mW}$ in 4.4(a)), the linewidth $\delta\omega$ increases, the resonance curves become strongly asymmetric, and the resonance frequency shifts to lower values. These transformations are connected with non-linear damping and negative non-linear frequency shift.

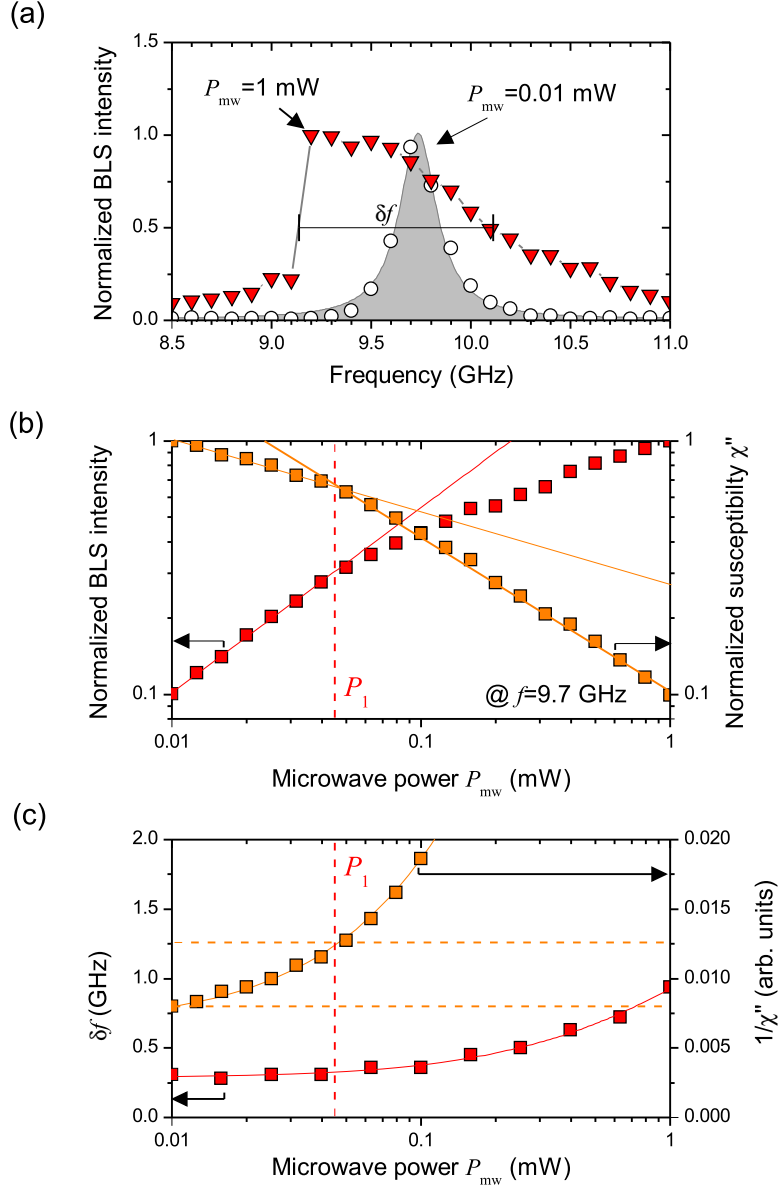


Figure 4.4: Non-linear FMR experiment of the smaller ellipse ($500 \text{ nm} \times 250 \text{ nm}$), measured by BLS. (a) Frequency-swept resonance curves at $H = 900 \text{ Oe}$ in terms of BLS intensity for two different microwave powers P_{mw} as indicated. (b) Dependence of BLS intensity I_{BLS} and susceptibility χ'' on P_{mw} at $\omega_{mw}/2\pi = 9.7 \text{ GHz}$. At $P_{mw} = P_1$, the experimental data curves show a kink (dashed horizontal lines marking the intersection of solid lines), which is connected with the onset of the Suhl instability. (c) Dependence of linewidth δf and $1/\chi''$ at $\omega_{mw}/2\pi = 9.7 \text{ GHz}$ on P_{mw} . Solid and dashed lines as guide to the eye.

The most obvious change (frequency shift and asymmetry) is caused by the non-linear frequency shift. As explained in chapter 2.3, the shift is connected with

a decrease of the effective magnetization with increasing precessional angle. The analytic equation (2.12) can be used to relate the frequency shift to the corresponding effective magnetization M_{eff} and precessional angle $\phi = \cos^{-1}(M_{eff}/M_0)$.⁸ At $P_{mw} = 0.1$ mW, the resonance frequency has dropped by 0.1 GHz, which is equivalent to $\phi = 12^\circ$. At $P_{mw} = 1$ mW, an angle of $\phi = 24^\circ$ follows from the even larger frequency shift of 0.5 GHz. Note that the frequency shift contributes to the increase of the linewidth shown in 4.4(c), as soon as the resonance curves become asymmetric.

A second contribution to the increase in linewidth is non-linear damping. In the linear regime, the peak intensity grows monotonously with the microwave power P_{mw} . At a particular power $P_1 = 0.04$ mW, the power dependence of the peak BLS intensity $I_0(9.7 \text{ GHz})$ displays a kink (see Figure 4.4(b)). At larger powers, the intensity still increases, albeit with a smaller rate. Simultaneously the linewidth increases (see 4.4(c)). These two behaviours can be consistently explained by a non-linear power dependence of the damping constant α , which enters the susceptibility $\chi'' \propto \alpha^{-1} \propto I_0/P_{mw}$. As outlined in chapter 2.3, Suhl explained this effect [118] by assuming the instability of a pair of degenerate spin waves, driven by non-linear terms in the LLG equation. In a confined element, one has to consider higher-order resonance modes, which are only approximately degenerate in frequency with the FMR mode.⁹

The threshold character of the instability process implies that at powers $P_{mw} < P_1$, the susceptibility χ'' should be constant. As Figure 4.4(b) shows, this is not true here. In metallic ferromagnets like Py it is well known that extrinsic losses (due to magnons scattering with electrons or phonons) dominate over intrinsic scattering processes (see chapter 14.2.5 in [47], and references therein). These extrinsic losses include two-magnon-two-electron scattering. In reference [119] Suhl pointed out that any kind of two-magnon scattering giving rise to a non-linear contribution to the damping at microwave powers $P_{mw} < P_1$, results in a non-constant susceptibility. In such a scenario the linewidth is not a good measure for the damping constant. Only initially one can assume $\delta\omega \propto \alpha$. At better

⁸ Without further modifications, the model described in chapter 2.2 overestimates $\omega_{00}/2\pi$ by about 1 GHz. Micromagnetic simulation shows that dynamic dipolar pinning expands l_y to an effective value of $l_y = 326$ nm, which has to enter Eq.(2.12) instead of the nominal value of 250 nm. Setting $M_{eff} = M_0$ at the lowest microwave power $P_{mw} = 0.01$ mW, and solving $\omega_{00}(H_{int})/2\pi = 9.7$ GHz (for $m = n = 0$) for the internal field, yields an effective value of $H_{int} = 788$ Oe, which is smaller than the value in the center of 870 Oe.

⁹ A more detailed discussion of the underlying process follows in subsection 4.1.3. Spatial signatures are beyond the experimental capabilities, especially for the structure with lateral sizes of $500 \text{ nm} \times 250 \text{ nm}$ discussed here.

measure is provided by the inverse susceptibility: at resonance Eq.(2.16) implies $\chi''^{-1} \propto \alpha$. For $P_{mw} < P_1$, the linewidth is constant, whereas χ''^{-1} significantly increases (see 4.4(c)).

Numerical results

Here, a numerical counterpart of the FMR experiment, conducted for both ellipses, will be discussed. We start with an investigation of the non-linear transformation of the resonance curve. For this a continuous excitation of the structures at frequency $\omega_{mw} = \omega_{00}$ was initiated, beginning with the equilibrium state at a given static field H . After several nanoseconds a dynamical equilibrium is reached. For small enough dynamic field h , only one oscillation mode is present. Plotting the space and time-averaged squared dynamic amplitude $a_0^2 = \langle m_z^2 \rangle_{s,t}$ as a function of H yields the resonance curves shown in Figure 4.5(a). At small $h = 1$ Oe, the resonance curve can be well approximated by a Lorentzian function.

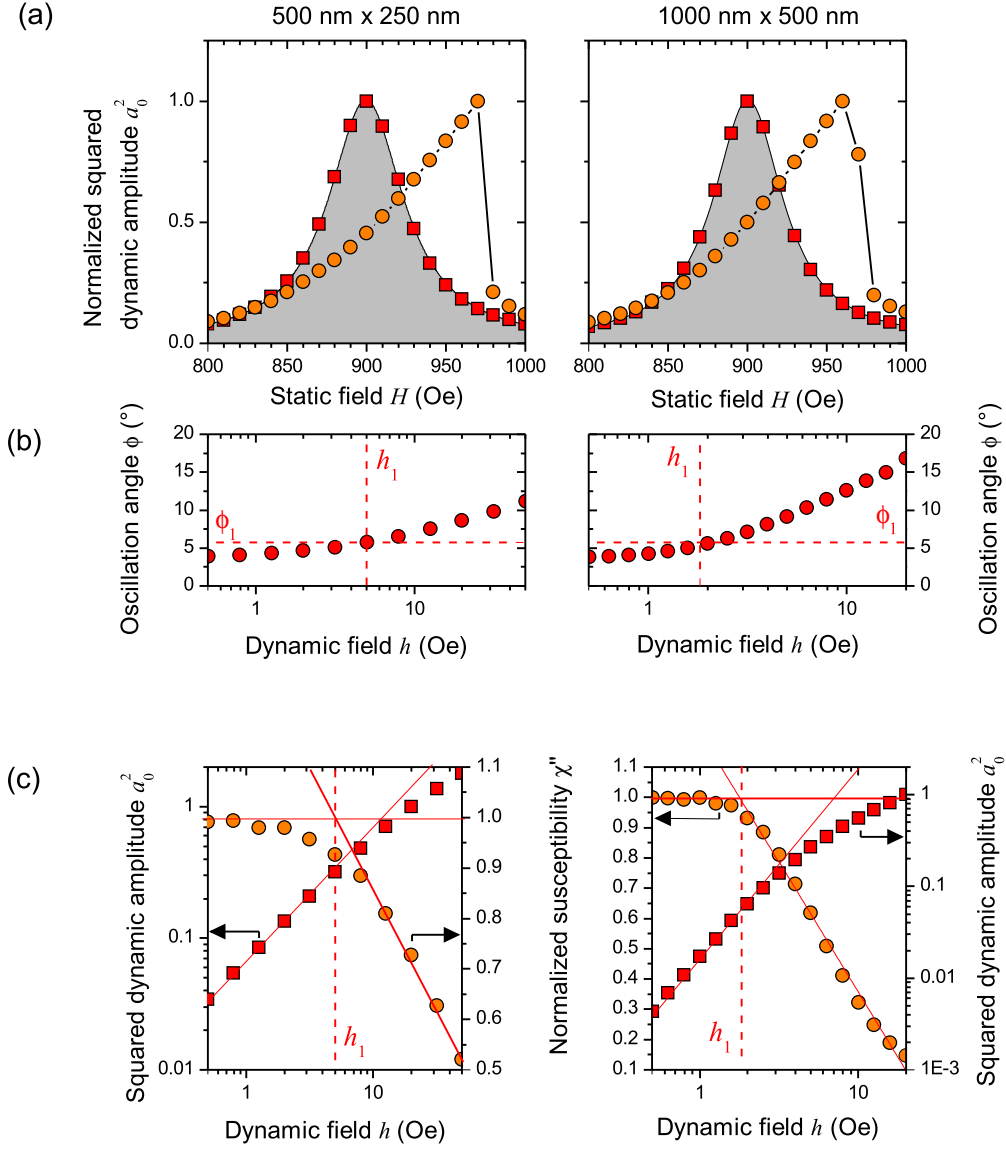


Figure 4.5: Numerical non-linear FMR experiment. Left panels show data for the smaller ellipse ($500 \text{ nm} \times 250 \text{ nm}$, $\omega_m w/2\pi = 9.9 \text{ GHz}$), right panels for the larger ellipse ($1000 \text{ nm} \times 500 \text{ nm}$, $\omega_m w/2\pi = 9.4 \text{ GHz}$). (a) Field-swept resonance curves $a_0^2(H)$ for two differently strong dynamic fields ($h = 1 \text{ Oe}$ and $h = 20 \text{ Oe}$). At $h = 1 \text{ Oe}$ the data can be described by a Lorentzian curve (grey shaded area). At $h = 20 \text{ Oe}$ the resonance curve is strongly asymmetric. (b) Oscillation angle ϕ as a function of the dynamic field h for fixed static field $H = 900 \text{ Oe}$. Dashed lines mark the threshold field h_1 and threshold angle ϕ_1 for the Suhl instability. (c) Dependence of a_0^2 and the susceptibility $\chi'' \propto a_0^2/h^2$ on the dynamic field h at fixed field $H = 900 \text{ Oe}$. Dashed line indicates the threshold field h_1 at which the Suhl instability appears. Solid lines as guides to the eyes.

One sees that as the dynamic field h is increased from 1 Oe to 20 Oe, the resonance field H_{res} increases, and the curve $a_0^2(H)$ becomes asymmetric. Recall that a similar effect was observed in the BLS experiment. The underlying processes was identified as negative non-linear frequency shift. In the numerical experiment, this process manifests as a positive non-linear resonance field shift. The process of non-linear frequency shift has no threshold: it sets in at arbitrarily low oscillation amplitudes.¹⁰ Time- and space-averaging m_x over several oscillation periods directly measures the effective magnetization $M_{eff} = \langle m_x \rangle_{s,t}$. Similar to the analysis of the real experiments we derive from this quantity the precession angle $\phi = \arccos(M_{eff}/M_0)$. Figure 4.5(b) shows ϕ as a function of the dynamic field h at $H = 900$ Oe. The angle grows continuously over the depicted range of the dynamic field. This underlines that the non-linear frequency shift is not an instability process. In the dependence of the squared dynamic amplitude a_0^2 at $\omega = \omega_{mw}$ on h shown in Figure 4.5(c) a characteristic kink appears at $h_1 = 3.4$ Oe for the smaller ellipse ($h_1 = 1.98$ Oe for the larger ellipse), corresponding to the experimentally found power threshold P_1 . As discussed, non-linear damping caused by the second order Suhl instability is likely responsible for this behaviour. The susceptibility $\chi'' \propto \frac{a_0^2}{h^2}$ remains constant up to h_1 , in contrast to the experimental data. Note that the oscillation angle $\phi_1 \approx 6^\circ$ at $h = h_1$ is the same for both structures, although the threshold field is not.

¹⁰ Note that at the power level P_1 , the simulation not yet shows a shift of H_{res} . This shows that the deviations from $a_0^2 \propto h^2$ as seen in Figure 4.5(c) is at this power level not connected with the non-linear frequency shift.

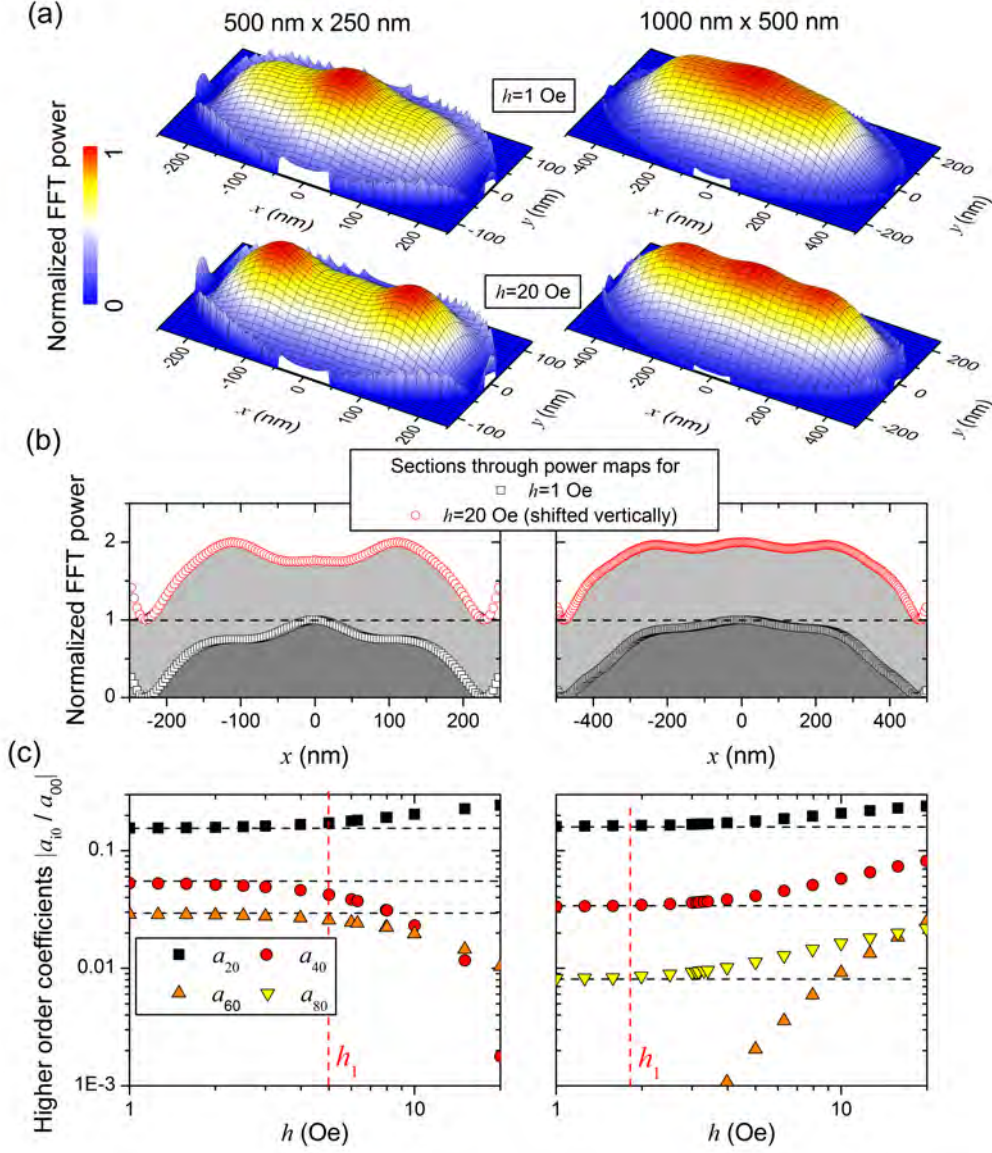


Figure 4.6: Simulated spatial transformation of the FMR mode due to the second order Suhl instability. (a) Normalized power maps $P(\omega_{00}, x, y)$ at $H = 900$ Oe for dynamic fields h below and above h_1 as indicated (linear color scale). (b) Central x -sections through power maps (open symbols, field h as indicated). Grey shaded areas result from fitting the test function p to the sections. (c) Dependence of higher order coefficients a_{i0} in test function p on h , normalized to a_{00} . Vertical dashed line marks the instability threshold field h_1 , the horizontal dashed lines highlight the relative constancy of the coefficients for $h < h_1$.

So far, the results reproduce the experimental findings. This provides confidence, to look at the spatial properties. Suhl instability means that at $h > h_1$, the

amplitude of the FMR mode is large enough to compensate the losses of degenerate modes. The dispersion diagrams 4.3 and 4.2 show that several higher order eigenmodes are approximately degenerate with the FMR mode. Figure 4.6(a) shows power maps $P(\omega_{00}, x, y)$ of the FMR mode in the two structures, calculated for dynamic fields below and above h_1 . A significant transformation of the profile can be seen, which complies with an increase of the dynamic amplitudes of higher order modes. The absence of phase jumps of π (such nodal lines manifest as lines with vanishing power in the power maps) inside the profile implies that the dominant contribution is still given by the FMR mode. Moreover, the complex Fourier amplitude maps (not shown here) contain no contributions from odd modes, neither for $h < h_1$ nor for $h > h_1$. Thus the symmetry of the FMR mode is preserved during the instability. A more quantitative understanding can be obtained by analysing central x -sections through the power profiles, as shown in 4.6(b). A coarse quantification of the transformation can be obtained by describing these sections via the squared function

$$p(x) \propto \sum_{i \text{ even}} a_{i0} \cos(i\pi/l_x) \quad (4.1)$$

The dependence of the coefficients a_{i0} on h is shown in Figure 4.6(c). These data clearly show that already at $h < h_1$ the profiles contain contributions from higher order modes. This is connected with the fact that the spatially homogeneous dynamic field h oscillating with frequency $\omega_{mw} = \omega_{00}$ can couple to all symmetric higher order modes if $\omega_{mw} \approx \omega_{mn}$, albeit with low efficiency. A similar effect was reported for macroscopic YIG discs [37]. Up to $h = h_1$, the coefficients do not change significantly. Referring to the smaller sample, the coefficient a_{20} then starts to increase. In the larger sample the situation is similar. For $h > h_1$ the coefficients of all approximately degenerate higher order modes start to increase. The dominant higher order contribution belongs again to the 20-mode.

4.1.4 Overpopulation

Experimental results

The results discussed in the following were obtained for the structure with lateral size of $500 \text{ nm} \times 250 \text{ nm}$. Qualitatively identical results were obtained for the larger structure. For $P_{mw} < P_2 = 4 \text{ mW}$ the system oscillation's are monochromatic: the BLS spectra show a single peak at ω_{mw} only (see Figure 4.7(a)). When approaching P_2 , the peak intensity saturates (see Figure 4.7(c)). This

indicates the onset of a qualitative change in the dynamics. At P_2 , the BLS spectrum suddenly shows additional peaks. The strongest secondary peak appears at a frequency $\omega_b/2\pi = 8.12 \text{ GHz} < \omega_{mw}/2\pi$. A third peak appears at $\omega_h/2\pi = 11.1 \text{ GHz} \approx (2\omega_{ex} - \omega_b)/2\pi$. When increasing the microwave power to $P_{mw} = 5 \text{ mW}$, the low frequency peak shifts to 8 GHz, the high frequency peak to 11.3 GHz. The intensity of both peaks increases, while the BLS intensity at ω_{mw} decreases by a factor of about 0.5. In addition, one can see small peaks around 6.2 GHz and 13 GHz. When further increasing P_{mw} , ω_b decreases noticeably, as shown in Figure 4.7(c), and indicated by the dashed line in Figure 4.7(a). The spectral peak around ω_b also broadens. The high frequency peak, and also the peaks around 6.2 GHz and 13 GHz totally disappear. The focus will now be on the low frequency peak at ω_b . The experimental data shown in Figure 4.7 witness a scattering process, which leads to an overpopulation of a particular spin-wave mode at this frequency. The expression overpopulation emphasizes that the occupation number of this mode strongly differs from thermal equilibrium.

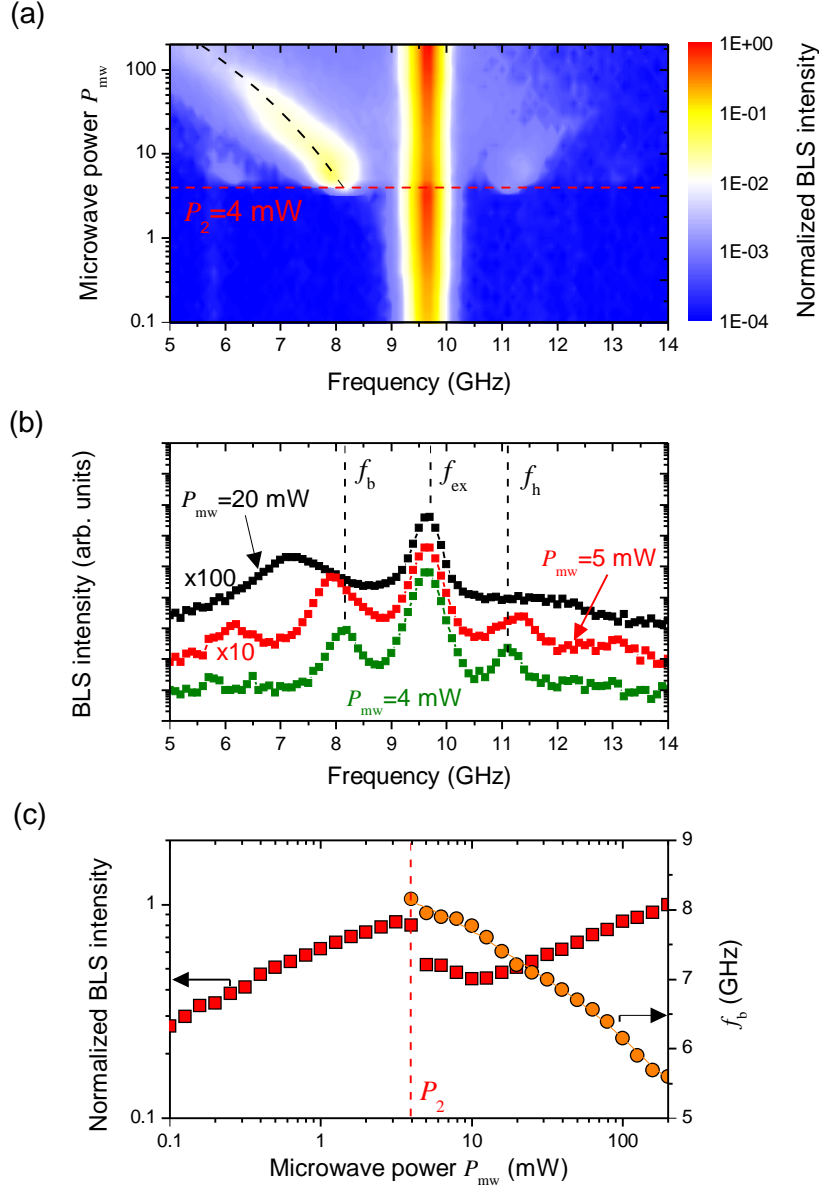


Figure 4.7: Overpopulation process in the smaller ellipse ($500 \text{ nm} \times 250 \text{ nm}$). (a) BLS intensity as a function of frequency and microwave power. Excitation at $\omega_{mw}/2\pi = 9.7 \text{ GHz} = \omega_{00}/2\pi$, $H = 900 \text{ Oe}$. Horizontal dashed line at $P_{mw} = P_2 = 4 \text{ mW}$ marks the onset of a scattering process. The frequency of the subsequently overpopulated mode decreases with increasing power, as indicated by the dashed curve. (b) BLS spectra for $P_{mw} = P_2$, $P_{mw} = 5 \text{ mW}$, and $P_{mw} = 20 \text{ mW}$. The spectra were multiplied by the factor indicated in the graph, to assure better visibility. (c) Power dependence of the BLS intensity at 9.7 GHz , and power dependence of the frequency f_b of the overpopulated mode.

Before providing an interpretation for the overpopulated mode, we address

it's spatial properties. Note that only the structure with lateral dimensions of $1000 \text{ nm} \times 500 \text{ nm}$ is large enough to allow spatial imaging of the overpopulated mode with diffraction-limited micro BLS. This structure has a FMR frequency of $\omega_{00}/2\pi = 9.3 \text{ GHz}$, and the overpopulation sets in at $P_2 = 1.6 \text{ mW}$. To obtain the dynamic profile of the overpopulated mode, the sample is excited with $\omega_{mw} = \omega_{00}$, and the laser spot is scanned over the surface, while the BLS intensity at ω_b is measured. This yields a two dimensional map, representing the mode profile in terms of the BLS intensity, which is proportional to the squared local amplitude. Figure 4.8(a) shows that at $P_{mw} = 3.2 \text{ mW}$, the overpopulated mode is localized in the center of the structure, decaying monotonously towards the edges of the ellipse. The x -section shown in Fig. 4.8(c) is well described by a Gaussian function, with a width of $\sigma_x = 380(10) \text{ nm}$ ($\sigma_y = 440(30) \text{ nm}$). When describing the laser spot's light field as a Gaussian function with $\sigma = 250 \text{ nm}$, deconvolution allows to estimate a lower boundary of the real size of $\sigma'_x = \sqrt{\sigma_x^2 - \sigma^2} = 290(20) \text{ nm}$ ($\sigma'_y = 360(40) \text{ nm}$). At larger power the mode expands, covering a larger fraction of the structure. The profile for $P_{mw} = 10 \text{ mW}$ is shown in Figure 4.8(b). At this power level, the mode profile follows the profile of the FMR mode, as indicated by the dashed line.

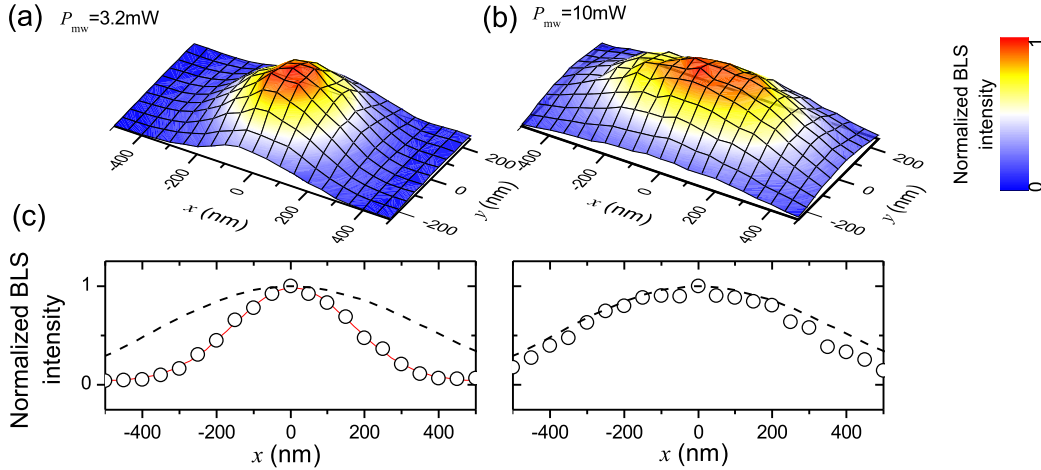


Figure 4.8: Spatial profiles of the overpopulated mode in terms of BLS intensity $I_{BLS}(\omega_b)$. In (a) for $P_{mw} = 3.2 \text{ mW}$, in (b) for $P_{mw} = 10 \text{ mW}$. In (c) central x -sections through the profiles in (a) (left panel) and (b) (right panel) are shown. The continuous red line shows a fit of a Gaussian function. The dashed line shows a x -section through the profile of the FMR mode.

We now assume that the spatial profile of the overpopulated mode in larger structure is qualitatively identical to the profile the smaller structure ($500 \text{ nm} \times$

250 nm). Its peculiar shape at $P_{mw} = 3.2$ mW cannot be related to any known center or edge mode. In particular the frequency $\omega_b < \omega_{00}$ suggests that the mode should be a (maybe higher order) edge mode, whereas the spatial imaging insinuates that the mode is a center mode. The interpretation published in [23] assumes that the overpopulated mode is reminiscent of the bottom spin-wave mode, which is locally excited in the center. Quite generally the large losses in Py enable modes, whose propagation length $\xi < l_y$ (see Eq. (2.9)) is smaller than the structures in-plane dimension. From the dispersion of thin films [60], it follows that the bottom spin-wave mode with frequency $\omega_{bottom} = \min\{\omega(k)\}$ has $\xi = 0$. Naively one may expect that if this mode gets overpopulated locally, the accumulating energy cannot be radiated. Therefore this kind of spectrally induced confinement (instead of geometrical confinement) immediately leads to large oscillation angles, which reduce the effective magnetization M_{eff} , resulting in a negative frequency shift. Within this model, setting $M_{eff} = M_0$ yields an upper frequency limit $\omega_{bottom}(M_0)$. The field dependence of this upper limit fits the experimental field dependence of the frequency ω_b of the overpopulated mode, as Figure 4.9 shows.

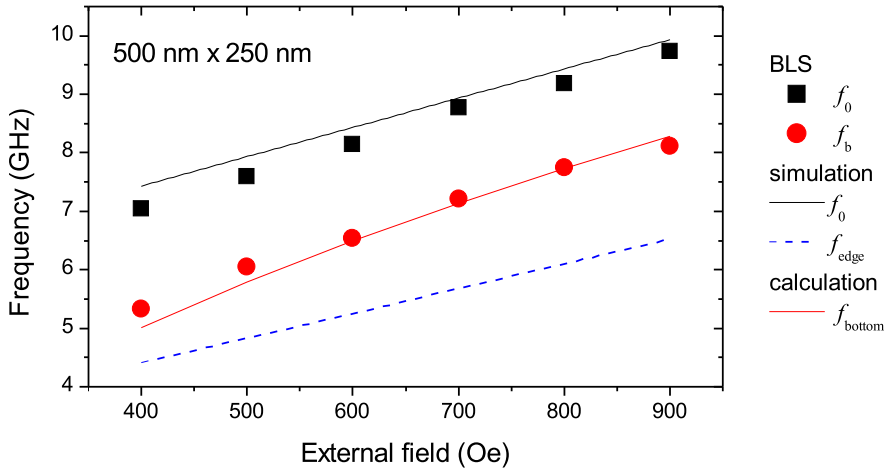


Figure 4.9: Field-frequency characteristics of the FMR mode (black dots) and the overpopulated mode (red circles). Black and blue dashed line show simulated field dependence of FMR and edge mode. The red line shows the calculated bottom spin-wave mode frequency.

Furthermore, it is possible to calculate the oscillation angle $\phi = \cos^{-1}(\frac{M_{eff}}{M_0})$

from the decrease of the frequency of the overpopulated mode by solving $\omega_b = \omega_{bottom}(M_{eff})$ for M_{eff} . For simplicity, the contribution of the FMR mode to the process of negative frequency shift is neglected. The obtained angles therefore give an upper bound only. At $P_{mw} = P_2$, an angle of 17° can be estimated. At larger power the mode expands, covering a larger fraction of the structure. Recall that simultaneously the frequency ω_b decreases. Both changes are self-consistent: as the frequency decreases, the regions with reduced internal field close to the boundaries can couple more efficiently to the dynamics in the center, promoting their expansion towards the outside. At $P_{mw} = 4P_2$ the frequency shift results in an oscillation angle of $\phi = 40^\circ$.

Numerical results

In this part only data obtained for the larger ellipse will be discussed. Simulations carried out for the smaller ellipse yield qualitatively identical results.

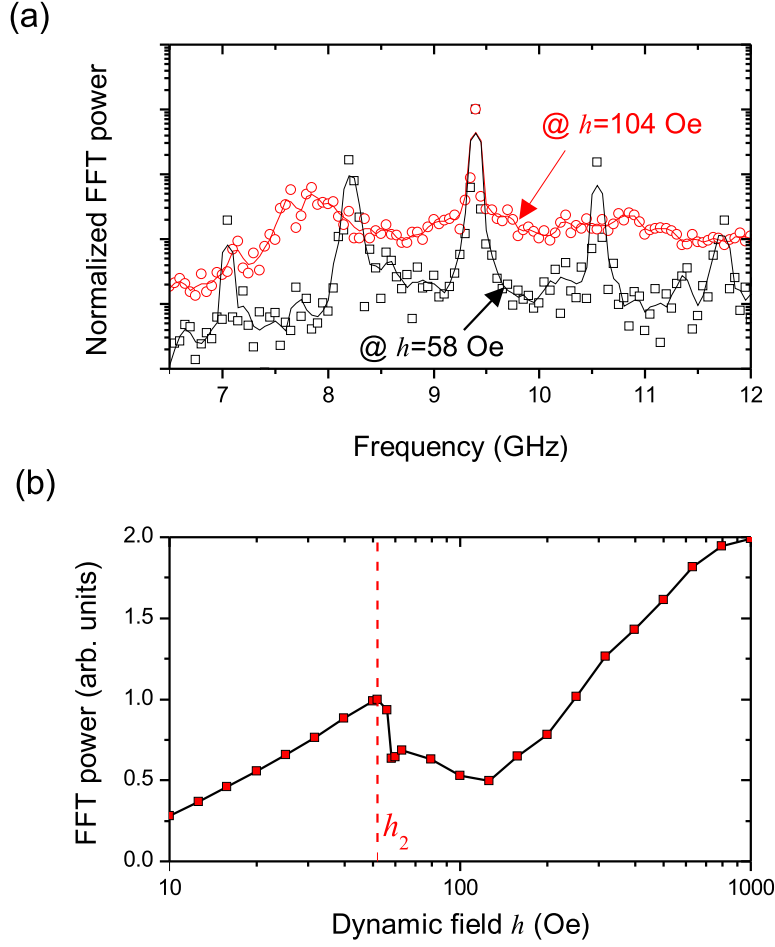


Figure 4.10: Simulation of the overpopulation process in the larger ellipse ($1000 \text{ nm} \times 500 \text{ nm}$). The field was set to $H = 900 \text{ Oe}$, the excitation frequency to $\omega_{mw}/2\pi = 9.4 \text{ GHz}$. (a) Fourier power spectra for two different dynamic fields $h > h_2$ as indicated. Thick lines are obtained from averaging the numerical data (open symbols). (b) Dependence of the Fourier power $P(\omega_{mw})$ on the dynamic field h .

Similar to the BLS experiment, up to a certain level $h = h_2 = 52 \text{ Oe}$ of the dynamic field, the system's oscillations are monochromatic. The power spectra show only a single peak at ω_{mw} . When exceeding this level, additional peaks appear in the spectrum, as shown by the power spectra in Figure 4.10(a). For $h = 58 \text{ Oe}$, the spectrum shows two strong secondary peaks at $\omega_b/2\pi = 8.1 \text{ GHz}$ and $\omega_h/2\pi = 10.55 \text{ GHz}$. In addition a set of smaller, equidistant peaks at $\omega_n = \omega_{mw} \pm (\omega_{mw} - \omega_b)$ can be seen. When further increasing the dynamic field to

$h = 104$ Oe, the lower peak shifts down to 7.85 GHz and broadens. The high frequency peak broadens even stronger, and diminishes relative to the peak at ω_b . The set of equidistant peaks vanishes totally.

If we look at the dependence of Fourier power $P(\omega_{mw})$ on h shown in 4.10(b), a characteristic drop when exceeding h_1 can be seen. The numerical data resemble the experimental data quite well (compare Figure 4.10(b) with Figure 4.7(c)).

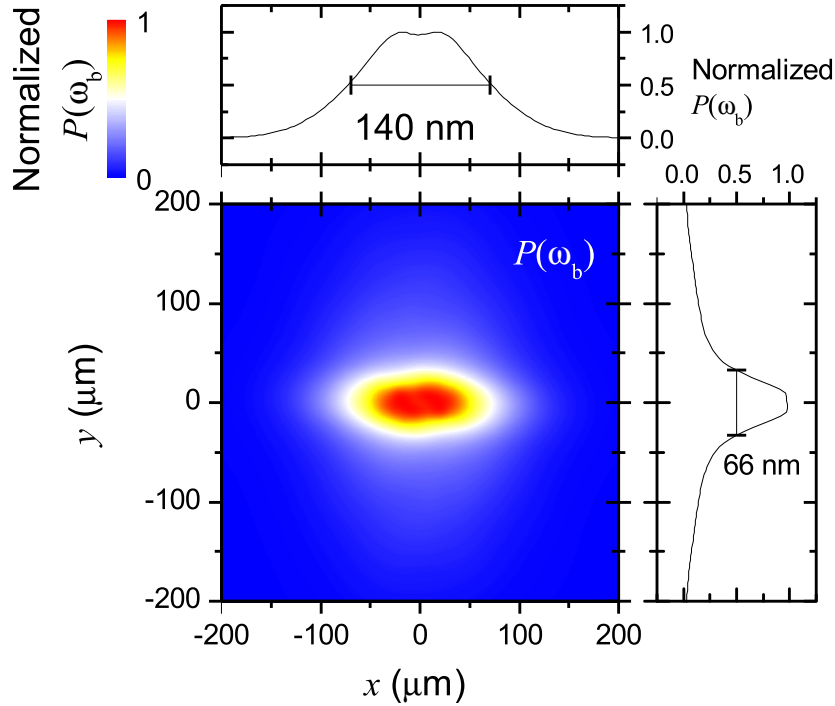


Figure 4.11: Spatial profile $P(\omega_b)$ of overpopulated mode in the numerical experiment. The plot refers to the larger ellipse ($1000 \text{ nm} \times 500 \text{ nm}$), to a dynamic field of $h = 58$ Oe, an excitation frequency of $\omega_{mw}/2\pi = 9.4$ GHz, and a static field of $H = 900$ Oe. The outer panels show central sections through the profile.

The qualitative effect of overpopulation is the same in the simulation and in the experiment. Therefore, as a next step, we will proceed with the analysis of the spatial properties of the overpopulated mode. Figure 4.11 shows the power map $P(\omega_b)$ of the overpopulated mode at $h = 58$ Oe. The mode is localized on spatial scales¹¹ of $\sigma_x = 140 \text{ nm}$ and $\sigma_y = 66 \text{ nm}$. The mode profile resembles the experimental findings (see 4.8(a)), although the overpopulated mode appears in

¹¹ σ_x and σ_y refer to the FWHM measured along x and y -section through the power maps $P(\omega_b)$.

the real experiment to be localized on a slightly larger scales.

The knowledge of the local Fourier power of the different modes allows to estimate¹² their individual contribution to the reduction of the magnetization $\Delta M = M_0 - M_{eff} = 0.48M_0 \propto P(\omega_b) + P(\omega_{00}) + P(\omega_h)$ in the center. From this, the local oscillation angle ϕ can be deduced. Accordingly, at $h = 58$ Oe the low frequency mode has an oscillation angle of 16° , the FMR mode oscillates with an angle of 9° , and the high frequency mode with an angle of 3° .

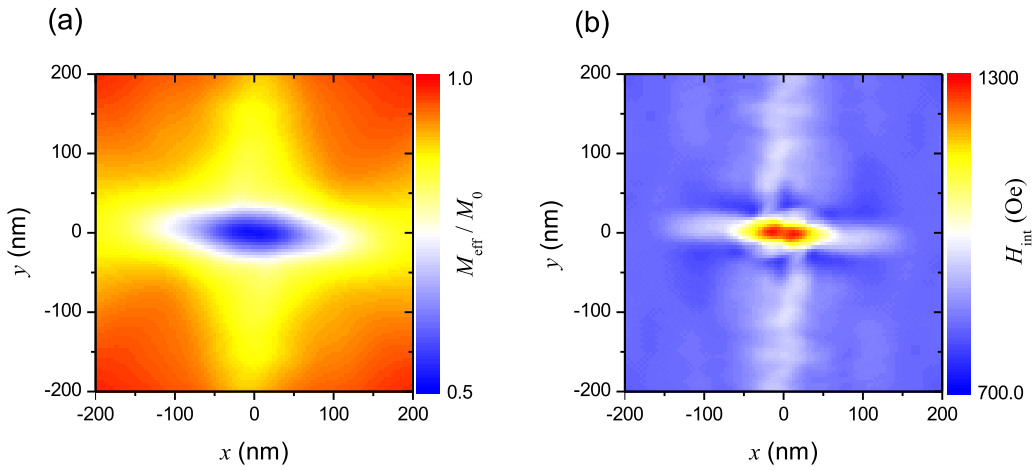


Figure 4.12: Simulated influence of strong dynamics due to overpopulation on the magnetization and on the internal field. The plots show a region of $400 \text{ nm} \times 400 \text{ nm}$ in the center of the elliptical disc with lateral size of $1000 \text{ nm} \times 500 \text{ nm}$. The plots refer to $h = 58$ Oe, $\omega_{mw}/2\pi = 9.4$ GHz, and $H = 900$ Oe. (a) Spatial profile of the effective magnetization M_{eff}/M_0 . (b) Spatial profile of the internal field H_{int} .

Further insight will be obtained by time-averaging the magnetization component m_x , yielding the spatial profile of the effective magnetization $M_{eff} = \langle m_x \rangle_t$. Figure 4.12(a) shows this profile for $h = 58$ Oe. The large amplitude of the dynamics result in significant reduction of the effective magnetization, down to $M_{eff} = 0.5M_0$ in the center. This strong reduction of M_{eff} also induces an alteration of the internal field. In Figure 4.12(b) the internal field, computed by time-averaging the x -component of the effective field $H_{int} = \langle H_{eff,x} \rangle_t$ is shown. The location of minimum M_{eff} is accompanied by a maximum $H_{int} \approx 1250$ Oe.

¹² In the calculation the same ellipticity for all contributing modes is assumed. Only the three strongest modes are taken into account.

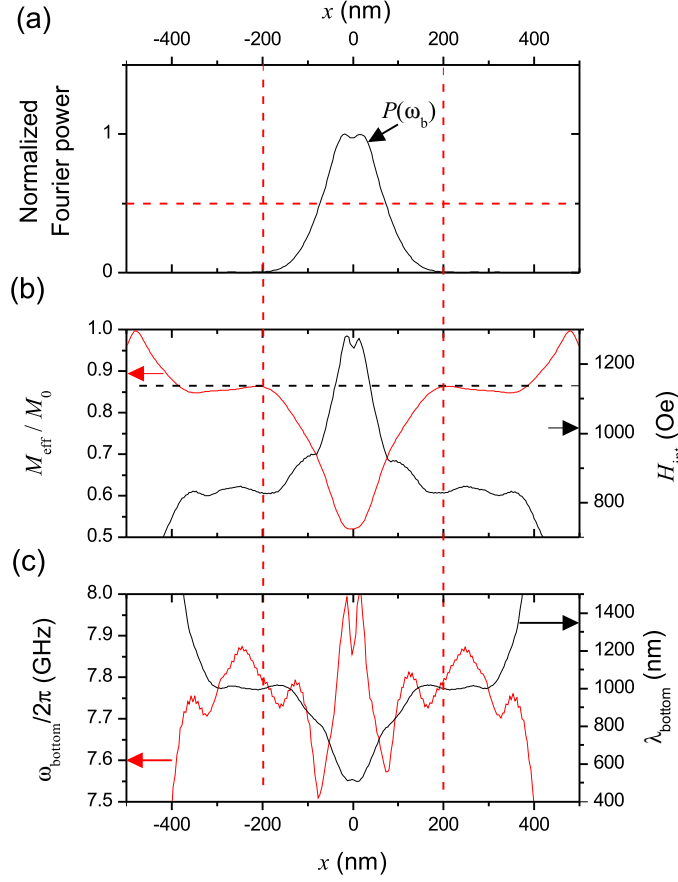


Figure 4.13: (a) Sections through mode profiles in terms of Fourier power. (b) Spatial dependence of the effective magnetization and the internal field. (c) Local bottom mode frequency and corresponding local bottom mode wave length λ_{bottom} . All data refer to $h = 58$ Oe, and $H = 900$ Oe. Vertical dashed line marks the lateral extend of the overpopulated mode, horizontal dashed lines as guide to the eye.

Now we will try to relate M_{eff} and H_{int} to the profile of the overpopulated mode. In Figure 4.13(b) both quantities are shown along a central x -section. The section through the power map plotted in Figure 4.13(a) show that the overpopulated mode is localized within the minimum of M_{eff} . If we assume local validity of the thin-film dispersion [60], we can compute the local bottom mode frequency $\omega_{\text{bottom}} = \min \{\omega(k, M_{\text{eff}}, H_{\text{int}})\}$, providing a lower frequency boundary for possible magnetization dynamics. At $h = 58$ Oe, the local internal field and effective magnetization yield $\omega_{\text{bottom}}/2\pi = 8.0$ GHz in the center, where the overpopulated mode has maximum amplitude. This boundary is close to the numerically observed value of $\omega_b/2\pi = 8.2$ GHz. The spatial dependence of the local bottom mode frequency is shown in Figure 4.13(c)). The corresponding bottom mode

wave length λ_{bottom} strongly depends on the location: in the center it drops to $\lambda_{bottom} = 510$ nm, whereas at $x = 200$ nm the wave length is about $\lambda_{bottom} = 1$ μ m. If we apply the quantization integral formalism introduced in chapter 2.2, i.e., we evaluate $\varphi = \int_{-200 \text{ nm}}^{200 \text{ nm}} \frac{2\pi}{\lambda_{bottom}(x)} dx$ inside the region where the overpopulated mode exists,¹³ the accumulated phase $\varphi = 1.06\pi$. In other words, the lateral expansion in the x -direction of the overpopulated mode guarantees a positive self-interference. In the y -direction a similar argument would demand an average wavelength in the order of $2\sigma_y$. Within the given spatial profile of M_{eff} and H_{int} , the corresponding DE-mode has a minimum frequency larger than 20 GHz. An alternative interpretation of the overpopulated mode, which circumvents these problems, will be given in the discussion.

4.1.5 Discussion

The BLS experiment and the numerical simulation draw a congruent picture of non-linear FMR in Py micro-structures. Both show: a) the second order Suhl instability at moderate microwave power P_{mw} or dynamic field h , and b) the overpopulation of a specific spin-wave mode at large P_{mw} or h .

The analysis of the experimental data reveals that already below the Suhl instability for $P_{mw} < P_1$, the susceptibility is not constant. This implies that a more accurate description of the relaxation processes demands a non-linear damping function α , as for example suggested in [121]. For low excitation powers $\alpha = \alpha_0 = 0.008$, which was assumed in the numerical experiment for all levels of agitation. Therefore, in the numerical experiment the susceptibility stays approximately constant up the onset of Suhl instability.

Second order Suhl instability

In accordance with the relatively large losses in Py, high dynamic amplitudes are necessary to enable this type of instability: the simulations show that the onset is connected with an oscillation angle of about 6° . Note that the Suhl instability process was also found experimentally [124] in a different structure, made of three coupled discs. The larger lateral size (in total $1 \mu\text{m} \times 3 \mu\text{m}$) allowed us to experimentally map the spatial transformation directly. In the experiments discussed here, these transformations appear on a scale close or below the diffraction limit. Therefore, meaningful spatial information can only be obtained from the numerical experiment.

¹³ The fact that the bottom mode frequency is actually not constant has been ignored here for simplicity.

The threshold field $h_1 = \mu_0 \frac{\sqrt{P_1/R}}{2(w+t)}$ can be estimated from the parameters of the stripline. The experimental power level $P_1 = 0.04 \text{ mW}$ refers to a dynamic field of $h_1 = 4.8 \text{ Oe}$, assuming an impedance of $R = 50 \Omega$. A rough theoretical estimate of h_1 by Eq. 2.33 yields the same order of magnitude. The numerically obtained threshold values of $h_1 = 1.98 \text{ Oe}$ for the smaller, and $h_1 = 3.4 \text{ Oe}$ for the larger sample are close to these values. Further evidence that the second order Suhl instability was observed at least in the numerical experiment, can be obtained by repeating the experiment for different α . From this the dependence of h_1 on α was obtained, yielding an exponent of 1.3(1), which is close to the theoretically expected exponent of 1.5. In literature [100], a threshold field of a few Oe is reported for extended Py films. Note that especially in this work, a quantitative determination of the damping constant α was possible, yielding a surprisingly small value. I will discuss a similar finding in the context of parametric excitation.

Overpopulation

In the experiment the overpopulation sets in at $P_2 = 4 \text{ mW} \Rightarrow h_2 = 48 \text{ Oe}$. In the simulation, the threshold for overpopulation was found at $h_2 = 52 \text{ Oe}$. This good qualitative agreement between experiment and simulation is somewhat surprising, given the fact that non-linear damping was totally neglected in the latter.

The originally published [23] interpretation of the overpopulated mode is to assume that this mode is reminiscent of the bottom spin-wave mode. This claim is supported by the field dependence of $\omega_b \approx \omega_{\text{bottom}}$. From the negative frequency shift of ω_b , relatively large oscillation angles $\phi \geq 17^\circ$ were deduced. The numerical experiment confirms the magnitude of overpopulated mode's oscillation angle. Furthermore, the additional information about the effective magnetization and the internal magnetic field allowed to refine the calculation of the local bottom spin-wave mode frequency. These calculations still approximately describe the frequency of the overpopulated mode. It was shown that the total lateral extend in the x -direction can then be interpreted as a signature of a positive self-interference.

Nevertheless, the localization in the y -direction cannot be explained by assuming a superposition of BWVM-like spin waves. Indeed, if one describes a point source oscillating at frequency $\omega \approx \omega_{\text{bottom}}$ by superposing modes on the iso-frequency curves around $\pm \mathbf{k}_{\text{bottom}}$, a caustic spin-wave structure results, which due to the dipolar anisotropy shows a high intensity beam directed along the y -direction [25, 126]. An alternative explanation of the overpopulated mode is to assume that it is a standing spin-wave bullet, as described in chapter 2.3.2. The

bullet can have frequencies below ω_{bottom} and is self-localized in both lateral directions, just like the overpopulated mode observed here. Note that in chapter 2.3.2, an approximate dispersion was introduced for pedagogic reasons, in which the dipolar anisotropy is neglected. When including the anisotropy, the dispersion can be expanded in a Taylor series up to second order in k_x and k_y . For BWVM modes, the expansion around $k_x = k_{bottom}$ yields $N < 0$, $D > 0$, and a diffraction coefficient $S = \frac{\partial \omega}{\partial k_y^2} > 0$. Since $ND < 0$, and $NS < 0$, the bullet as a solitonic solution exists. This consideration implies that in the x -direction the wave number $k_y = k'_y + \imath k''_y$ is for $\omega < \omega_{bottom}$ not strictly imaginary, but contains a real part which approaches $k'_y = k_{bottom}$ for $\omega = \omega_{bottom}$. The localization in the y -direction complies with a completely imaginary wave number for this direction. Note that in contrast to spin-torque oscillators, where the bullet is a stable solution because of the STT, the bullet is here sustained by means of a scattering process.

On a first sight it is appealing to interpret the scattering process causing the overpopulation as second order kinetic instability, as was done by the authors of [91]. Using simple rate equations it is possible to approximately reproduce for example the dependence of the peak BLS intensity $I_{BLS}(\omega_{00})$ on the excitation power shown in Figure 4.7(c). Kinetic instability demands the appearance of a high frequency secondary peak at $\omega_h \approx 2\omega_{00} - \omega_b$ in the spectrum. Experimentally such a peak can be seen, but only within a small range of microwave power. So far, these details do not contradict the interpretation that the overpopulation is caused by kinetic instability. But the numerical experiment reveals a deviation, which conflicts with this assignment. Equation (2.34) predicts a particular relation between the Gilbert damping constant α and the squared dynamic amplitude $a_0^2 \propto N_0$ of the FMR mode when reaching the threshold:

$$a_0^2 \propto \sqrt{\alpha} \quad (4.2)$$

Figure 4.14 shows that the scaling exponent $\beta = 0.185(3) < 0.5$. The vanishing of a_0^2 for $\alpha \rightarrow 0$ nevertheless clearly demonstrates that the overpopulation is an instability process connected with the compensation of external losses, albeit in a different manner than expected from second order kinetic instability. In summary, if one wants to maintain the interpretation that the overpopulation is a kinetic instability, one has to develop a theory, which takes into account the large amplitudes of the participating modes, and that, as a consequence, they are no linear eigenmodes of the system.

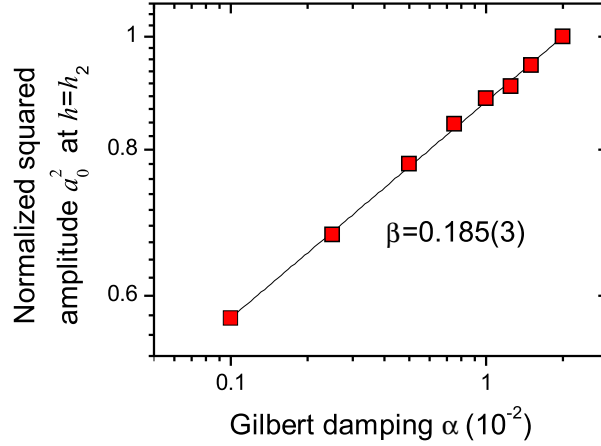


Figure 4.14: Double logarithmic plot of a_0^2 at $h = h_2$ versus α . Solid line shows a linear fit, which determines the scaling exponent β .

An alternative approach to describe the experimental findings is the framework of Bose-Einstein-Condensation (BEC). Considering magnetic systems, this process is known for magnons in YIG films [30] at room temperature (see chapter 2.3). Now we will briefly consider, what differences occur when the system, which undergoes a dynamic transition into magnon BEC, is confined. In the confined system investigated here, the geometrical eigenmode with the lowest frequency is practically degenerate with the FMR mode. Therefore, when exciting at the system with $\omega_{mw} = \omega_{00}$ at $P_{mw} < P_2$, no thermalization inside the eigenmode spectrum can be seen. Note that, as consequence of the spectral depletion¹⁴ of modes with frequency $\omega_{mn} < \omega_{00}$, scattering into modes with frequency $\omega_{mn} > \omega_{00}$ is suppressed. The bottom spin-wave mode has a frequency ω_{bottom} , which is detached from the rest of the discrete eigenmode spectrum. When trying to reach this mode via scattering processes respecting energy conservation, a high frequency mode at $\omega_h \approx 2\omega_{mw} - \omega_{bottom}$ must be present in the spectrum. This high frequency mode only exists, when the sample is strongly enough excited. Fulfilment of this condition enables the thermalization process, and the BEC formation. In contrast to extended systems, the FMR mode has a spatial structure. So one should expect that in a confined system the BEC formation is initiated, where the local amplitude of this mode has a maximum. A macroscopic (non-thermal) occupation certainly holds for the overpopulated mode discussed here. Experimentally, an oscillation angle of 17° was estimated at $P_{mw} = P_2$. In the simulation the

¹⁴ Edge modes are not considered here, because of the spatial separation from the center modes.

large amplitude of the overpopulated mode alone reduces the magnetization locally by 27% (at $h = 58$ Oe, $\phi = 16^\circ$) - magnon BECs in YIG never reach such amplitudes. The estimate of the wave length, and the alternative interpretation of the overpopulated mode as a standing spin-wave bullet imply that the mode profile is a standing wave pattern. This demands the presence of two waves at $k = \pm k_{bottom}$. At powers (of dynamic fields) much larger than the threshold, the coherence is lost, and the amplitude of the overpopulated mode decreases. This happens because the dynamics expand to locations where ω_{bottom} is different than in the center. Then, the BEC scenario breaks down.

4.2 Parametric instability

In the previous chapter, a non-linear FMR experiment with a laterally confined magnetic sample, patterned from a thin film, was discussed. The induced spin-wave instability processes are indirect. They require a strongly excited FMR mode. In contrast parametric excitation offers a way to directly pump energy into a potentially unstable mode. In a corpuscular picture, one can interpret the parametric excitation as a splitting of one microwave photon into two magnons. No intermediate magnons appear in this process. The chapter begins with a sample description and a determination of the eigenmode spectrum. Analytic and numerical methods are applied for this purpose. Based on these results, the experimental findings presented subsequently can be directly interpreted. Spectral, spatial, and temporal properties are discussed. The experimental results are published in [125]. Concerning in particular edge modes, further studies can be found in [109]. The combined action of spin-currents with parametric excitation is discussed in [38].

4.2.1 The sample

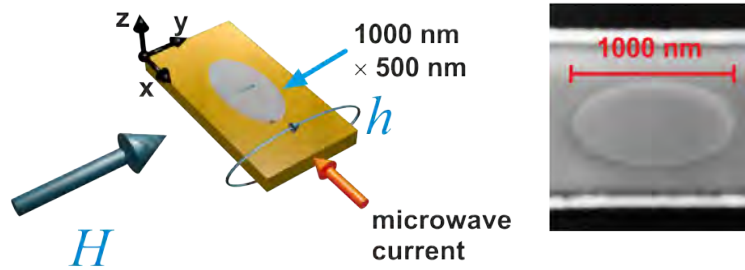


Figure 4.15: Sketch of the sample. On top of a Au microstripline, an ellipse was patterned from a Py thin film ($t = 10$ nm). The field H is applied along the short axis of the ellipse. The dynamic magnetic field h is parallel to the static field. Inset shows a SEM image.

The sample is structurally similar to the sample used for the FMR experiment (compare sketch in Figure 4.15 with Figure 4.1). The difference is that the microstripline is oriented in such a way that the static field \mathbf{H} and the dynamic field \mathbf{h} are collinear. The Py disc has a size of $0.5 \mu\text{m} \times 1 \mu\text{m} \times 10$ nm. For the experiments discussed in the following, a field of $H = 700$ Oe was applied. To avoid heating the microwaves were pulsed with pulse length 100 ns and period $2 \mu\text{s}$.

4.2.2 Eigenmode spectrum

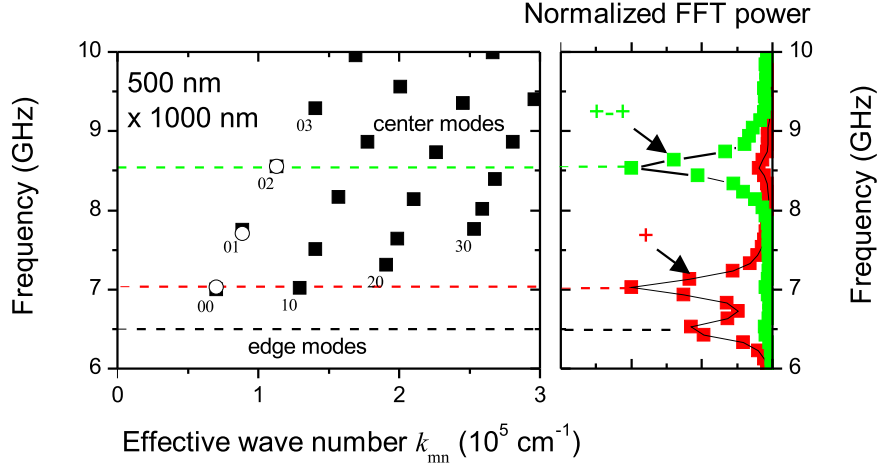


Figure 4.16: Left panel shows the eigenmode spectrum of the elliptical element with lateral size 500 nm \times 1000 nm. A field of $H = 700$ Oe is applied along the short axis. Closed symbols show analytically calculated, open symbols numerically calculated eigenfrequencies. Right panel shows two representative, numerical power spectra, from which the eigenfrequencies were extracted.

The eigenmode spectrum shown in Figure 4.16 was primarily calculated analytically (closed rectangles), based on the model outlined in chapter 2.2. Micromagnetic simulation (open circles), yields similar frequencies. In the simulation, the pulsed dynamics field $\mathbf{h} \perp \mathbf{H}$, which is not possible in the real experiment. To match the analytic model with the numerically obtained eigenfrequencies, an internal magnetic field of $H_{int} = 532$ Oe was assumed. An estimate based on [57] predicts $H_{int} = 585$ Oe in the center of a rectangular dot. For this value of the internal field, the resulting eigenfrequencies are typically more than 200 MHz larger. The additional reduction of H_{int} takes into account that (in the actually elliptical dot) on average, the field reduction is stronger than in the center. Note that the first quantization index m refers to the direction parallel to \mathbf{H} (short axis), whereas n refers to the direction perpendicular to \mathbf{H} (long axis). In the simulation, higher order modes were addressed by means of spatially inhomogeneous dynamic fields \mathbf{h} .

Using continuously applied (anti-)symmetric field $\mathbf{h} \perp \mathbf{H}$, the mode profiles shown in Figure 4.17(a,c,e) were determined. To highlight their spatial symmetries, the real part of the Fourier amplitude is shown, instead of the usual Fourier power. Note that at the edges, where the static demagnetizing fields in-

duce a strong reduction of the internal magnetic field, the dynamic amplitudes are strongest. One can also see in the power spectrum shown in Figure 4.16 a strong response connected with this edge mode. In reality, the roughness of the physical edges, altered magnetic properties etc., diminish the local susceptibility. Such local features can strongly influence the properties of edge modes (see [109]). If it would be possible to excite the eigenmodes in this way experimentally, a BLS measurement along the central x -sections would yield the curves shown in Figure 4.17(b,d,f). To emulate these sections from the complex Fourier profiles, Eq.(3.11) was evaluated for different x -positions of the laser spot.

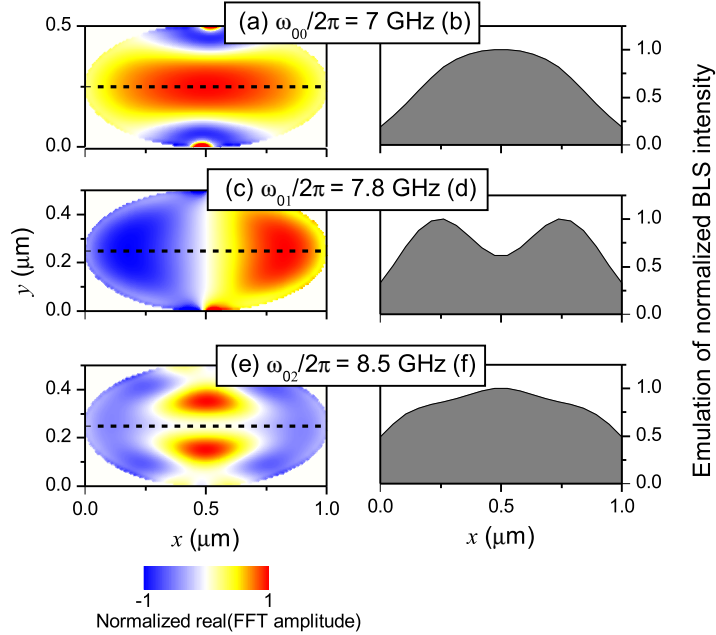


Figure 4.17: Numerically determined eigenmode profiles. In (a) the fundamental mode, in (c) the second order mode, and in (e) the third order mode are depicted in terms of the real part of the FFT amplitude. The corresponding central x -sections in (b),(d), and (f) represent an emulated BLS measurement.

4.2.3 Experimental results

Spectral properties

As explained in the introductory chapter 2.3.1 on parametric excitation, this phenomenon can be observed under two conditions: the microwave frequency has to be approximately twice the frequency of the addressed mode, and the dynamic field $h \geq h_{th}$ has to exceed the threshold defined by Eq.(2.30). To find a para-

metric response experimentally, the laser spot was positioned in the middle of the ellipse, and the microwave frequency ω_{mw} was swept within a certain interval, while the BLS intensity I_{BLS} at $\omega = \frac{\omega_{mw}}{2}$ was recorded.

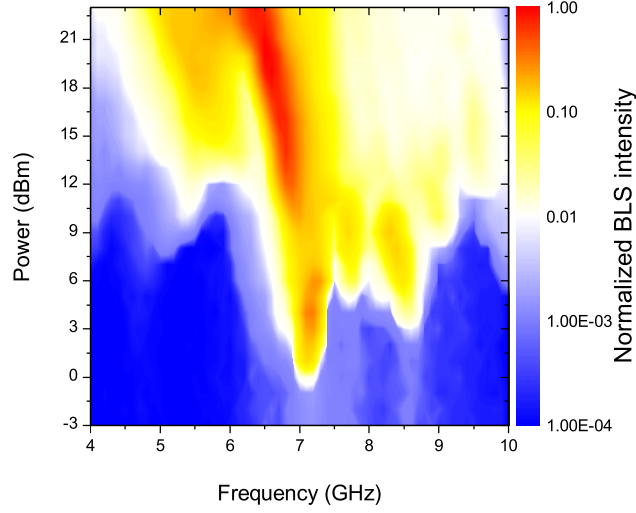


Figure 4.18: BLS intensity $I_{BLS}(\omega_{mw}/2)$ as a function of the microwave frequency and the microwave power P_{mw} .

In Figure 4.18 the experimental results are presented in a compact form. The color-coded two-dimensional map shows the BLS intensity at frequency $\omega_{mw}/2$ and microwave power P_{mw} . This map is essentially an experimental realization of the dynamic phase diagram shown in Figure 2.5 in chapter 2.3.1. Before the experimental data will be discussed in detail, one can already conclude that several different modes can be excited parametrically.

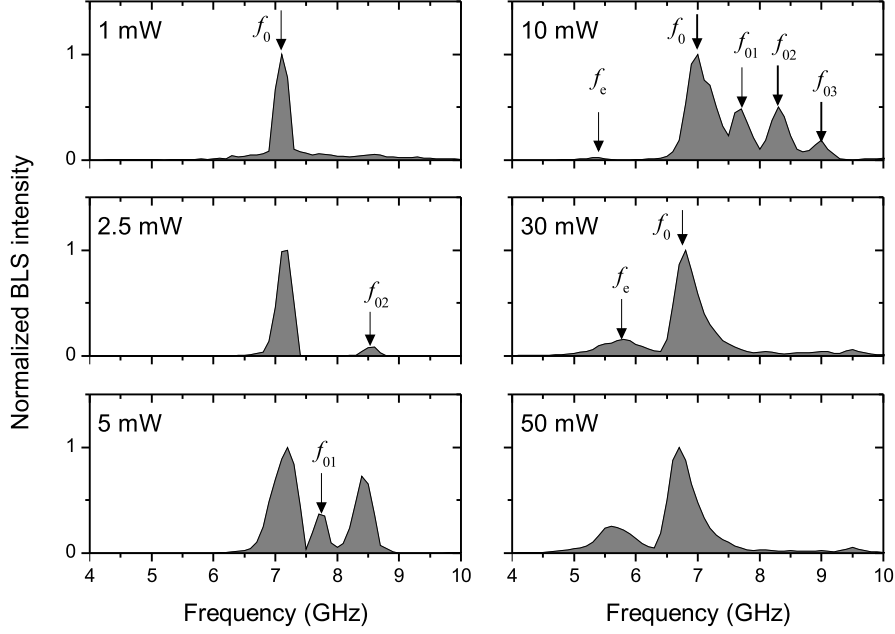


Figure 4.19: BLS intensity I_{BLS} at frequency $\omega = \frac{\omega_{mw}}{2}$ for different microwave powers P_{mw} as indicated. The appearance of a new spectral peak is indicated by the labelled arrows. These peaks can be related to different eigenmodes with indices mn .

For microwave power $P_{mw} < 1$ mW only the thermal agitation of the magnetic system was measured. The first indication of a parametric response occurs for $P_{mw} = 1$ mW. The corresponding spectrum is shown in Figure 4.19. The BLS intensity at 7 GHz is two orders of magnitude stronger than the thermal signal strength. When increasing the power, several additional peaks appear in the spectrum. At $P_{mw} = 10$ mW a set of 5 different spectral peaks can be distinguished. At larger power, only the two peaks with lowest frequency persist. An explanation of this behaviour will be given later. The labels indicate the quantization indices mn of the corresponding eigenmodes. Eigenfrequencies calculated by the analytic and numerical model match well with this assignment to the peaks in the experimental data.

Spatial properties

To support the assignment of the spectral peaks to different eigenmodes, spatial imaging of the dynamical mode profiles was performed. For this the pumping

frequency was set to $\omega_{mw} = 2\omega_{mn}$, and the microwave power to $P_{mw} = 10$ mW. At this power level, the largest number of different spectral peaks was found. The sample was scanned in the two lateral directions with a step size of 50 nm, covering the ellipse, while the BLS intensity $I_{BLS}(\omega_{mn})$ was recorded. The corresponding maps of BLS intensity are shown in Figure 4.20(a,c,e). These maps can be directly compared to the simulated profiles shown in Figure 4.17(a,c,e). Note that since in BLS the local spin-wave intensity is measured, the phase-information is lost.

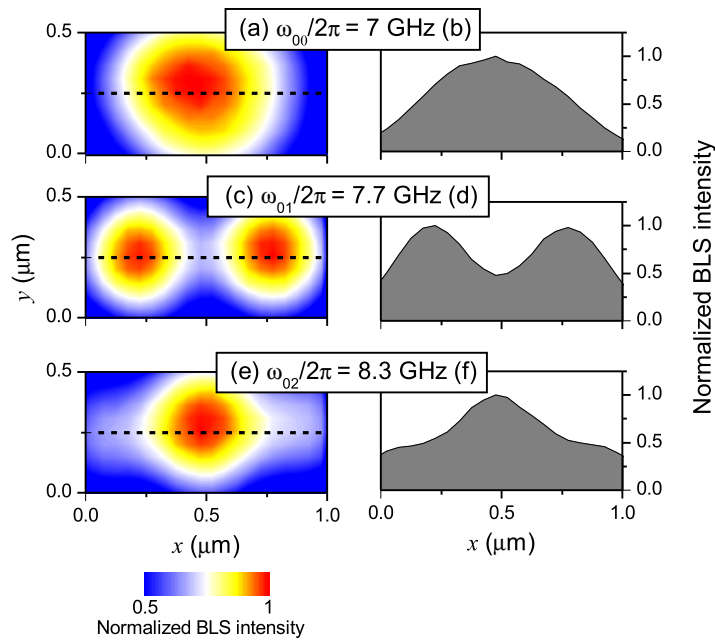


Figure 4.20: Mode profiles in terms of BLS intensity. In (a) the fundamental mode, in (c) the second order mode, and in (e) the third order mode are depicted. The corresponding central x -sections in (b),(d), and (f) represent an emulated BLS measurement.

Nevertheless, the experimental and numerical mode profiles clearly correspond to each other. Comparing the emulated sections in Figure 4.17(b,d,f) with the experimental sections in Figure 4.20(b,d,f) explains for example the local minimum of the BLS intensity in the center of the mode $m = 0$, $n = 1$ as a signature of a nodal line at $x = 0.5$ μm .

Temporal properties

As a characteristic of all instability processes discussed in this thesis, when exceeding the instability threshold $h_{th} \propto \sqrt{P_{th}}$, the unstable mode's amplitude grows

in theory exponentially $c_k \propto \exp \nu t$. When increasing the microwave power in the parametric excitation experiment, the FMR mode is the first to show a parametric response. To determine the exact threshold power, the temporal growth of the FMR mode was investigated, by means of a time-resolved BLS measurement. The onset of the microwave pulse initializes a time counter, which is stopped by a scattering event registered by the interferometer. In this way, each scattering event receives a time signature, yielding a time-resolved BLS spectrum. Technical restrictions do not allow to investigate processes on time-scales smaller than 1 ns. The data (BLS intensity at $\omega_{mw}/2$ as a function of time) shown in Figure 4.21(a) was obtained by setting $\omega_{mw} = 2\omega_{00}$ and $P_{mw} = 1$ mW. Obviously the microwave power already exceeds the instability threshold, but not by far. Therefore one can see a continuous increase in the BLS intensity during the full time interval of 100 ns, in which the pumping field was active.

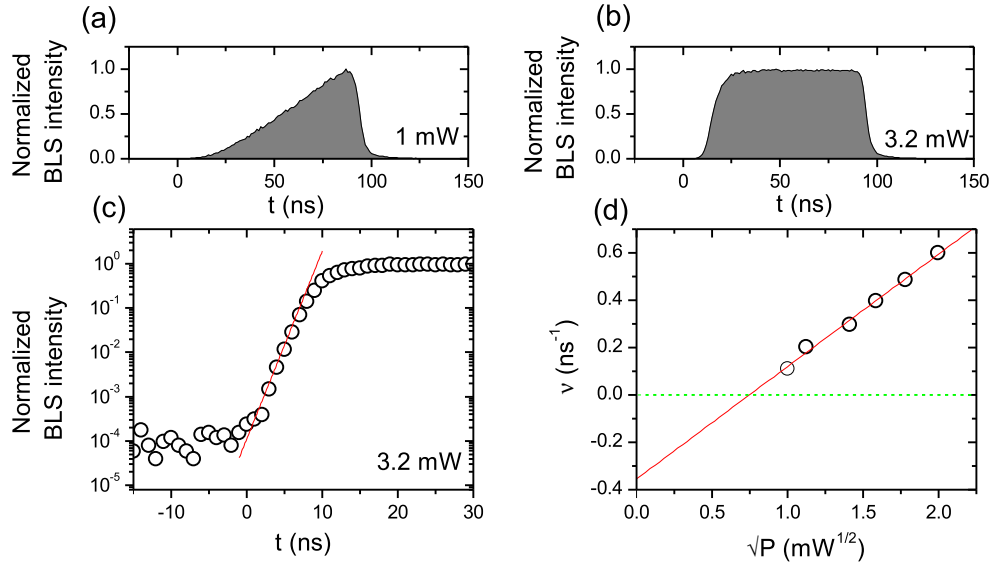


Figure 4.21: Temporal characteristics of parametrically excited FMR mode. (a) and (b) BLS intensity $I_{BLS}(t)$ for two different microwave powers P_{mw} as indicated. (c) Onset of parametric growth for $P_{mw} = 3.2$ mW. Note the log-scale. Red line is fitted to the data in order to determine the growth rate ν . (d) Growth rate ν as a function of \sqrt{P} . Red line is fitted to the data. The instability threshold P_{th} can be found where the red line intersects the dashed horizontal line.

For $P_{mw} = 3.2$ mW, the growth is much faster, as can be seen in Figure 4.21(b). The BLS intensity saturates after approximately 20 ns, 80 ns before the pumping pulse actually ends. The initial increase of the BLS intensity is indeed exponential, as the logarithmic plot of the rising edge and the linear fit to the data in Figure

4.21(c) demonstrates. Note that here the BLS intensity $I_{BLS} \propto |c_0|^2 \propto \exp(2\nu t)$ is proportional to the square of the dynamic amplitude. The fitted growth rate ν refers to the latter. In Figure 4.21(d) ν is plotted as a function of \sqrt{P} . This data reveal a linear dependence

$$\frac{1}{\tau} = m\sqrt{P} - B. \quad (4.3)$$

The theoretical considerations in chapter 2.3.1 allow to identify the slope $m = V_k A$ with a product of the coupling factor V_k and a calibration factor A of the stripline. From the analytic model, an estimate of the coupling factor $V_{00} \approx 1.6 \times 10^7 \text{ Oe}^{-1} \text{ s}^{-1}$ for the fundamental mode can be derived. The slope m then converts into a calibration factor of $A = 29(1) \text{ Oe} / \text{mW}^{1/2}$. Assuming an impedance of 50Ω , from the microstripline's geometry an estimate for A of $24 \text{ Oe} / \text{mW}^{1/2}$ can be made. This calculation demonstrates the conceptual validity of the analytic model introduced in chapter 2.2. The model is not only suitable to compute eigenfrequencies, but also provides a quantitatively correct description of the coupling process, which is determined by the ellipticity of the spin-wave modes. The higher order modes theoretically have coupling factors $V_{01} = 1.5 \times 10^7 \text{ Oe}^{-1} \text{ s}^{-1}$, $V_{02} = 1.3 \times 10^7 \text{ Oe}^{-1} \text{ s}^{-1}$, $V_{03} = 1.2 \times 10^7 \text{ Oe}^{-1} \text{ s}^{-1}$, all smaller than V_{00} . This explains the necessity of larger microwave powers in order to destabilize these modes.

The intercept $B = 0.36(3) \text{ ns}^{-1} = \omega_{r0} = \alpha \omega_0 \frac{\partial \omega_0}{\partial \omega_H}$ can be identified with the relaxation frequency, and solved for the Gilbert damping constant, yielding $\alpha = 0.0037(3)$. This value is significantly smaller than values ($\alpha = 0.008$ [105]) typically deduced from FMR linewidth measurements obtained from infinitely extended Py films. The exact instability threshold power $P_{th} = \frac{B^2}{m^2} = 0.6(1) \text{ mW}$ follows from the condition of a vanishing growth rate.

Non-linear dynamical processes

The dynamical state at powers much larger than the threshold is most complex. Here only a particular aspect will be discussed: at intermediate microwave powers, the measured BLS intensity of the FMR mode shows a non-monotonous behaviour. It will be shown that this experimental finding results from a competition between several, approximately degenerate modes.

When following the evolution of the BLS intensity of the FMR mode from P_{th} to larger powers (see Figure 4.18 and Figure 4.22(a)), a drop of the BLS intensity can be seen around 8 mW. The theoretical considerations in chapter 2.3.1 suggest that this finding can be interpreted as a signature of a competition between several

eigenmodes.

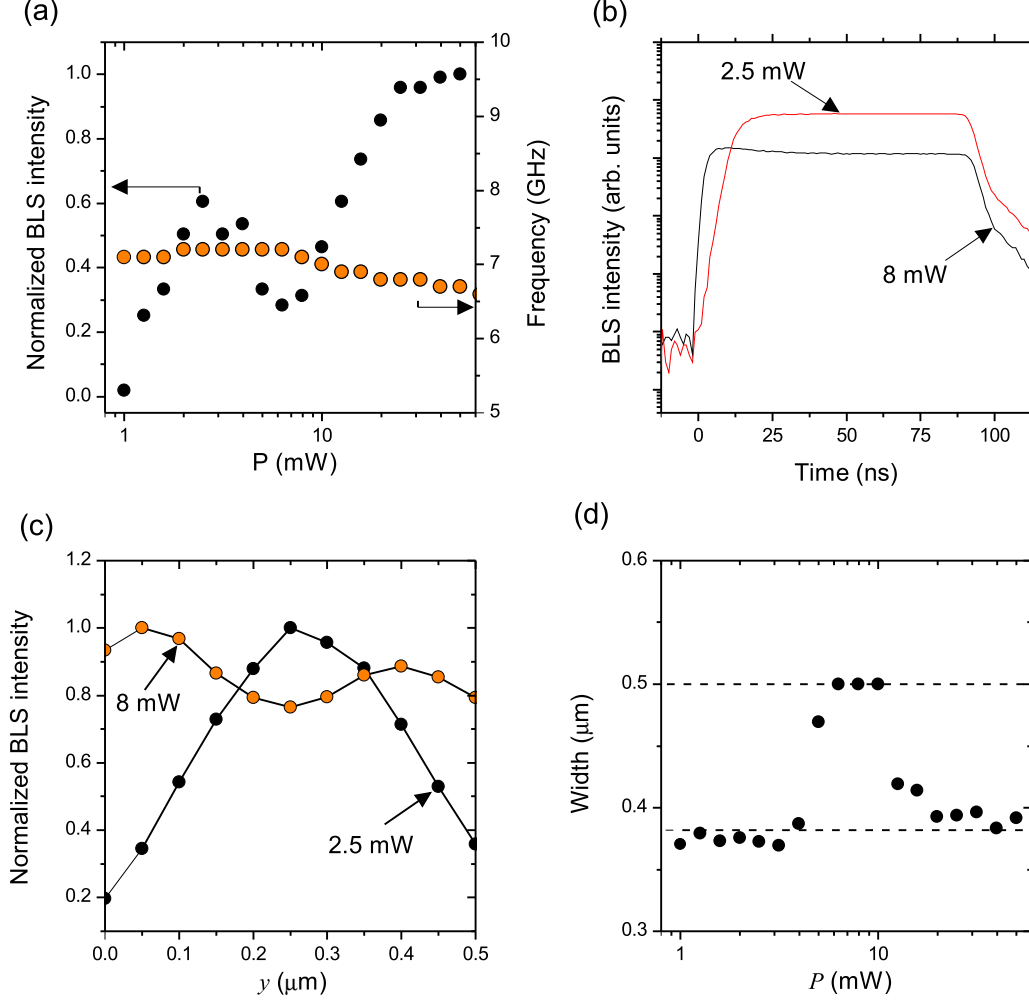


Figure 4.22: Spectral and spatial transformations of the FMR mode above the parametric excitation threshold. (a) Power dependence of the BLS intensity $I_{BLS}(\omega_{mw}/2 = \omega_{00})$, and power dependence of the FMR frequency. (b) Time-dependence of the BLS intensity $I_{BLS}(\omega_{mw}/2 = \omega_{00})$ for two different powers as indicated. (c) Central x -section through FMR mode profile for two different powers as indicated. (d) Power dependence of the profile's width in terms of their FWHM.

The temporally resolved BLS intensity shown in Figure 4.22(b) demonstrate that the linear stage (the first few ns) is not affected by the competition process. Initially, the individual modes simply grow exponentially, and do not yet interact. Therefore the rising edge of the temporally-resolved BLS intensity increases faster with larger microwave power. In contrast, on a longer time scale, the competition

manifests. For $P_{mw} = 8 \text{ mW}$, the stationary BLS intensity established after 25 ns is smaller than the stationary signal for $P_{mw} = 2.5 \text{ mW}$. Note that if the energy pumped into the system is split between several modes (FMR mode and higher order modes), the BLS signal decreases, because the light scattered from higher order modes is less efficiently recollected by the objective lens, than light scattered from the FMR mode ($\sigma_{mn} < \sigma_{00}$).

The spatially resolved BLS measurements provide further evidence for the above interpretation of a multi-mode competition. For small powers, the y -section shown in 4.22(c) depicts the expected sinusoidal profile, whereas at larger powers, when the competition occurs, the sections reveal a flat profile.¹⁵ This can be interpreted as a result of the superposition of the FMR mode with higher order modes. The power dependence of the profile's width shown in 4.22(d) is clearly correlated with the decrease in BLS intensity. The calculation of the eigenfrequencies (see 4.16) further supports the idea of mode competition, by predicting that the eigenfrequencies $\omega_{10} \approx \omega_{00} \approx \omega_{20}$.

At larger power, the competition regime is left again. The power dependence of the FMR frequency shows a decrease, starting at $P_{mw} = 8 \text{ mW}$ (see Fig. 4.22(a)). The usually suspected process responsible for this behaviour is the negative non-linear frequency shift mechanism. The fact that this mechanism manifests experimentally at powers for which the measured BLS intensity is actually decreased, can only be explained by large dynamic amplitudes in modes with low effective scattering cross section σ_{mn} . The decreased effective magnetization implies an increased intermodal frequency separation. Then, the difference in the growth rates ν_{mn} becomes more pronounced, and the competition is suppressed.

The higher order modes with $m = 0$, $n = 1, 2$ completely disappear in the spectrum for powers above 10 mW. They likely enter a similar competition regime as the FMR mode. For them, a larger set of concurring higher order eigenmodes is available (see 4.16). Therefore they can not simply evade from this competition by means of the negative non-linear frequency shift.

4.2.4 Discussion

The experimental data demonstrate that parametric excitation is an important tool for the investigation of eigenmode spectra of confined magnetic elements. In particular spatially antisymmetric eigenmodes can in principle not be excited by uniform fields $\mathbf{h} \perp \mathbf{H}$, as used in a FMR experiment. Only in numerical experiments, fields with arbitrary spatial symmetry can be easily implemented and

¹⁵ x -sections stay sinusoidal for all powers.

allow to address such modes. But even then, excitation of a pure eigenmode is not possible. This can be seen, when comparing the mode profiles of the mode with $m = 0$, $n = 2$, as obtained numerically (Fig. 4.17), and experimentally (Fig. 4.20). Although the overall shape of the emulated section is qualitatively similar to the experimental section, the central maximum appears to be much stronger in the experiment. One can interpret this difference as a consequence of a simultaneous excitation of the mode with $m = 2$, $n = 2$ in the simulation. The resulting superposition explains, why the Fourier amplitude vanishes in the center, and why the central peak of the emulated BLS section is smaller than the central peak found in the corresponding experimental section, where only the pure eigenmode with $m = 2$, $n = 2$ was excited.

The lateral confinement of the magnetic element on a micrometer scale allowed to use lithographically defined antenna structures. Their small dimensions and good impedance matching enables large dynamic fields in the immediate vicinity of the antenna, at relatively small microwave power. Due to the reduction of the threshold power to less than 1 mW demonstrated here, a practical application, like parametric amplification within a spintronic device becomes feasible.

The most surprising result of the discussed experiments, is the smallness of the damping constant derived from the power dependence of the exponential growth rate ν . The interpretation which will now be given, argues that in a parametric instability process, a true normal mode goes unstable, whose relaxation frequency only reflect extrinsic losses. Further experimental support of this argument can be found in [100], in conjunction with dissipation parameters experimentally derived from second order Suhl instability process in a Py film. There, a Gilbert damping constant related to the unstable spin-waves of only $\alpha = 0.0046$ was found, in contrast to $\alpha = 0.0072$ corresponding to the FMR linewidth of the same film.

In an ideal case, the properties of the sample are spatially invariant. As shown in chapter 2.2, in a laterally confined sample orthogonal normal modes with frequencies ω_{mn} can be introduced. The definition of a normal mode implies that the linewidth of each mode only reflects the coupling to the lattice. In a metallic system like Py these extrinsic losses are dominated by electron-magnon scattering (see chapter 14.2.5 in [47]). Spatial inhomogeneities, such as anisotropy fluctuations due to grain structures in polycrystalline films, or dipolar fields induced at rough edges or surfaces, can formally be treated as a mediator for a coupling of the normal modes.

If one knows all spatial details about the irregularities, one can in principle also determine the true normal modes of the inhomogeneous system. Consider now the case of small enough inhomogeneity, when the true normal modes $c'_{mn} = \sum_{ij} \mu_{ij} c_{ij}$

can be written as a linear sum of the normal modes c_{mn} referring to a homogeneous system with identical geometry, and c'_{mn} retains the dominant spatial symmetry of c_{mn} ($\forall ij \neq mn, |\mu_{mn}| \gg |\mu_{ij}|$). This in particular implies that the FMR mode ($m = n = 0$) is mixed into the higher order modes.¹⁶ It was stated earlier in the thesis that even in the ideal case of no spatial inhomogeneities, all symmetric modes respond to the homogeneous field applied in a FMR experiment. Due to the mixing, the strength of this response will now increase. The practically measured linewidth reflects the superposed susceptibility of all of the true normal modes c'_{mn} . Theoretical models [89, 69] allow to quantify this two-magnon scattering contribution to the linewidth.

In contrast, during the course of an instability process, only a single true normal mode (the one with largest growth rate ν) goes unstable. Since by definition, for a true normal mode, the relaxation is only connected with extrinsic losses, the damping parameter α inferred from e.g. the temporal behaviour, must be smaller than inferred from the linewidth obtained by an FMR experiment. This explains the abnormally small dissipation parameter of $\alpha = 0.0037$ determined here, and found in other experiments [100].

¹⁶ The eigenfrequencies will be renormalized as well. A small perturbation implies that $\omega'_{mn} \approx \omega_{mn}$.

4.3 Spin current-induced instability

In this chapter magnetization dynamics in a novel kind of spin-transfer oscillator are investigated. In the spin-Hall nano-oscillator (SHNO), magnetic dynamics are induced by means of pure spin-currents, generated by the spin-Hall effect. The important feature of this structure is the realization of a local spin-current injection. To understand this properties in detail, the structure is modelled numerically by a three dimensional finite-element method. This modelling allows to determine a) the charge current distribution, b) the corresponding Oersted field, c) the temperature increase due to Joule heating, and d) the local polarization and strength of a spin current due to the spin-Hall effect. The analysis of experimental data obtained by BLS begins with spectra obtained for currents below the onset of instability. An analytic description based on the fluctuation-dissipation theorem will be introduced. This model is suitable up to the onset of instability. Subsequently, the spin-current induced instability is analysed. The experimental data suggest that the unstable mode is a standing spin-wave bullet. Finally, micromagnetic modelling is presented, which confirms this interpretation.

The experimental results were published in [28], the simulations in [122]. Additional investigations of parametric synchronization of a SHNO are discussed in [24].

4.3.1 The sample

Figure 4.23(b) shows a sketch of the SHNO. It consists of a circularly patterned Pt/Py bilayer, with triangularly shaped Au electrodes on top. From SEM measurements¹⁷ shown in Figure 4.23 (b), the rounding radius of the Au electrode tips was estimated to be about 50 nm. The gap between the electrodes spans 100 nm. The structures were manufactured by S. Uraszdin. Details about the fabrication can be found in [28].

¹⁷ SEM images were made in the Institute of Material Physics (WWU Münster) by R. Schlesiger under supervision of D. Baither and G. Schmitz.

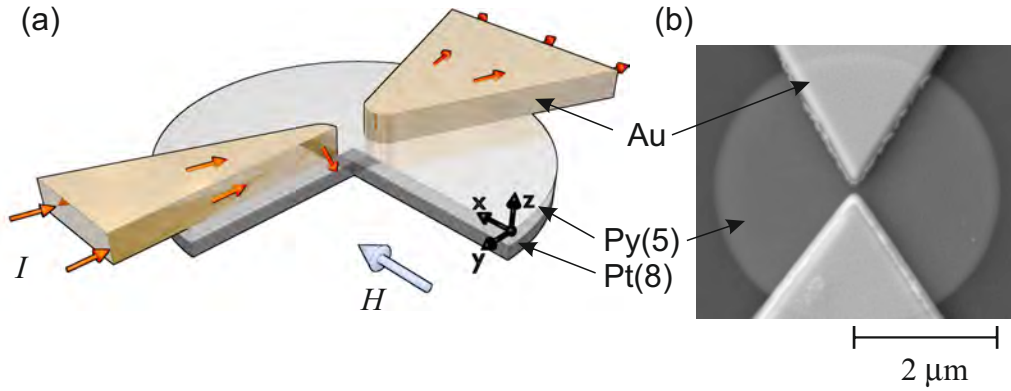


Figure 4.23: (a) Sketch of the investigated SHNO. Red arrows indicate the charge current. One quarter is left out for illustration purposes. The Au electrodes have a thickness of 150 nm, the Py layer has a thickness of 5 nm, and the Pt layer a thickness of 8 nm. (b) SEM image of the SHNO. Looking from above, the Py layer is imaged.

Charge current

The three dimensional distribution of the charge current density \mathbf{j}_c inside the SHNO was determined using the finite-element software package COMSOL Multiphysics,¹⁸ which solves Maxwell equations. For the electrical current flow, the relevant material parameter is the conductivity. Values valid for the considered sample were provided by S. Urazhdin ($3.1 \cdot 10^6 \text{ S/m}$ for Py, and $9.1 \cdot 10^6 \text{ S/m}$ for Pt). In contrast to the materials in the bilayer, the Au electrodes were modelled with a much larger conductivity of $4.1 \cdot 10^7 \text{ S/m}$.¹⁹ In the numerical model one Au electrode is subject to an incoming current ($I = 16 \text{ mA}$ entering the left electrode in Figure 4.23), the other electrode is grounded. The computed current distribution shows that the current stays as long as possible in the Au electrodes, till it reaches the gap in the center of the structure. Then it flows down into the Py/Pt bilayer. Due to the different conductivities, the current is stronger concentrated in the Pt layer than in the Py layer. The current density inside the Pt layer is shown in Figure 4.24.

¹⁸ www.comsol.com

¹⁹ Taken from the COMSOL material library.

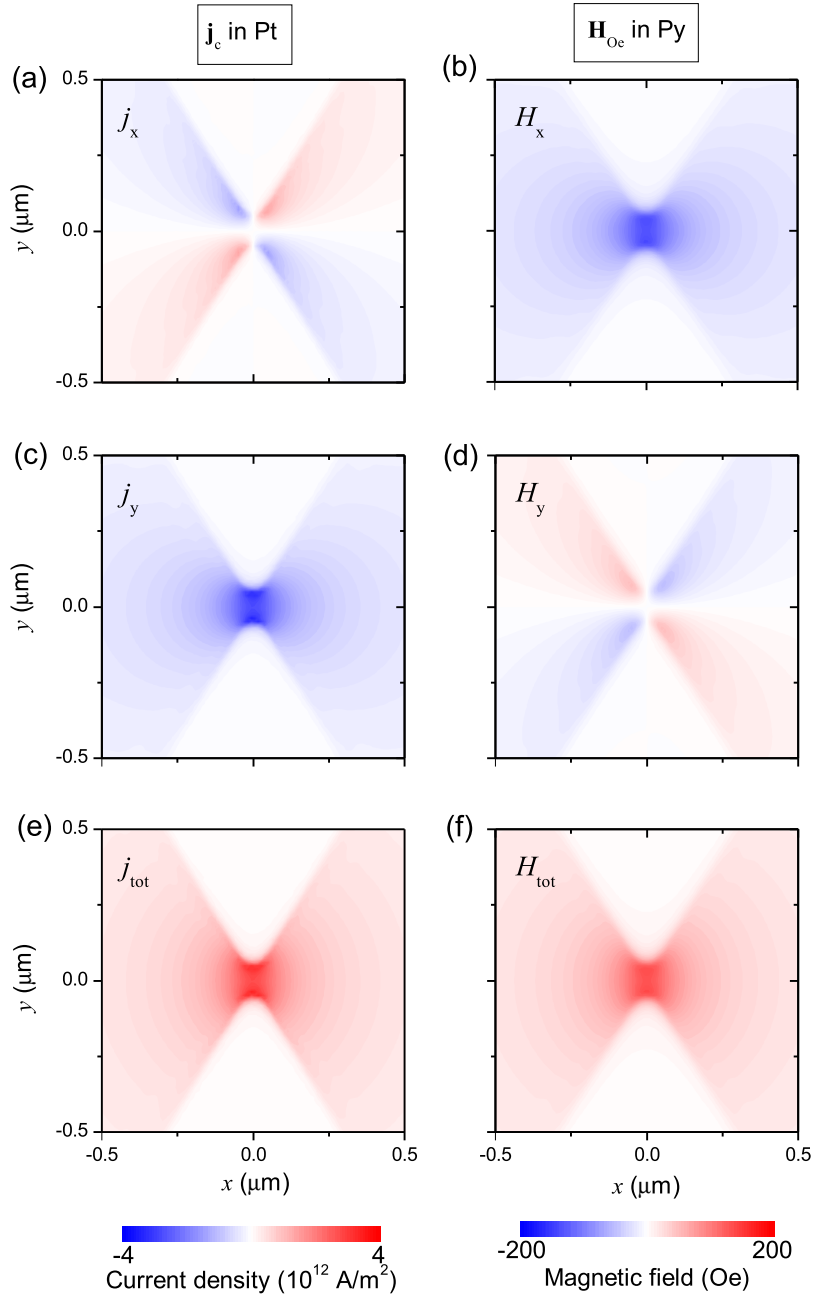


Figure 4.24: (a), (c), (e) Charge current density in the Pt layer, (b), (d), (f) and corresponding Oersted field.

A maximum current density of $3.5 \cdot 10^{12} \text{ A/m}^2$ is established where the current enters or leaves the Pt layer. In Figure 4.25 the current density along a central x -section in the Pt, and a vertical section through the double layer in the cen-

ter are shown. In the x -direction, a Lorentzian distribution with a FWHM of 250 nm approximately describes \mathbf{j}_c . In contrast in the y -direction, the electron's presence in the Pt is restricted to the region inside the gap. The vertical section demonstrates that more than 80% of the current flows through the Pt.

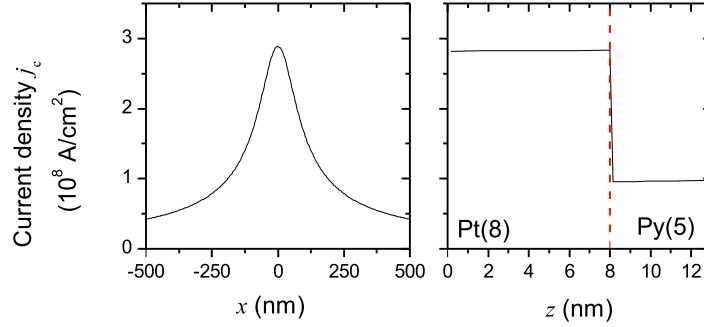


Figure 4.25: (a) Central x -section through charge current density in the Pt layer, (b) vertical section in the center of the gap. The data refers to $I = 18 \text{ mA}$.

Magnetic field

The Oersted field \mathbf{H}_{Oe} inside the Py layer, generated by the charge current density \mathbf{j}_c in the Pt layer, was calculated by numerical integration, using Biot-Savart law:

$$\mathbf{H}_{Oe}(\mathbf{r}) = \frac{1}{4\pi} \int_V \mathbf{j}_C(\mathbf{r}') \times \frac{\mathbf{r} - \mathbf{r}'}{|\mathbf{r} - \mathbf{r}'|^3} d\mathbf{r}'. \quad (4.4)$$

Figure 4.24 shows that the Oersted field is opposed to the static field, and approximately rotated by 90 degree in comparison to \mathbf{j}_c , as a consequence of the cross product in Eq. (4.4). At the typical current of 16 mA, a maximum local reduction of 140 Oe is induced in the gap. Consider for comparison a point-contact STNO, where a current of similar magnitude flows through a circular area whose in-plane dimension is one order of magnitude smaller. Accordingly, local Oersted fields of about 1 kOe will be induced. Thus in the SHNO the influence of the Oersted field is much weaker than in STNOs.

Spin current

As outlined in chapter 2.3, when electrons are scattered in Pt, the action of spin-orbital coupling leads to a correlation of the scattering direction and the spin-orientation of the electron. Considering electrons scattered upwards (into the

z -direction), the spin has a large probability to lie in the x - y -plane. A transverse spin imbalance can built up and diffuse into the Py, so that one may speak of a transverse spin current density \mathbf{j}_s , which is locally proportional to the magnitude of the lateral charge current density \mathbf{j}_c in the Pt layer. The polarization \mathbf{p} of the transversally flowing spin current is orthogonal to \mathbf{j}_c and \mathbf{e}_z . Inside the gap, $\mathbf{j}_c \parallel -\mathbf{e}_y$, therefore $\mathbf{p} \parallel -\mathbf{e}_x$. Figure 4.26 shows the magnitude j_s of the spin current density, and polarization \mathbf{p} in the gap region.

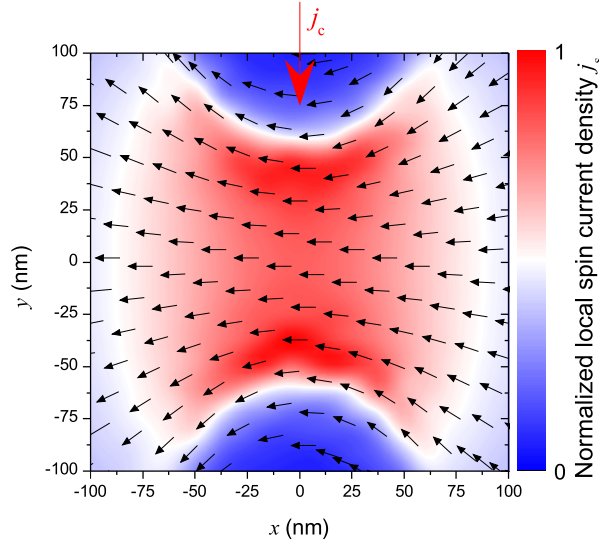


Figure 4.26: Spin current density j_s (color-coded two-dimensional map) and polarization \mathbf{p} (arrows) entering the Py layer.

The spin current causes a spin-transfer torque (STT), which acts on the magnetization in the Py. The typical spatial scale of the region where the STT acts is the same as the characteristic size of the charge current distribution - about 250 nm.

Joule heating

When a charge current flows, the electrical resistance leads to a temperature increase ΔT . This Joule heating can be significant. Apart from an accelerated degradation of the structure, in a magnetic system one has to take care, that the temperature stays well below the Curie temperature. In order to estimate the magnitude of the Joule heating, the COMSOL model of the SHNO was extended

by heat flow equations. A thermal bath is connected to the metallic structures, by inclusion of the sapphire substrate, which is assumed to be at the bottom at room temperature. Figure 4.27 shows the stationary temperature increase ΔT in the Py layer, at a typical current of $I = 16$ mA. Inside the gap, a maximum increase of 20 K can be seen. For comparison, the Curie temperature of Py is about 750 K. The calculation thus demonstrates that Joule heating in SHNOs is not significant.

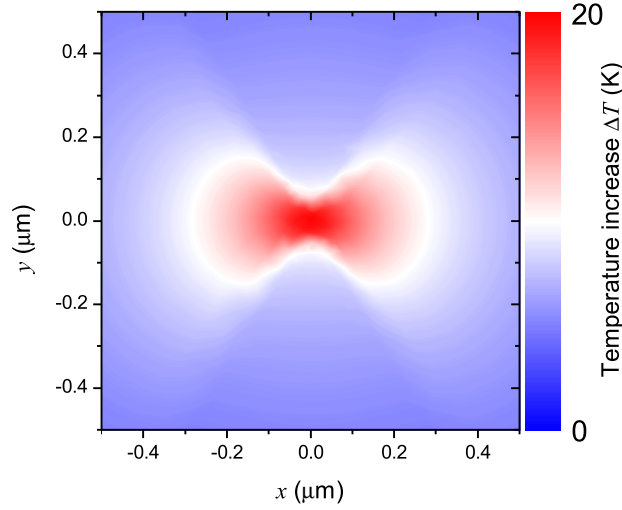


Figure 4.27: Effect of Joule heating in a SHNO. Temperature increase ΔT inside the Py layer for $I = 16$ mA.

4.3.2 Thermal fluctuations under the influence of STT

No STT

To study how a spin current influences thermal magnetic fluctuations in the SHNO, the laser spot is positioned inside the gap, and the current is gradually increased from zero. I will start the analysis of the experimental data, with the spectrum obtained for $I = 0$ mA. The BLS spectrum for $I = 0$ mA, and $H = 900$ Oe is shown in Figure 4.28(a).

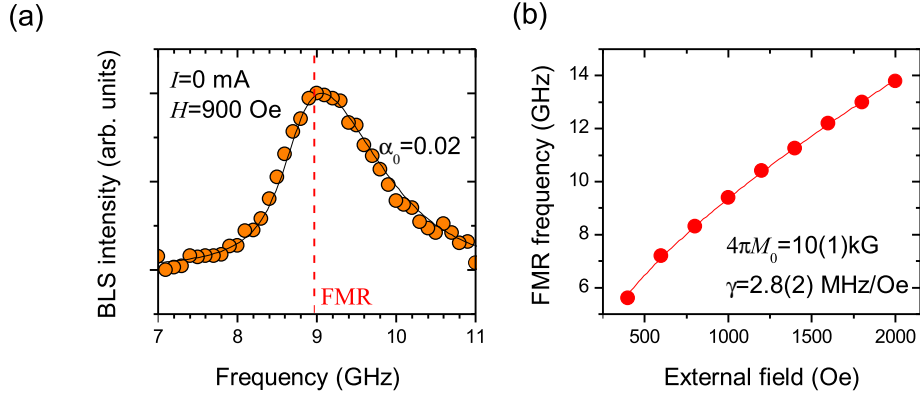


Figure 4.28: Thermally activated magnetic fluctuations in the SHNO, measured by BLS. (a) Dots shows the spectrum for $H = 900$ Oe, when no current is applied. Solid line is a calculated spectrum. The vertical dashed line marks the maximum BLS intensity, which can be associated with the FMR frequency. (b) Dependence of the FMR frequency (dots) on the applied field. Solid line is a fit of the Kittel formula (2.3).

Since we consider a thin Py films, the maximum intensity at 9 GHz can be associated with the FMR frequency ω_0 . This is a direct result of the small initial slope of the Backward Volume modes in thin Py, which implies that $\omega_{bottom} \lesssim \omega_0$. Repeating the measurement for different fields H yields the dependence of $f_0 = \omega_0/2\pi$ on H shown in Figure 4.28(b). This data can be described by the Kittel formula Eq.(2.3), which allows to determine the saturation magnetization $4\pi M_0 = 10(1)$ kG, and the gyromagnetic ratio $\gamma/2\pi = 2.8(3)$ MHz/Oe. Within their error bars, these values equal the standard values for Py listed in table 1.

A thermal spectrum can theoretically be calculated (see [117]) from these parameters,²⁰ by applying the fluctuation-dissipation theorem. It states that the power spectral density of the fluctuations $S(\omega)$ is proportional to the imaginary part of the susceptibility χ'' , multiplied by a statistical occupation factor n . The Py film is patterned into a disc with a diameter of $4\mu\text{m}$. The quantization of the wave number results in a discrete spectrum as described in chapter 2.2. The relatively large size, compared to the structures investigated in chapter 4.1, implies a large density of states, which therefore approximates the density of states in an infinitely extended film. As explained in chapter 2.2, each resonance mode contributes to the full susceptibility $\chi(\omega) = \sum_{mn} \chi_{mn}(\omega)$. Spin waves are bosons, therefore the occupation statistics n_{mn} of each mode is described by

²⁰ For the missing exchange constant I assume the standard value given in table 1.

$$n_{mn} = \frac{1}{\exp\left\{\frac{\hbar\omega}{k_B T}\right\} - 1}. \quad (4.5)$$

In micro BLS, the sensitivity to small wave length modes is limited by the properties of the objective lens, as explained in chapter 3.1. This limitation can be taken into account by a factor σ_{mn} given by Eq. (3.11). The laser light field in the SHNO is masked by the Au leads. This mask Υ enters Eq. (3.5) as a prefactor of the light field $E(\mathbf{r})$:

$$I_{sc}(\mathbf{q}) = \left| \int d^2\mathbf{r} m(\mathbf{r}) \Upsilon(\mathbf{r}) E(\mathbf{r}) e^{i\mathbf{q}\mathbf{r}} \right|^2. \quad (4.6)$$

Finally, the optics inside the interferometer lead to an additional convolution of the scattered light spectrum with the instrumental function $\mathcal{I}(\omega) \approx A\mathcal{T}(\omega)^6$. For \mathcal{I} , a FWHM of 300 MHz is assumed. Putting together Eqs. (4.6), (3.11), (2.16) and (4.5) yields for the power of the fluctuations $S(\omega)$, when measured by micro BLS:

$$S(\omega) = A \left[\sum_{mn} \sigma_{mn} n_{mn}(\omega) \chi''_{mn}(\omega) \right] (\omega) * \mathcal{I}(\omega), \quad (4.7)$$

with A being the amplitude parameter, which models all unknown factors. Note that Eq. (4.7) does not take into account the ellipticity of the magnetic precession. In the thin film system considered here, the ellipticity hardly changes within the accessible wave number range, therefore it can be neglected.

In order to determine σ_{mn} a numerical scheme is used. For this, the film was discretized into 200×200 cells. A quadratic instead of a circular geometry was used, which allows to use Eq.(2.12) to compute ω_{mn} . Modes up to $m = 80$ and $n = 60$, whose scattered light is not collected by the objective lens anymore, were taken into account. Spatially antisymmetric modes were shifted by a quarter wave length in order to maximize their contribution. This is allowed, because the propagation length is for all modes $\xi_{mn} < 4 \mu\text{m}$, and therefore coherence throughout the whole structure cannot be expected. In this regard, the quantization scheme is only a formal approach to sample the dispersion manifold. All integrals, Fourier transformations and convolutions appearing in Eq.(4.7) were evaluated numerically. The final result of the computation is the solid line shown in Figure 4.28(a). The only parameter to be adjusted (apart from the amplitude parameter A) to obtain a good matching with the BLS data, is the damping constant. The value $\alpha_0 = 0.02$ of the damping constant is relatively large compared to the standard value of 0.008 for Py, but indeed typical for thin Py on Pt [4, 77].

Finite STT

When a non-zero current is applied, the spectra transform significantly, as can be seen in Figure 4.29. Generally, for $I > 0$ mA the BLS intensity increases in the low frequency region. This means that the small wave length dipolar part of the spectrum is stronger affected by the spin current, than the high frequency exchange part, in agreement with the theoretical considerations outlined in chapter 2.3. In addition, the maximum intensity shifts to a smaller frequency. This negative frequency shift has two origins: first-of-all, the usual negative non-linear frequency shift mechanism, as discussed in chapter 4.1. Secondly, the charge current induces an Oersted field H_{Oe} , which is anti-parallel to the applied field, thereby reducing the frequencies of magnetic oscillations.

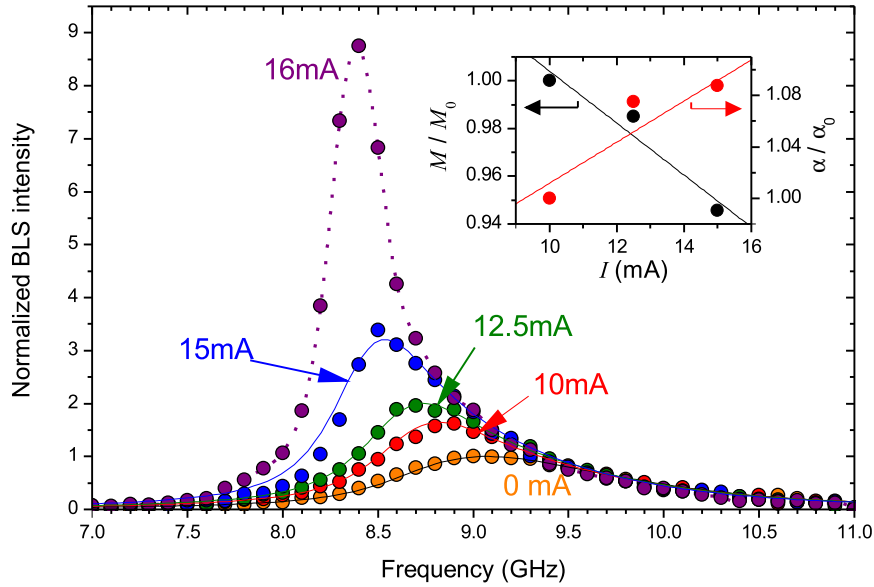


Figure 4.29: Thermal magnetic fluctuations under the influence of a spin current. BLS spectra (dots) for different currents as indicated. Solid lines show calculated spectra. The inset shows the parameters used for this calculations.

The energy, which is pumped into the magnetic system by the spin current can be characterized by integrating the BLS intensity over the frequency. This integral intensity is shown in Figure 4.30. The inverse of this quantity clearly demonstrates a divergence at a critical current of $I_1 = 16$ mA.

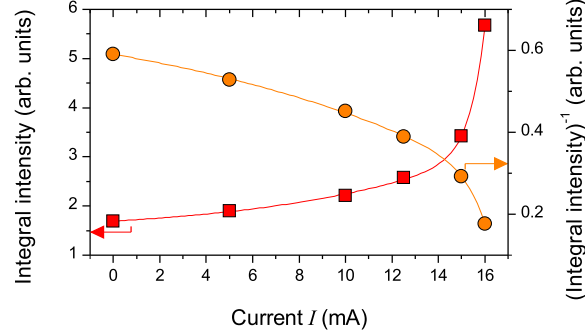


Figure 4.30: Dependence of the (inverse) integral intensity on the current I . Lines as a guide to the eye.

The formalism for the numerical computation of the thermal BLS spectrum can be extended to the case of non-vanishing current. For this, one has to take into account radiative losses R and the STT by the substitutions

$$\text{in Eq.(2.16): } \omega_{r,mn} + R_{mn} - \beta_{av} \text{ for } \omega_{r,mn}, \quad (4.8)$$

$$\text{in Eq.(4.5): } T \frac{\omega_{r,mn} + R_{mn}}{\omega_{r,mn} + R_{mn} - \beta_{av}} \text{ for } T. \quad (4.9)$$

The radiative losses $R_{mn} = \frac{\partial \omega_{mn}}{\partial k_{mn}}/s$ (see supplement to [28]), with $s = 0.61 \frac{\lambda}{NA}$ characterizing the laser spot size. β_{av} is the effective strength of the STT-term, averaged within the lateral area probed by the laser. This approach explicitly models the measurement. The spectrum for $I = 10$ mA is shown in Figure 4.29. In the analytic model, the Oersted field induced by the charge current can be taken into account by a decreased internal magnetic field. At $I = 10$ mA, a reduction of 11 Oe was estimated by averaging the calculated Oersted field inside the area probed by the laser spot. The values for α_0 and M_0 were taken from the fitting of the spectrum for $I = 0$ mA (see 4.28(a)). Note that no further adjustment of the global amplitude factor A is necessary. In order to fit the modified Eq.(4.7) to the experimental data, the strength of the STT was adjusted to $\beta_{av} = 880$ MHz. To judge whether this value is reasonable, an average value of

$$\beta_{av} = \frac{\int d^2\mathbf{r} j_c(\mathbf{r}) E(\mathbf{r}) \Upsilon(\mathbf{r})}{\int d^2\mathbf{r} E(\mathbf{r}) \Upsilon(\mathbf{r})} \frac{\phi_H g \mu_B}{2e M_0 t} \approx 970 \text{ MHz}, \quad (4.10)$$

with $E(\mathbf{r})$ given by Eq. (3.3), and $j_c = |\mathbf{j}_c|$ can be estimated for $I = 10$ mA, assuming $\phi_{H_H} = 0.07$. The value taken for ϕ_{H_H} is typical for Pt/Py systems (see [4, 77]). The matching of the fitted $\beta_{av} = 880$ MHz with the above estimate of

970 MHz supports the validity of the analytic model.

When further increasing the current to $I = 12.5$ mA, β_{av} and the reduction of H are assumed to grow linearly. In this respect, without further adjustments, the negative shift of the maximum BLS intensity is stronger than expected from the change of H . Therefore one has to decrease the magnetization to $M = 0.985M_0$. The physical mechanism responsible for this decrease is negative non-linear frequency shift. The correct global amplitude is obtained by increasing the damping constant to $\alpha = 1.075\alpha_0$. Both adjustments are in line with the general model [112] of STT-induced magnetization oscillations, and experimental observations [27]. For $I = 15$ mA, a good fitting to the experimental data is obtained for $\alpha = 1.0875\alpha_0$ and $M = 0.945M_0$.

At $I = 16$ mA Eq. (4.7) cannot be fitted to the experimental data. Extrapolation of α and M based on the preceding values underestimates the maximum BLS intensity by a factor of about two. This failure suggests that instead of having STT enhanced thermal fluctuations, to which all possible modes contribute, a particular mode goes unstable. This mode drags off the spin current from the other modes. Such a picture explains the diverging dependence of the (inverse) integral BLS intensity on the current, shown in Figure 4.30.

4.3.3 Instability

The analysis of the experiment proceeds now with data obtained for currents $I \geq 16$ mA. The data is shown in 4.31(b) and (c). As explained in the previous section, the system now reaches the point of damping compensation. A small increase in the current from $I = 16$ mA to $I = 16.1$ mA $= I_c$ causes a significant transformation of the BLS spectrum: suddenly a secondary peak at $\omega_b/2\pi = f_b = 7.8$ GHz $< \omega_0/2\pi = f_0 = 8.2$ GHz appears. The peak intensity $I_{BLS}(\omega_b)$ quickly increases with the current, as can be seen in Figure 4.31(c). At currents $I \geq 16.2$ mA, $I_{BLS}(\omega_b) > I_{BLS}(\omega_0)$. With other words, the dynamical mode attributed to the peak at ω_b then dominates the dynamics. The intensity of the other modes even decreases, as can be seen in Figure 4.31(c). The frequency ω_b of the dominant mode continuously decreases with increasing current (see Fig. 4.31(d)), whereas the peak intensity $I_{BLS}(\omega_b)$ saturates.

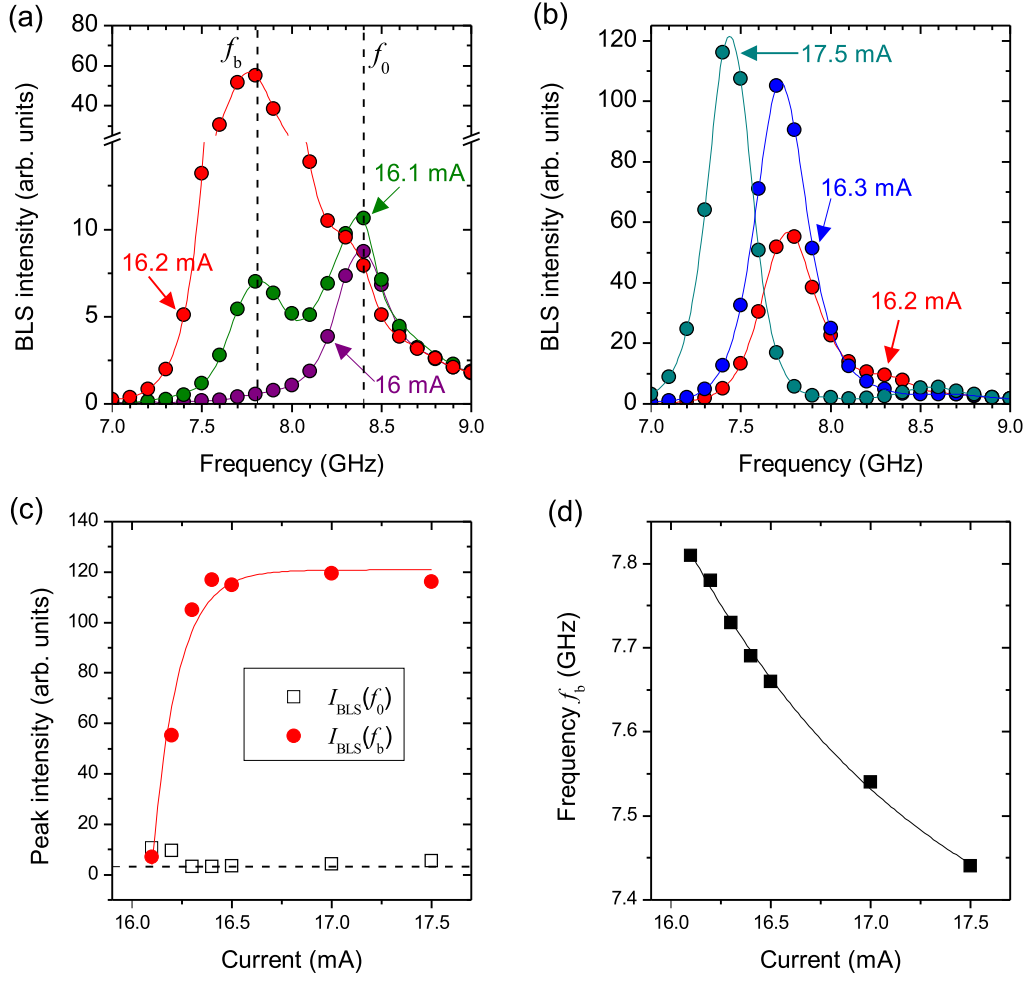


Figure 4.31: BLS investigations of the spin-current induced instability in the SHNO. (a) BLS spectra for currents I close to the instability at $I_c = 16.1$ mA. (b) BLS spectra for currents $I > I_c$. (c) Peak intensities $I_{BLS}(\omega_0)$, and $I_{BLS}(\omega_b)$ as a function of the current. Continuous line as a guide to the eye. Dashed line marks minimum $I_{BLS}(\omega_0)$. (d) Dependence of ω_b on I . Line as a guide to the eye.

Spatial properties

The spatial profile of the BLS intensity $I_{BLS}(\omega, \mathbf{r})$ at $I = 16$ mA $< I_c$ ($\omega = \omega_0$) and $I > I_c$ ($\omega = \omega_b$) is shown in Figure 4.32. Before the instability develops, the dynamics is enhanced within the gap (see Fig. 4.32(a)). Due to radiation, the dynamic profile shows a distribution, which is in the x -direction larger than the gap size. A Gaussian function with a FWHM of $\sigma_x = 810(40)$ nm describes

the lateral extend in this direction. In the other direction, the determined $\sigma_y = 309(6)$ nm essentially reflects that inside the gap, the intensity of the dynamics is approximately constant. As the current exceeds the threshold $I_c = 16.1$ mA, the dynamics changes qualitatively not only in the frequency-space, but also in real space. Figure 4.32(b) shows that now the dynamic profile is much stronger concentrated inside the gap. The FWHM of $\sigma_x = 271(5)$ nm ($\sigma_y = 238(6)$ nm) implies that the actual size (after deconvolution with a Gaussian representing the laser spot) is less than 100 nm. This rough estimate will be further refined in conjunction with the discussion of a micromagnetic simulation of the SHNO in section 4.3.4. When further increasing the current, the lateral size increases slightly (see Fig. 4.32(c) and (d)).

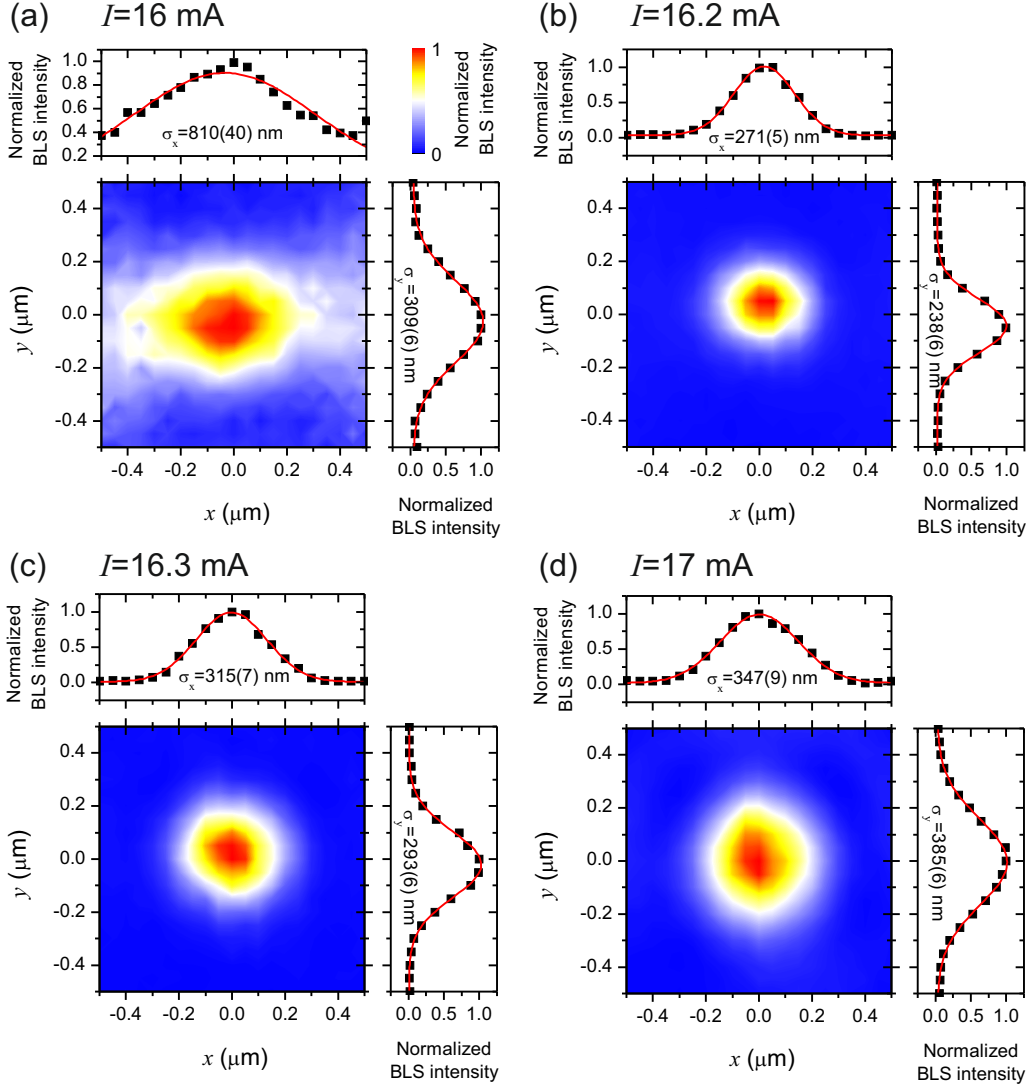


Figure 4.32: Spatially resolved BLS intensity for different currents (background from zero current subtracted). Central sections along \mathbf{e}_x and \mathbf{e}_y were fitted by Gaussian functions (red line), yielding the FWHM $\sigma_{x,y}$ as indicated. (a) $I = 16 \text{ mA} < I_c$, BLS intensity measured at frequency ω_0 . Above the current threshold, the shown BLS profiles were measured at $\omega_b < \omega_0$: (b) $I = 16.2 \text{ mA} > I_c$, (c) $I = 16.3 \text{ mA} > I_c$, and (d) $I = 17 \text{ mA} > I_c$.

Field dependence

I will now discuss the field dependence of the observed instability. The influence of the magnitude and the relative orientation of the field on the oscillation frequency ω_b and on the critical current I_c can be seen in Figure 4.33. The angle θ is defined as the angle between \mathbf{H} and $\mathbf{e}_y \parallel -\mathbf{j}_c$.

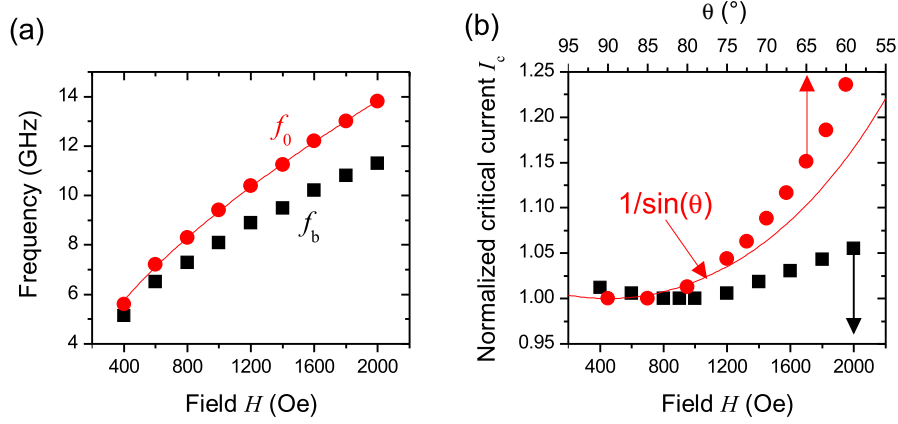


Figure 4.33: (a) Field dependence of the frequency $f_b = \omega_b/2\pi$ of the unstable mode at $I = I_c$ in comparison to the FMR frequency $f_0 = \omega_0/2\pi$. (b) Field (angular) dependence of the critical current I_c at $\theta = 90^\circ$ ($H = 900$ Oe), normalized to the critical current $I_c = 16.1$ mA at $\theta = 90^\circ$ and $H = 900$ Oe. The continuous red curve $f(\theta) = \sin^{-1} \theta$ approximately describes the angular dependence.

For $\theta = 90^\circ$, the oscillation frequency ω_b of the unstable mode is distinctively below the FMR frequency ω_0 for $400 \leq H \leq 2$ kOe, as shown in Figure 4.33(a). The frequency separation increases with increasing field. Reversal of the field ($\theta = -90^\circ$) or reversal of the current flow direction totally suppresses the dynamics. When fixing the field to $H = 900$ Oe, the critical current I_c increases with decreasing θ . These observations demonstrate that the spin current generated in the SHNO obeys the symmetry expected from the spin Hall effect.

In particular the angular dependence of I_c can be understood, when considering the polarization \mathbf{p} of the spin current in the gap. If we rotate the frame of reference with the field, the polarization direction, and the gap orientation changes. It was shown in chapter 2.3.2 that for $\mathbf{p} \parallel -\mathbf{H}$, the spin-transfer torque $\tau_{STT} \parallel -\tau_G$. Thus precessional motion will be enhanced. If we consider an angle $\theta \neq 90^\circ$, the damping-like part of $\tau_{STT} \propto \sin \theta$ decreases. In order to maintain the damping compensation, the current has to increase proportional to $\sin^{-1} \theta$. This simple picture holds down to $\theta = 75^\circ$, as can be seen in Figure 4.33(b).

Interpretation of the unstable mode

The spectral and spatial properties clearly indicate what kind magnetic mode goes unstable in the SHNO. First-of-all, the frequency ω_b is below the bottom of the usual spin-wave spectrum. The unstable mode can not be part of the latter. The spatial measurements show a strong localization of the auto-oscillation mode on

a scale of 100 nm. The most convincing interpretation is that also in the SHNO, a standing spin-wave bullet [111] mode is excited. Of course the experimental technique has only a limited spatial resolution. Thus the spatial features remain partially obscured. Apart from this, one may object against the interpretation of a bullet mode that the temperature gradient, and the inhomogeneous internal magnetic field also can give rise to a localized spin-wave mode. In order to clarify these issues, a micromagnetic model of the SHNO will be discussed in the following.

4.3.4 Micromagnetic model

The calculated spin-current distribution and polarization are taken as scalar and vectorial input fields for the STT-term Eq.(2.36) in a micromagnetic model implemented in MuMax2 [128]. Within this model, only the Py layer is taken into account. The 5 nm thick Py disc with a diameter of 4 μm is discretized into 1024×1024 cells. The previously determined magnetic material parameters are adopted. The same spin-Hall angle of $\phi_H = 0.07$ as for the previous calculations is assumed. The Oersted field \mathbf{H}_{Oe} caused by the charge current is added to the external field \mathbf{H} . The simulation is carried out at 0 K.

Transient dynamics

Switching on the charge current in the simulation, drives the magnetic system into a non-equilibrium state. For small currents the system does not show persistent oscillations. Only a reconfiguration of the static magnetization due to the STT and the Oersted field can be seen. When exceeding a minimum current of about $I_S = 22.75$ mA, a spin-wave instability is enabled. The dynamic mode which goes unstable is not a bullet mode. Instead one sees a Slonczewski-like spin-wave mode [115] (S-mode), with frequency $\omega_S/2\pi = 10.1$ GHz $\approx \omega_{\text{bottom}}/2\pi$, and wave length $\lambda \approx 200$ nm in the x -direction. Due to the anisotropy of the spin-wave dispersion, the wavelength in the y -direction $\lambda_y > \lambda_x$ is much larger. In fact, no oscillation can be seen at all, implying that the wave is overdamped in this direction. Because of the damping compensation by the STT, the amplitude of the S-mode increases in time. In Figure 4.34(a) the trajectory (red line) of the magnetization vector \mathbf{M} (yellow), probed in the center of the SHNO's gap, is plotted on a unit sphere. The starting point close to the x -axis is marked by a small yellow sphere. The depicted trajectory spans 5 ns, during which the S-mode grows, and finally the system switches into a different dynamic state, characterized by large angle oscillations around the negative x -axis.

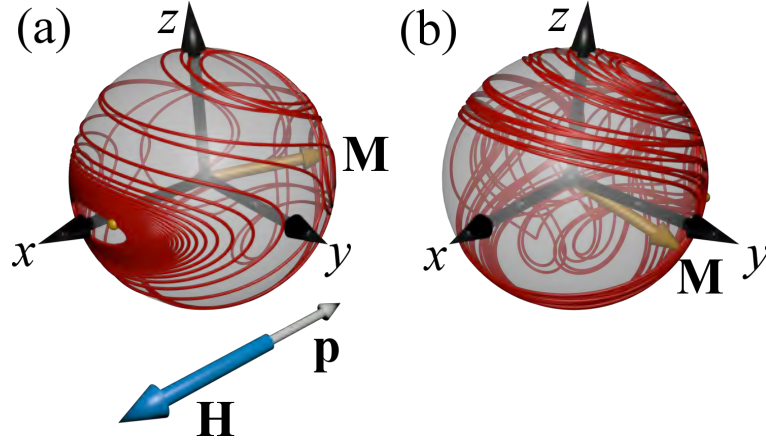


Figure 4.34: (a) Transient dynamics for $I = 23 \text{ mA}$, $H = 1200 \text{ Oe}$. The amplitude of the initially excited S-mode grows until the system switches into a different oscillation mode. (b) Stationary oscillations, after dynamic phase transition and subsequent reduction of the current to $I = 20 \text{ mA}$.

The dynamic phase transition takes place, when the precession angle reaches a magnitude of $\phi = 90^\circ$. After this, the dominant oscillation mode is a spin-wave bullet mode. The S-mode vanishes totally. When further increasing or decreasing the current, the bullet mode persists. The initially observed S-mode does not appear again. This peculiar dynamic behaviour, termed subcriticality, is for example discussed in reference [18] in the context of a micromagnetic simulation of a conventional STNO. Not being part of the linear spin-wave spectrum is the basic reason, why one cannot excite a bullet directly from equilibrium. Before the bullet appears, a certain level of dynamic agitation is mandatory. In the real experiment carried out at room temperature, the STT-enhanced thermal activation of the magnetic system might be sufficient to allow a direct bullet formation. In the numeric simulation at 0 K, the S-mode serves as a dynamic seed for the bullet. In Figure 4.34(b) the trajectory of the magnetization vector after the phase transition is shown. One can clearly see that the STT pushes \mathbf{M} away from the positive, towards the negative x -direction. The final dynamic state is evidently not a simple limit cycle, as expected from a single coherent mode, but a more complex superposition of at least two modes.

In [18] it is shown that within a certain current interval ΔI around I_S the S-mode can be the only stable solution. This was not observed in the simulation discussed here. One reason is that in this simulation non-linear damping, as proposed for example in [121], is neglected.²¹ If the non-linear magnon-magnon

²¹ Theoretically it might be possible to see a stable (not growing) S-mode also without non-linear

interactions, promoting e.g. non-linear damping due to Suhl instability, are too weak, the STT-induced instability grows without limitation.

Stationary dynamics

When the bullet mode is established in the simulation, it is in fact always accompanied by a second mode. A typical power spectrum for $I = 20$ mA, and $H = 1200$ Oe is shown in Figure 4.35(a). Two dominant peaks at frequencies $\omega_b/2\pi = 8.235$ GHz and $\omega_h/2\pi = 9.881$ can be seen. Both are below the FMR frequency $\omega_0/2\pi = 10.25$ GHz. As I will show in the following, the dynamical mode causing the peak at frequency ω_b resembles the experimentally observed bullet mode, and will be referred to as such from now on. The second mode with frequency ω_h was not found in the BLS experiments discussed in this thesis. In addition to these two modes, the spectrum also shows several smaller peaks. When varying experimental parameters (field or current), the frequencies ω_n of these peaks are always equidistant with $\omega_n = \omega_b + n(\omega_h - \omega_b)$. This clearly shows that the dynamics at these frequencies result from a non-linear frequency multiplication effect.

damping. The numerical investigations of the SHNO discussed here, show that if such a dynamic phase exists, the current interval $\Delta I < 0.1$ mA. In [18] it was shown that the current interval ΔI increases when taking non-linear damping into account.

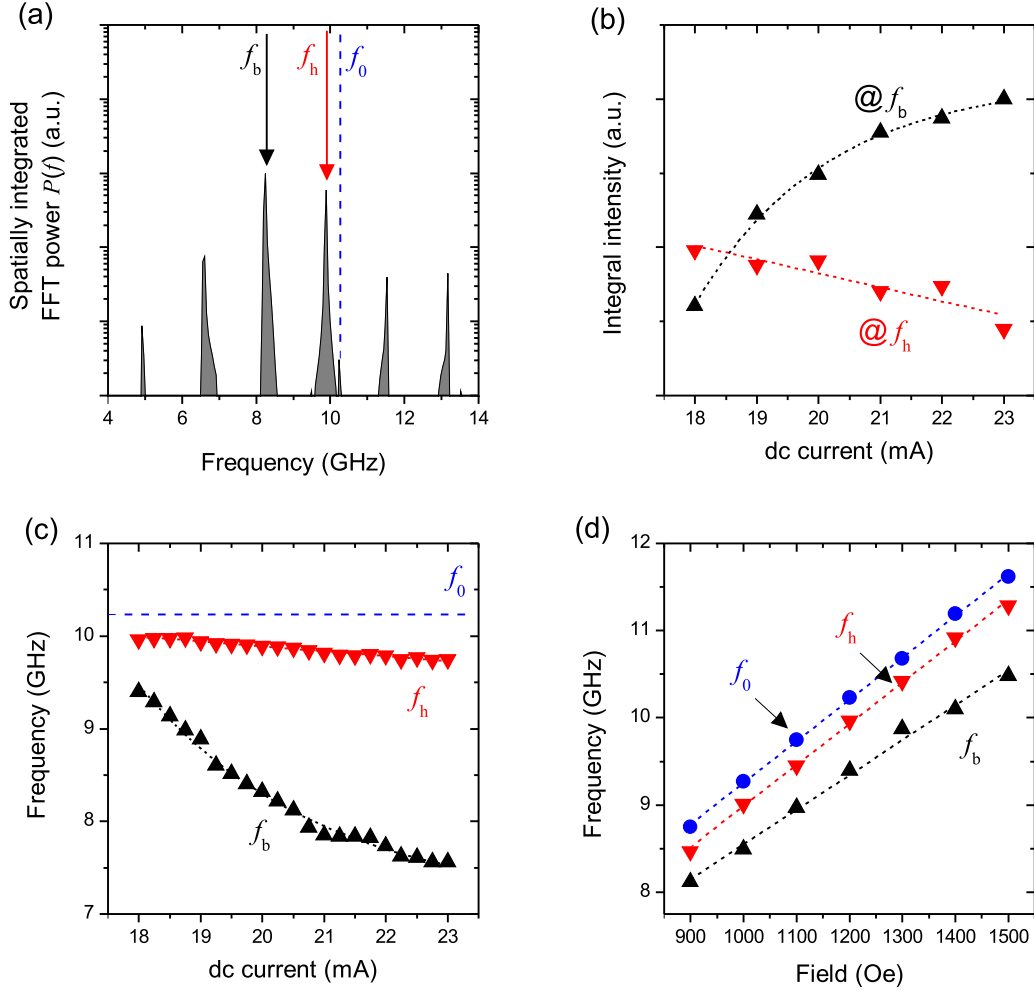


Figure 4.35: Spectral characteristics of the simulated auto-oscillations in the SHNO. (a) Power spectrum for $I = 20$ mA, and $H = 1200$ Oe. (b) Current dependence of the integral intensity (grey areas in (a)). (c) Current dependence of the auto-oscillation frequencies f_b and f_h at $H = 1200$ Oe. (d) Field dependence of the auto-oscillation frequencies f_b and f_h at smallest current possible, before the modes vanish.

The integral intensity of the spectral peak associated with the bullet mode increases monotonously with the current, as shown in Figure 4.35(b). For large currents a gradual saturation of the integral intensity can be seen. In contrast in the experiment, a fast saturation was found (see Figure 4.31(c)). The integral intensity of the second mode decreases linearly with current. Note that for the smallest current, the bullet mode is less prominent than the second auto-oscillation mode.

The mode with frequency ω_b displays current and field characteristics similar to the experimentally observed bullet mode. In particular the current dependence of $f_b = \omega_b/2\pi$ shown in Figure 4.35(c) has a negative slope $\frac{df_b}{dI} \approx 0.8 \text{ GHz/mA}$, which is comparable to the experimental value of 0.5 GHz/mA . The frequency ω_h of the second mode is contrast almost independent of the current.

In Figure 4.35(d) the field dependence of the auto-oscillation frequencies is shown. For a given field, the current was set to the smallest value possible, before the auto-oscillations vanish. Note that if this happens, always both modes disappear. As a function of the field, the frequency of the bullet is always distinctively below the FMR frequency. Similar to the experimental findings, the frequency separation increases with increasing H . The frequency of the second mode stays closely below the FMR frequency as function of H . In contrast to the bullet mode, the separation stays constant. Note that the properties of the second mode comply with findings reported in [78]. There a similar SHNO as here was investigated by means of microwave spectroscopy.

Spatial properties

The experimentally obtained BLS maps $I_{BLS}(\omega, \mathbf{r})$ will now be compared to simulated power maps $P(\omega, \mathbf{r})$. The power map of the bullet mode is shown in Figure 4.36(a). The central sections reveal a FWHM of $\sigma_x = 78 \text{ nm}$ ($\sigma_y = 66 \text{ nm}$). The profile shows a shallow minimum in the center. The surrounding maxima are located on the x -axis at a distance of approximately 20 nm from the center. As a function of the field, the FWHM decreases significantly, as shown in 4.36(c) for σ_x . This increased localization complies with the increased frequency separation to the FMR mode: the further the bullet's frequency is detached from the frequencies of the linear spin waves, the stronger the bullet is confined. As a function of the current, the FWHM shows no clear trend (see 4.36(d)), apart from a small increase. Recall that in the experiment, such a small increase in the lateral size was observed. According to theory [111] developed for STNOs, one would expect a decrease in the lateral extend with increasing current, and thus decreasing frequency. One reason why this cannot be seen in the SHNO is the simultaneously increasing lateral region, where the STT overcomes the instability threshold. To summarize, the typical lateral extend of the bullet in terms of the FWHM is about 80 nm . This supports the experimental estimate of about 100 nm .

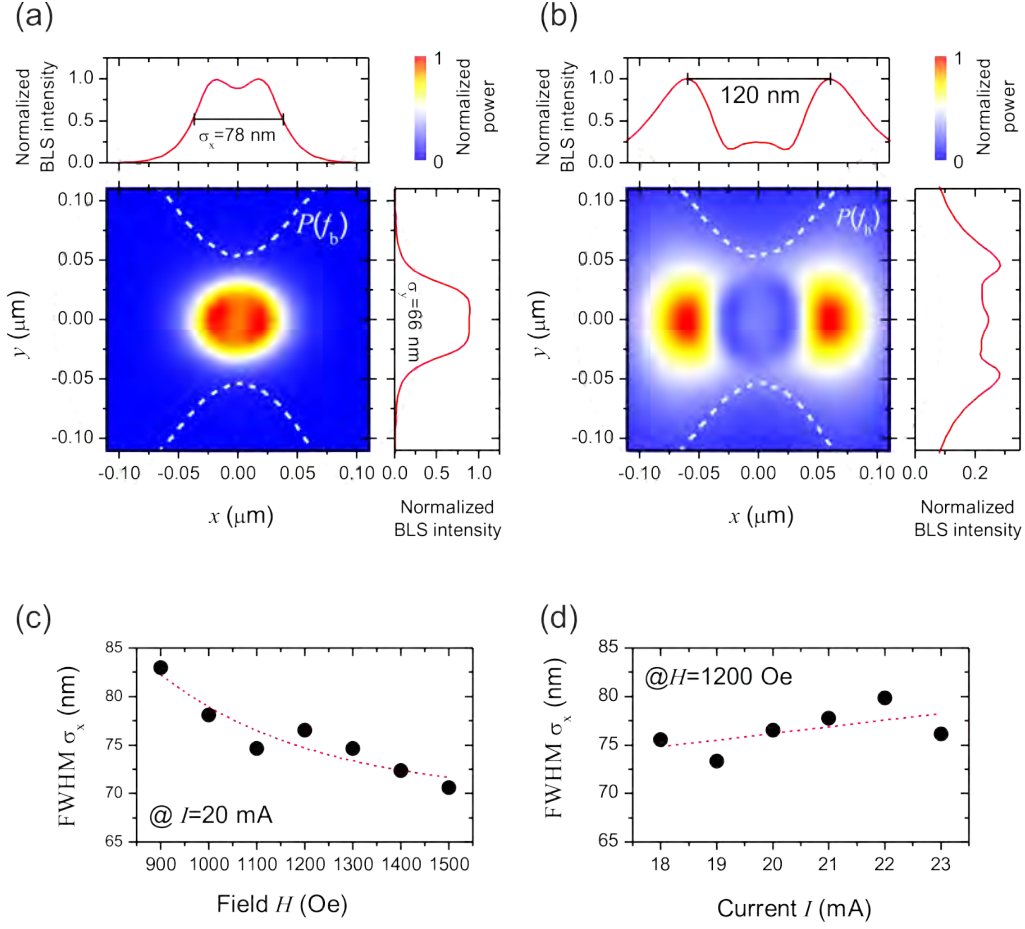


Figure 4.36: Spatial characteristics of the simulated auto-oscillation modes. (a) Bullet mode. (b) Second mode. (c) Dependence of the FWHM σ_x on the field H , at $I = 20 \text{ mA}$. (d) Dependence of the FWHM σ_x on the current I , at $H = 1200 \text{ Oe}$.

The second auto-oscillation mode shown in 4.36(b) has a different dynamic profile than the bullet. Note that for better visibility, the power map is normalized to its maximum. In comparison with the bullet, the maximum power is one order of magnitude smaller. The two maxima on the x -axis are located 60 nm away from the center. A discussion of the nature of this mode follows further below.

The power map of the bullet mode characterizes the dynamic part of the bullet. As I will show now, the double peak feature in the dynamic part can be related to the static part. To access the latter, one can inspect the time-averaged magnetization component $\langle m_x \rangle_t$ shown in Figure 4.37. The additionally shown central sections through this magnetization profile are complemented by corresponding sections through the bullet's dynamic profile $P(\omega_b)$. In contrast to the dynamic

part of the bullet, the static part decays monotonously for all radial directions.

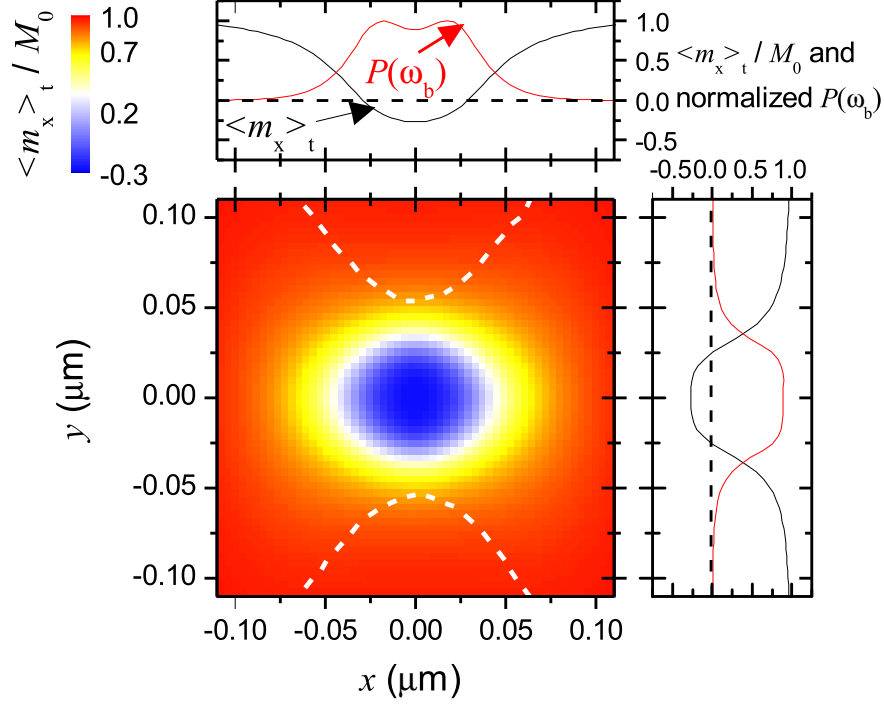


Figure 4.37: Time averaged magnetization, characterizing the static part of the bullet (inner panel). The central sections (outer panels) also contain sections through the profiles $P(\omega_b)$ of the bullet mode.

As the sections in Figure 4.37 show, the oscillation of the bullet is strongest, where the average magnetization vanishes. Vanishing of the average magnetization implies an average precessional angle of exactly 90° . In the center a partial reversal of the magnetization to $\langle m_x \rangle_t = -0.2M_0$ is established. For this, the precession angle has to exceed 90° . Therefore, the bullets dynamics is strongest not in the center, but where $\langle m_x \rangle_t = 0$. In the extremal case of full magnetization reversal in the center, the dynamic part would totally vanish.

The strong modification of the magnetization caused by the bullet gives rise to a significant change in the internal magnetic field. The internal field $H_{int} = \langle H_{eff,x} \rangle_t$, computed by time-averaging the effective field, is shown in Figure 4.38. There one can see that the magnetization reversal caused by the bullet gives rise to a strong increase of the internal field inside the bullet's core, and to a local minimum outside the core. The additional sections through the mode profile P_{ω_h}

of the secondary mode show that this mode is localized in the minima of the internal field.

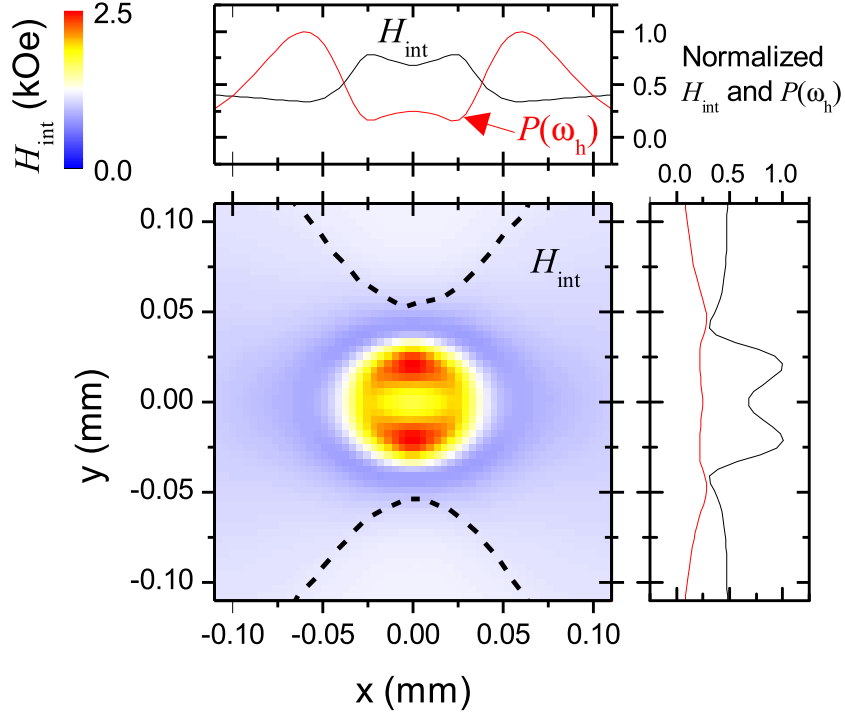


Figure 4.38: Time averaged internal field, characterizing the static part of the bullet (inner panel). The central sections (outer panels) also contain sections through the profile $P(\omega_h)$ of the secondary auto-oscillation modes.

Role of temperature and Oersted field

It was shown previously that Joule heating is relatively weak in the discussed SHNO. To check, whether the dynamics are qualitatively different, when including this effect, a proper random fluctuation term in the LLGS equation was included in the simulation. An inhomogeneous, stationary temperature distribution as shown in Figure 4.27 was assumed. The simulation was carried out exemplarily for a single set of typical experimental parameters ($H = 1200$ Oe, $I = 20$ mA). Apart from changing the linewidth of the auto-oscillation modes, no other significant qualitative change was observed in the corresponding spectrum. Still, two different modes, and equidistant peaks resulting from frequency multiplication can be seen in the spectrum.

In STNOs, the relatively large Oersted field H_{Oe} strongly influences the dynamics. In particular it was shown in [34] that regarding the secondary auto-oscillation mode in STNOs, the localization properties depend on the spatial dependence of H_{Oe} . The computation for the SHNO instead suggests that in SHNOs, the Oersted field is less important. Indeed, even when completely neglecting H_{Oe} , the secondary mode still exists, and displays qualitatively the same spectral and spatial features. This confirms that the localization of the secondary auto-oscillation mode in SHNOs is dominated by the dipolar field created by the bullet mode.

4.3.5 Discussion

The discussed experiments demonstrate that spin-currents generated by the spin-Hall effect can be strong enough to induce a spin-wave instability. For this, a local spin-current injection is mandatory, as implemented by the design of the spin-Hall nano-oscillator. Experiment, theory, and simulation leave no doubt that the unstable mode is a standing spin-wave bullet [111]. Although this mode is believed to be the dominant auto-oscillation mode in standard, tangentially magnetized spin-torque oscillators, no direct mapping is possible in such devices. The electrical contacts which provide the (spin-polarized) current always overshadow the area, where the bullet is localized. So far only numerical modelling of such devices allowed to investigate the spatial properties of the bullet [18, 9, 19, 34]. The planar structure of the SHNO provides direct optical access to the active area. The two-dimensional mode profiles shown in Figure 4.32 and published in [28] represent the first direct evidence of a standing spin-wave bullet mode in a Py film, sustained by a spin current.

Role of radiative losses

Similar to standard spin-torque oscillator, in the SHNO radiative losses limit the amplitudes of short-wavelength exchange modes. This mechanism is elucidated by the analytic modelling of the BLS spectra, done for currents below the instability threshold. Based on the fluctuation-dissipation-theorem, the model incorporates the interaction of the spin current with the magnetic system, and the actual measurement process. In the supplement 5.1 the same approach is applied to a simpler situation - to the structure with global spin current injection discussed in [27]. In both cases, the model provides a reasonable description of the experimental data. The most interesting difference when comparing the analysis of the device with global spin-current injection with the analysis of the SHNO, is the different impact of the spin current on α . For the former device α increases by more than 40%,

which suppresses the instability. In contrast for the SHNO an increase of α of only 9% was derived. These numbers quantify the qualitative argument given in [27], and emphasize the decisive benefit of radiative losses, which enable a spin-current induced instability in the SHNO.

Simulation

The simulation shows that spin-wave dynamics in SHNOs is not limited to the bullet mode. It was shown that an additional mode coexists with the bullet. This mode is localized in the inhomogeneous internal field created by the bullet. The characteristics of this mode comply with observations in SHNOs by microwave spectroscopy published in [78]. A similar mode was also found in simulations [34] of STNOs.²² With these non-propagating auto-oscillation modes, a technologically interesting synchronization of adjacent SHNOs is not possible. The large amplitudes of both modes give in the numerical experiment rise to a frequency multiplication effect. The resulting spectral peaks lie above the FMR frequency, and thus represent in real space propagating waves, which might be useful for synchronization.

As a transient phenomenon in the simulation, a Slonczewski-like propagating mode was found. Such an S-mode is known to be able to mediate synchronization. Considering the experimental data, the divergence of the integral intensity and the failure of the analytic model prior to the appearance of the bullet mode, leaves a small current interval, in which the system is already unstable. The numerical simulation suggests that the unstable mode is the S-mode. Evidently, in the real experiment, non-linear damping takes place. This implies that the S-mode can be a stable solution.

Relation to overpopulation in confined elements

In the discussion of the overpopulation process, it was shown that the overpopulated mode resembles a standing spin-wave bullet, at least for microwave powers and dynamic fields h not too far above the threshold. The non-linear features (huge dynamic amplitude, localization, sub-criticality) are naturally explained by this interpretation.

The bullet observed in the SHNO has very similar properties. In both cases, the frequencies are below, or close to the bottom of the spin-wave spectrum. In case of the confined element, the frequency ω_b of the bullet is very close to

²² There it is misleadingly termed 'propagating', because when forcing the magnetization to point out-of-plane, the frequency of this mode increases above FMR, and radiation sets in.

$\omega_{bottom} \approx \omega_0$. The typical size of 290 nm is larger than for the bullet in the SHNO, where a typical size of 100 nm was determined. This complies with the theory [111], which also predicts a stronger confinement, with increasing distance to ω_0 .

The amplitude of the bullet, as reflected by the average magnetization in the center, is in the confined element with $M_{eff} = 0.5M_0$ smaller than in the SHNO. There the magnetization is on average not only reduced but even reversed, so that $M_{eff} = -0.2M_0$ is reached. The dispersion Eq.(2.44) can be written in terms of the amplitude $B_0 \propto 1 - M_{eff}/M_0$ (see Eq.(6) in [111]):

$$\omega_b(B_0) = \omega_0 + NB_0^2, \quad (4.11)$$

where $N < 0$ is the non-linearity coefficient. Thus, the smaller the amplitude, the closer is the frequency ω_b to ω_0 , as found here experimentally.

In the confined element, certain aspects of the overpopulation resemble a BEC formation. Remarkably, in the SHNO the transformation of the power spectral density for currents approaching the instability threshold shown in Fig. 4.29, appears to be similar to the magnon BEC formation in YIG [30]. Mathematically, this can be seen directly by inspection of the occupation factor n . In the presence of a spin current, the argument of the exponential function in Eq.(4.5) can be written as

$$\frac{\hbar\omega}{k_B T} \frac{\omega_{r,mn} + R_{mn} - \beta}{\omega_{r,mn} + R_{mn}} \equiv \frac{\hbar\omega - \mu}{k_B T}, \quad (4.12)$$

with $\mu = \frac{k_B T \beta}{\omega_{r,mn} + R_{mn}}$. In this respect, the spin-current induced enhancement of thermal magnetic fluctuations is formally closely related with the formation of a magnon BEC. The difference to magnon BECs in YIG is that the STT not only modifies the occupation factor, but also the linewidth of each mode. Furthermore, the chemical potential is different for each mode. Finally, the overpopulated magnon state in the SHNO - the bullet mode - is not part of the linear spin-wave spectrum. In contrast the the magnon BEC in YIG is formed by the bottom spin-wave mode.

Chapter 5

Supplement

5.1 Thermal magnetic fluctuations in a device with uniform spin current injection

Prior to the experiments discussed in chapter 4.3, experimental investigations [27, 26, 38] carried out in our laboratories focussed on device structures, in which a uniform spin current is injected into a confined ferromagnetic structure. Figure 2.7 shows a sketch of such a device. The analytic model (Eq. (4.7) modified according to Eqs. (4.9) and (4.8)) describing the STT enhanced thermal fluctuations, is considerably simpler for such a structure. No radiative losses have to be taken into account, and no electrodes mask the ferromagnet. The prefactor β of the STT term can be directly calculated, based on the Pt stripline geometry - no assumptions about an effective β related to the probing laser spot are necessary.

I will now refer to the experimental data presented in Ref. [27]. For this device, the Pt stripline has a thickness of $t_{Pt} = 10$ nm and a width of $w = 2.8$ μm . The Py disc on top has a radius of 1 μm , and a thickness of $t_{Py} = 5$ nm. For a given current I , β follows from:

$$\beta = \frac{I}{wt_{Pt}} \frac{\phi_H g \mu_B}{2eM_0 t_{Py}}. \quad (5.1)$$

The spin Hall angle is as before in this thesis assumed to be $\phi_H = 0.07$. In [27], the Oersted field was shown to depend linearly on the current with a slope of 2.14 Oe mA^{-1} . It was shown in this thesis that in the SHNO, the Joule heating can be safely neglected. This does not hold for the structure considered here: numerical calculation based on a COMSOL model shows that for $I = 28$ mA, a temperature increase of $\Delta T = 80$ K can be expected. The dependence of ΔT on the current is shown in Figure 5.1. It can be fitted by second order polynomial function (continuous line). The contribution from Joule heating is taken into account by substitution of $T + \Delta T$ for T in Eq. (4.8).

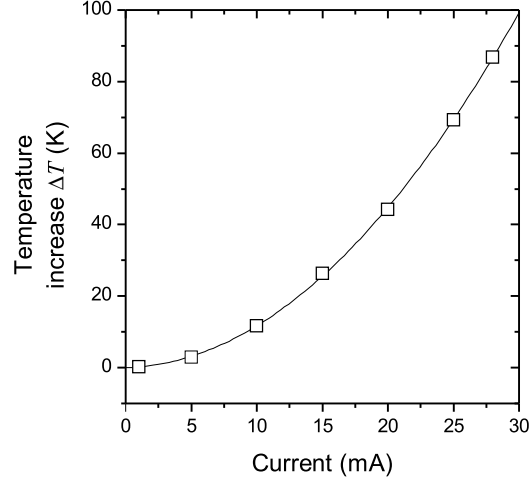


Figure 5.1: Joule heating in a device with uniform spin-current injection. Open symbols show the numerically calculated temperature increase ΔT as a function of the current, based on a COMSOL model. Continuous line is a second order polynomial function, fitted to the numerical data.

Two parameters remain to be adjusted in order to fit the analytic model to the spectra, shown in Figure 5.2. These are the damping constant α and the magnetization M_0 . To fit the spectrum for $I = 0$ mA, a saturation magnetization of $M_0 = 7.350$ kG (standard value is 10 kG), and $\alpha = 0.02$ has to be assumed. The relatively small value of the saturation magnetization indicates a bad quality of the Py used in this device. The large value for α is typical for Py on Pt (see [4, 77]).

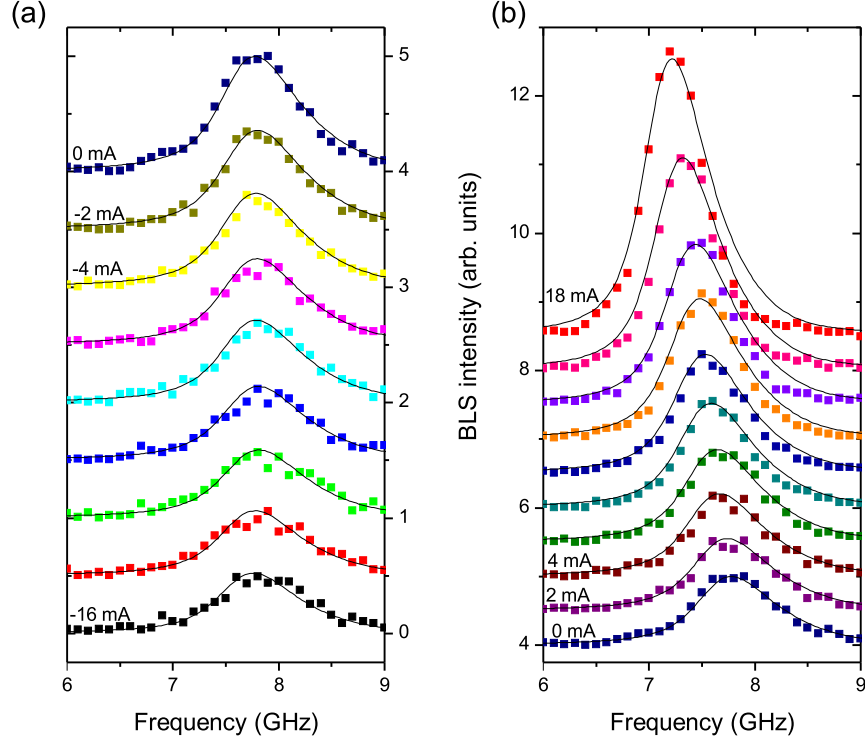


Figure 5.2: Thermally activated magnetic fluctuations in a device with uniform spin current injection. BLS spectra (coloured symbols) from [27] are shown in (a) for negative current, and in (b) for positive current. Solid lines were obtained by fitting the analytic model to this experimental data. For better visibility, the individual spectra are shifted vertically.

Fits for negative currents, when the magnetic fluctuations are suppressed, are shown in Figure 5.2(a). Down to $I = -16$ mA, the data can be well described by the model (for currents $I < -16$ mA, the BLS signal gets too noisy). The fitting parameters are shown in Figure 5.3. The small decrease of the magnetization for increasingly negative currents complies with the increase in temperature due to Joule heating. The decrease in α will be explained later.

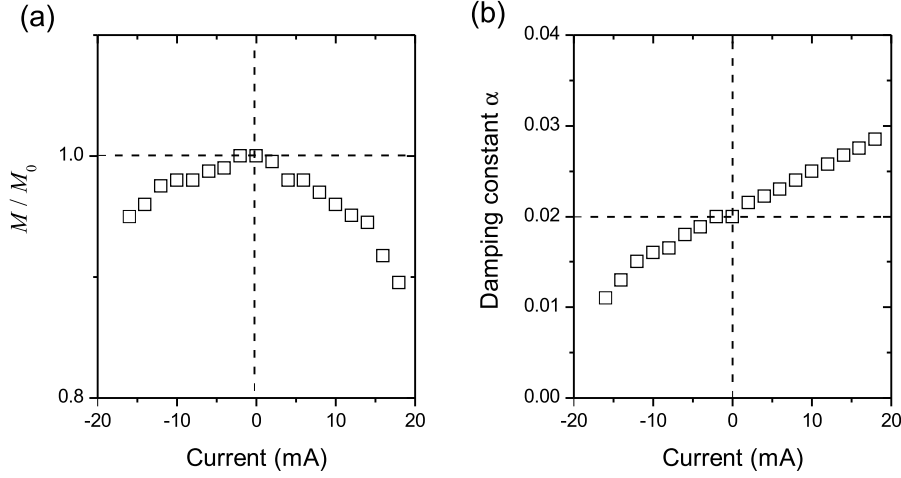


Figure 5.3: (a) Current dependence of the magnetization M and (b) of the damping constant α , determined from the fits shown in Figure 5.2.

For positive currents, the magnetic fluctuations are enhanced. The analytic model is able to capture this effect up to $I = 18$ mA. Then it begins to fail. First of all, the trailing edge is slightly overestimated. At $I > 20$ mA (data not shown), the model can only reproduce the peak intensity with reasonable parameters. In [27] it was shown that in this regime, the integral intensity saturates. The interpretation given in [27] was that scattering with exchange modes increases the damping of the dipolar modes, preventing their instability. The current dependence of the fitted damping constant α , shown in Figure 5.3(b), supports this picture. It strongly increases when approaching large positive currents. The decrease of the magnetization is now caused by Joule heating, and the negative non-linear frequency shift due to STT. For negative currents α instead decreases. This complies with the assumption that for this current polarity, the scattering of the dipolar modes is reduced.

A more qualitative understanding of the reason, why the damping constant is proportional to the current, can be obtained by considering the temperature dependence of the four-particle process, in which two conduction electrons and two magnons interact without spin-flip. These processes dominate magnetic relaxation in metallic ferromagnets like Py. It was shown theoretically (see Eq.(10) in [82])

that the corresponding relaxation frequency

$$\omega_r \propto k_B T \ln \frac{k_B T}{\hbar \omega} \quad (5.2)$$

Here, we ignore the current dependence of the magnetization. For small enough currents, this is reasonable. Let us assume that all modes participating in the scattering process have approximately the same effective temperature $T_{SHE} = T \frac{\Gamma_0}{\Gamma_0 - \beta}$. As a first approximation the losses $\Gamma_0 = \omega_r(\beta = 0)$. Substituting T_{SHE} for T in Eq.(5.2) directly yields a monotonous dependence of $\alpha \propto \omega_r$ on the current. This simplistic argument emphasizes that a complete understanding demands a truly microscopic theory, which is beyond the scope of this thesis.

In summary, the model introduced to describe thermal magnetic fluctuations, enhanced by a local spin current injection in SHNOs, can be simplified in order to describe devices with uniform spin current injection. In both situations, a good agreement is possible up to the (suppressed) onset of instability processes.

Bibliography

- [1] G. S. Abo, Y. Hong, J. Park, J. Lee, W. Lee, and B. Choi. Definition of magnetic exchange length. *Magnetics, IEEE Transactions on*, 49(8):4937–4939, 2013. Cited on p. 6.
- [2] M. Althammer, S. Meyer, H. Nakayama, M. Schreier, S. Altmannshofer, M. Weiler, H. Huebl, S. Geprägs, M. Opel, R. Gross, D. Meier, C. Klewe, T. Kuschel, J. Schmalhorst, G. Reiss, L. Shen, A. Gupta, Y. Chen, G. E. W. Bauer, E. Saitoh, and S. T. B. Goennenwein. Quantitative study of the spin hall magnetoresistance in ferromagnetic insulator/normal metal hybrids. *Phys. Rev. B*, 87:224401, Jun 2013. Cited on p. 25.
- [3] P. W. Anderson and H. Suhl. Instability in the motion of ferromagnets at high microwave power levels. *Phys. Rev.*, 100:1788–1789, Dec 1955. Cited on p. 3, 20.
- [4] K. Ando, S. Takahashi, K. Harii, K. Sasage, J. Ieda, S. Maekawa, and E. Saitoh. Electric manipulation of spin relaxation using the spin hall effect. *Phys. Rev. Lett.*, 101:036601, Jul 2008. Cited on p. 2, 85, 87, 105.
- [5] W. J. Antel, M. M. Schwickert, Tao Lin, W. L. O’Brien, and G. R. Harp. Induced ferromagnetism and anisotropy of pt layers in fe/pt(001) multilayers. *Phys. Rev. B*, 60:12933–12940, Nov 1999. Cited on p. 25.
- [6] M. N. Baibich, J. M. Broto, A. Fert, F. Nguyen Van Dau, and F. Petroff. Giant Magnetoresistance of (001)Fe/(001)Cr Magnetic Superlattices. *Physical Review Letters*, 61:2472–2475, 1988. Cited on p. 1.
- [7] M. Bauer, O. Büttner, S. O. Demokritov, B. Hillebrands, V. Grimalsky, Yu. Rapoport, and A. N. Slavin. Observation of spatiotemporal self-focusing of spin waves in magnetic films. *Phys. Rev. Lett.*, 81:3769–3772, Oct 1998. Cited on p. 30.

- [8] C. Bayer, J. P. Park, H. Wang, M. Yan, C. E. Campbell, and P. A. Crowell. Spin waves in an inhomogeneously magnetized stripe. *Physical Review B*, 69:134401, 2004. Cited on p. 10.
- [9] D. V. Berkov and N. L. Gorn. Magnetization oscillations induced by a spin-polarized current in a point-contact geometry: Mode hopping and nonlinear damping effects. *Phys. Rev. B*, 76:144414, Oct 2007. Cited on p. 101.
- [10] G. Binasch, P. Grünberg, F. Saurenbach, and W. Zinn. Enhanced magnetoresistance in layered magnetic structures with antiferromagnetic interlayer exchange. *Physical Review B*, 39:4828–4830, 1989. Cited on p. 1.
- [11] F. Bloch. Zur theorie des ferromagnetismus. *Zeitschrift für Physik*, 61(3-4):206–219, 1930. Cited on p. 4.
- [12] N. Bloembergen and R. W. Damon. Relaxation effects in ferromagnetic resonance. *Phys. Rev.*, 85:699–699, Feb 1952. Cited on p. 3, 20.
- [13] N. Bloembergen and S. Wang. Relaxation effects in *Para* - and ferromagnetic resonance. *Phys. Rev.*, 93:72–83, Jan 1954. Cited on p. 3, 20.
- [14] M. Buchmeier, H. Dassow, D. E. Bürgler, and C. M. Schneider. Intensity of brillouin light scattering from spin waves in magnetic multilayers with noncollinear spin configurations: Theory and experiment. *Phys. Rev. B*, 75:184436, May 2007. Cited on p. 34.
- [15] O. Büttner, M. Bauer, S. O. Demokritov, B. Hillebrands, M. P. Kostylev, B. A. Kalinikos, and A. N. Slavin. Collisions of spin wave envelope solitons and self-focused spin wave packets in yttrium iron garnet films. *Phys. Rev. Lett.*, 82:4320–4323, May 1999. Cited on p. 30.
- [16] A. V. Chumak, P. Pirro, A. A. Serga, M. P. Kostylev, R. L. Stamps, H. Schultheiss, K. Vogt, S. J. Hermsdoerfer, B. Laegel, P. A. Beck, and B. Hillebrands. Spin-wave propagation in a microstructured magnonic crystal. *Applied Physics Letters*, 95(26):262508, 2009. Cited on p. 2.
- [17] J. F. Cochran. Brillouin light scattering intensities for patterned magnetic thin films. *Journal of Magnetism and Magnetic Materials*, 212(1-2):40–52, 2000. Cited on p. 35.
- [18] G. Consolo, B. Azzerboni, G. Gerhart, G. A. Melkov, V. Tiberkevich, and A. N. Slavin. Excitation of self-localized spin-wave bullets by spin-polarized

- current in in-plane magnetized magnetic nanocontacts: A micromagnetic study. *Phys. Rev. B*, 76:144410, Oct 2007. Cited on p. 30, 94, 95, 101.
- [19] G. Consolo, B. Azzerboni, L. Lopez-Diaz, G. Gerhart, E. Bankowski, V. Tiberkevich, and A. N. Slavin. Micromagnetic study of the above-threshold generation regime in a spin-torque oscillator based on a magnetic nanocontact magnetized at an arbitrary angle. *Phys. Rev. B*, 78:014420, Jul 2008. Cited on p. 101.
- [20] M. G. Cottam and D. J. Lockwood. *Light Scattering in Magnetic Solids*. A Wiley-Interscience Publication, 1986. Cited on p. 31.
- [21] R. W. Damon and J. R. Eshbach. Magnetostatic modes of a ferromagnetic slab. *Journal of Physics and Chemistry of Solids*, 19:308–320, 1961. Cited on p. 6, 7, 34.
- [22] R. E. De Wames and T. Wolfram. Dipole-exchange spin waves in ferromagnetic films. *Journal of Applied Physics*, 41(3):987–993, 1970. Cited on p. 6.
- [23] V. E. Demidov, H. Ulrichs, S. O. Demokritov, and S. Urazhdin. Nonlinear scattering in nanoscale magnetic elements: Overpopulation of the lowest-frequency magnon state. *Phys. Rev. B*, 83:020404, Jan 2011. Cited on p. 41, 55, 62.
- [24] V. E. Demidov, H. Ulrichs, S. V. Gurevich, S. O. Demokritov, V. S. Tiberkevich, A. N. Slavin, A. Zholud, and S. Urazhdin. Synchronization of spin hall nano-oscillators to external microwave signals. *Nat Commun*, 5:–, January 2014. Cited on p. 78.
- [25] V. E. Demidov, S. Urazhdin, and S. O. Demokritov. Direct observation and mapping of spin waves emitted by spin-torque nano-oscillators. *Nature Materials*, 9:984–988, 2010. Cited on p. 2, 28, 29, 62.
- [26] V. E. Demidov, S. Urazhdin, E. R. J. Edwards, and S. O. Demokritov. Wide-range control of ferromagnetic resonance by spin hall effect. *Applied Physics Letters*, 99(17):172501, 2011. Cited on p. 2, 27, 104.
- [27] V. E. Demidov, S. Urazhdin, E. R. J. Edwards, M. D. Stiles, R. D. McMichael, and S. O. Demokritov. Control of magnetic fluctuations by spin current. *Phys. Rev. Lett.*, 107:107204, Sep 2011. Cited on p. 24, 27, 28, 88, 101, 102, 104, 106, 107.

- [28] V. E. Demidov, S. Urazhdin, H. Ulrichs, V. Tiberkevich, A. N. Slavin, D. Baither, G. Schmitz, and S. O. Demokritov. Magnetic nano-oscillator driven by pure spin current. *Nature Materials*, 11(12):1028–1031, December 2012. Cited on p. 2, 78, 87, 101.
- [29] S. O. Demokritov and V. E. Demidov. Micro-brillouin light scattering spectroscopy of magnetic nanostructures. *Magnetics, IEEE Transactions on*, 44(1):6–12, 2008. Cited on p. 3, 32.
- [30] S. O. Demokritov, V. E. Demidov, O. Dzyapko, G. A. Melkov, A. A. Serga, B. Hillebrands, and A. N. Slavin. Bose-einstein condensation of quasi-equilibrium magnons at room temperature under pumping. *Nature*, 443:430, 2006. Cited on p. 23, 64, 103.
- [31] S. O. Demokritov, B. Hillebrands, and A. N. Slavin. Brillouin light scattering studies of confined spin waves: linear and nonlinear confinement. *Physics Reports*, 348(6):441 – 489, 2001. Cited on p. 30.
- [32] S. O. Demokritov and A. N. Slavin, editors. *Magnonics*. Springer Berlin Heidelberg, 2013. Cited on p. 1.
- [33] M. J. Donahue and D. G. Porter. OOMMF User’s Guide, Version 1.0, Interagency Report NISTIR 6376. Technical report, National Institute of Standards and Technology, Gaithersburg, MD, 1999. Cited on p. viii.
- [34] R. K. Dumas, E. Iacocca, S. Bonetti, S. R. Sani, S. M. Mohseni, A. Eklund, J. Persson, O. Heinonen, and Johan Åkerman. Spin-wave-mode coexistence on the nanoscale: A consequence of the oersted-field-induced asymmetric energy landscape. *Phys. Rev. Lett.*, 110:257202, Jun 2013. Cited on p. 101, 102.
- [35] M. I. Dyakonov and V. I. Perel. Current-induced spin orientation of electrons in semiconductors. *Physics Letters A*, 35(6):459 – 460, 1971. Cited on p. 2, 23.
- [36] O. Dzyapko, V. E. Demidov, S. O. Demokritov, G. A. Melkov, and V. L. Safonov. Monochromatic microwave radiation from the system of strongly excited magnons. *Applied Physics Letters*, 92:162510, 2008. Cited on p. 23.
- [37] E. R. J. Edwards, M. Buchmeier, V. E. Demidov, and S. O. Demokritov. Magnetostatic spin-wave modes of an in-plane magnetized garnet-film disk. *Journal of Applied Physics*, 113:103901, 2013. Cited on p. 51.

-
- [38] E. R. J. Edwards, H. Ulrichs, V. E. Demidov, S. O. Demokritov, and S. Urazhdin. Parametric excitation of magnetization oscillations controlled by pure spin current. *Phys. Rev. B*, 86:134420, Oct 2012. Cited on p. 2, 27, 66, 104.
- [39] M. Faraday. On a peculiar class of acoustical figures; and on certain forms assumed by groups of particles upon vibrating elastic surfaces. *Philosophical Transactions of the Royal Society of London*, 121:299–340, 1831. Cited on p. 15.
- [40] Z. Feng, J. Hu, L. Sun, B. You, D. Wu, J. Du, W. Zhang, A. Hu, Y. Yang, D. M. Tang, B. S. Zhang, and H. F. Ding. Spin hall angle quantification from spin pumping and microwave photoresistance. *Phys. Rev. B*, 85:214423, Jun 2012. Cited on p. 25.
- [41] A. Fert. Magnetic and transport properties of metallic multilayers. *Materials Science Forum*, 59-60:439, 1991. Cited on p. 2.
- [42] A. Fert, V. Cros, and J. Sampaio. Skyrmions on the track. *Nat Nano*, 8(3):152–156, March 2013. Cited on p. 1.
- [43] T. L. Gilbert. A phenomenological theory of damping in ferromagnetic materials. *IEEE Transactions on Magnetism*, 40:3443–3449, 2004. Cited on p. 8.
- [44] S. Gliga, A. Kákay, R. Hertel, and O. G. Heinonen. Spectral analysis of topological defects in an artificial spin-ice lattice. *Phys. Rev. Lett.*, 110:117205, Mar 2013. Cited on p. 39.
- [45] G. Gubbiotti, G. Carlotti, T. Okuno, M. Grimsditch, L. Giovannini, F. Montoncello, and F. Nizzoli. Spin dynamics in thin nanometric elliptical permalloy dots: A brillouin light scattering investigation as a function of dot eccentricity. *Phys. Rev. B*, 72:184419, Nov 2005. Cited on p. 35.
- [46] G. Y. Guo, S. Murakami, T.-W. Chen, and N. Nagaosa. Intrinsic spin hall effect in platinum: First-principles calculations. *Phys. Rev. Lett.*, 100:096401, Mar 2008. Cited on p. 24.
- [47] A. G. Gurevich and G. A. Melkov. *Magnetization Oscillations and Waves*. CRC Press, 1996. Cited on p. 20, 46, 76.

- [48] K. Y. Guslienko, S. O. Demokritov, B. Hillebrands, and A. N. Slavin. Effective dipolar boundary conditions for dynamic magnetization in thin magnetic stripes. *Phys. Rev. B*, 66:132402, Oct 2002. Cited on p. 10.
- [49] C. Hahn, G. de Loubens, O. Klein, M. Viret, V. V. Naletov, and J. Ben Youssef. Comparative measurements of inverse spin hall effects and magnetoresistance in yig/pt and yig/ta. *Phys. Rev. B*, 87:174417, May 2013. Cited on p. 25.
- [50] J. Hamrle, J. Pistora, B. Hillebrands, B. Lenk, and M. Münzenberg. Analytical expression of the magneto-optical kerr effect and brillouin light scattering intensity arising from dynamic magnetization. *Journal of Physics D: Applied Physics*, 43(32):325004, 2010. Cited on p. 34.
- [51] C. Herring and C. Kittel. On the theory of spin waves in ferromagnetic media. *Phys. Rev.*, 81:869–880, Mar 1951. Cited on p. 5.
- [52] J. E. Hirsch. Spin hall effect. *Phys. Rev. Lett.*, 83:1834–1837, Aug 1999. Cited on p. 2, 23.
- [53] A. Hoffmann. Spin hall effects in metals. *Magnetics, IEEE Transactions on*, 49(10):5172–5193, 2013. Cited on p. 2, 24.
- [54] T. Holstein and H. Primakoff. Field dependence of the intrinsic domain magnetization of a ferromagnet. *Phys. Rev.*, 58:1098–1113, Dec 1940. Cited on p. 4.
- [55] S. Y. Huang, X. Fan, D. Qu, Y. P. Chen, W. G. Wang, J. Wu, T. Y. Chen, J. Q. Xiao, and C. L. Chien. Transport magnetic proximity effects in platinum. *Phys. Rev. Lett.*, 109:107204, Sep 2012. Cited on p. 25.
- [56] J. Jorzick, S.O. Demokritov, C. Mathieu, B. Hillebrands, B. Bartenlian, C. Chappert, F. Rousseaux, and A.N. Slavin. Brillouin light scattering from quantized spin waves in micron sized magnetic wires. *Physical Review B*, 60(22):15194–15200, 1999. Cited on p. 35.
- [57] R. I. Joseph and E. Schömann. Demagnetizing Field in Nonellipsoidal Bodies. *Journal of Applied Physics*, 36:1579–1593, 1965. Cited on p. 9, 12, 67.
- [58] J. D. Jouannopoulos, S. G. Johnson, J. N. Winn, and R. D. Meade. *Photonic Crystals: Molding the Flow of Light*. Princeton University Press, 2. edition, 2008. Cited on p. 1.

-
- [59] Yu. D. Kalafati and V. L. Safonov. Theory of quasiequilibrium effects in a system of magnons excited by incoherent pumping. *JETP Letters*, 73:1511, 1991. Cited on p. 22.
- [60] B. A. Kalinikos and A. N. Slavin. Theory of dipole-exchange spin wave spectrum for ferromagnetic films with mixed exchange boundary conditions. *Journal of Physics C: Solid State Physics*, 19:7013–7033, 1986. Cited on p. 6, 7, 10, 55, 60.
- [61] J. A. Katine, F. J. Albert, R. A. Buhrman, E. B. Myers, and D. C. Ralph. Current-driven magnetization reversal and spin-wave excitations in co/cu/co pillars. *Phys. Rev. Lett.*, 84:3149–3152, Apr 2000. Cited on p. 2.
- [62] Y. K. Kato, R. C. Myers, A. C. Gossard, and D. D. Awschalom. Observation of the spin hall effect in semiconductors. *Science*, 306:1910, 2004. Cited on p. 23.
- [63] A. Khitun, M. Bao, and K. L. Wang. Magnonic logic circuits. *Journal of Physics D: Applied Physics*, 43(26):264005, 2010. Cited on p. 2.
- [64] S. Kim. Micromagnetic computer simulations of spin waves in nanometre-scale patterned magnetic elements. *Journal of Physics D: Applied Physics*, 43(26):264004, 2010. Cited on p. 39.
- [65] S. I. Kiselev, J. C. Sankey, I. N. Krivorotov, N. C. Emley, R. J. Schoelkopf, R. A. Buhrman, and D. C. Ralph. Microwave oscillations of a nanomagnet driven by a spin-polarized current. *Nature*, 425(6956):380–383, September 2003. Cited on p. 2.
- [66] C. Kittel. On the theory of ferromagnetic resonance absorption. *Phys. Rev.*, 73:155–161, Jan 1948. Cited on p. 6.
- [67] M. Krawczyk and H. Puzskarski. Plane-wave theory of three-dimensional magnonic crystals. *Physical Review B*, 77:054437, 2008. Cited on p. 1.
- [68] I. N. Krivorotov, N. C. Emley, J. C. Sankey, S. I. Kiselev, D. C. Ralph, and R. A. Buhrman. Time-domain measurements of nanomagnet dynamics driven by spin-transfer torques. *Science*, 307(5707):228–231, 2005. Cited on p. 2.
- [69] P. Krivosik, N. Mo, S. Kalarickal, and C. E. Patton. Hamiltonian formalism for two magnon scattering microwave relaxation: Theory and applications. *Journal of Applied Physics*, 101(8):083901, 2007. Cited on p. 77.

- [70] V. V. Kruglyak, S. O. Demokritov, and D. Grundler. Magnonics. *Journal of Physics D: Applied Physics*, 43(26):260301, 2010. Cited on p. 1.
- [71] V. V. Kruglyak, P. S. Keatley, A. Neudert, R. J. Hicken, J. R. Childress, and J. A. Katine. Imaging collective magnonic modes in 2d arrays of magnetic nanoelements. *Phys. Rev. Lett.*, 104:027201, Jan 2010. Cited on p. 2.
- [72] A. V. Lavrinenko, V. S. L’vov, G. A. Melkov, and V. B. Cherepanov. Kinetic instability of a strongly nonequilibrium system of spin waves and tunable radiation of a ferrite. *Zh. Eksp. Teor. Fiz.*, 81:1022, 1981. Cited on p. 22.
- [73] A. V. Lavrinenko, G. A. Melkov, and A. Yu. Taranenko. Kinetic instability of spin waves under arbitrary pumping conditions. *Sov. Phys. Solid State*, 26:910, 1984. Cited on p. 22.
- [74] E. M. Lifshitz and L. P. Pitajewski. *Lehrbuch der theoretischen Physik IX: Statistische Physik Teil 2*. Akademie Verlag GmbH Berlin, 4. edition, 1992. Cited on p. 5.
- [75] M. J. Lighthill. Contributions to the theory of waves in non-linear dispersive systems. *IMA Journal of Applied Mathematics*, 1(3):269–306, 1965. Cited on p. 30.
- [76] W. L. Lim, N. Ebrahim-Zadeh, J. C. Owens, H. G. E. Hentschel, and S. Urazhdin. Temperature-dependent proximity magnetism in pt. *Applied Physics Letters*, 102(16):162404, 2013. Cited on p. 25.
- [77] L. Liu, T. Moriyama, D. C. Ralph, and R. A. Buhrman. Spin-torque ferromagnetic resonance induced by the spin hall effect. *Phys. Rev. Lett.*, 106:036601, Jan 2011. Cited on p. 2, 25, 85, 87, 105.
- [78] R. H. Liu, W. L. Lim, and S. Urazhdin. Spectral characteristics of the microwave emission by the spin hall nano-oscillator. *Phys. Rev. Lett.*, 110:147601, Apr 2013. Cited on p. 2, 97, 102.
- [79] N. Locatelli, V. Cros, and J. Grollier. Spin-torque building blocks. *Nat Mater*, 13(1):11–20, January 2014. Cited on p. 2.
- [80] L. Lopez-Diaz, G. Aurelio, L. Torres, E. Martinez, M. A. Hernandez-Lopez, J. Gomez, O. Alejos, M. Carpentieri, G. Finocchio, and G. Consolo. Micro-magnetic simulations using graphics processing units. *Journal of Physics D: Applied Physics*, 45(32):323001, 2012. Cited on p. 39.

-
- [81] V. S. Lutovinov, G. A. Melkov, A. Yu. Taranenko, and V. B. Cherepanov. Kinetic instability of first order spin waves in ferrite. *JETP Letters*, 68:760, 1989. Cited on p. 22.
- [82] V. S. Lutovinov and M. Yu. Reizer. Relaxation processes in ferromagnetic metals. *JETP*, 50:355, 1979. Cited on p. 107.
- [83] V. S. L'vov. *Wave Turbulence Under Parametric Excitation*. Springer-Verlag Berlin Heidelberg New York, 1994. Cited on p. 15, 18, 22.
- [84] M. Madami, S. Bonetti, G. Consolo, S. Tacchi, G. Carlotti, G. Gubbiotti, F. B. Mancoff, M. A. Yar, and J. Akerman. Direct observation of a propagating spin wave induced by spin-transfer torque. *Nat Nano*, 6(10):635–638, October 2011. Cited on p. 28.
- [85] A. Manchon. Spin hall effect versus rashba torque: a diffusive approach. 2012. Cited on p. 25.
- [86] F. B. Mancoff, N. D. Rizzo, B. N. Engel, and S. Tehrani. Phase-locking in double-point-contact spin-transfer devices. *Nature*, 437(7057):393–395, September 2005. Cited on p. 2.
- [87] M. Mansuripur and R. Giles. Demagnetizing field computation for dynamic simulation of the magnetization reversal process. *Magnetics, IEEE Transactions on*, 24(6):2326–2328, 1988. Cited on p. 39.
- [88] R. D. McMichael and M. D. Stiles. Magnetic normal modes of nanoelements. *Journal of Applied Physics*, 97:10J901, 2005. Cited on p. 40, 42.
- [89] R. D. McMichael, D. J. Twisselmann, and A. Kunz. Localized ferromagnetic resonance in inhomogeneous thin films. *Phys. Rev. Lett.*, 90:227601, Jun 2003. Cited on p. 77.
- [90] G. A. Melkov, V. L. Safonov, A. Yu. Taranenko, and S. V. Sholom. Kinetic instability and bose condensation of nonequilibrium magnons. *Journal of Magnetism and Magnetic Materials*, 132(1-3):180 – 184, 1994. Cited on p. 22.
- [91] G. A. Melkov and D. V. Slobodianiuk. A strongly nonequilibrium state in magnetic nanodots at high pumping levels. *Ukr. J. Phys.*, 58:189–194, 2013. Cited on p. 22, 41, 63.

- [92] S. Mühlbauer, B. Binz, F. Jonietz, C. Pfleiderer, A. Rosch, A. Neubauer, R. Georgii, and P. Böni. Skyrmion lattice in a chiral magnet. *Science*, 323(5916):915–919, 2009. Cited on p. 1.
- [93] O. Mosendz, V. Vlaminck, J. E. Pearson, F. Y. Fradin, G. E. W. Bauer, S. D. Bader, and A. Hoffmann. Detection and quantification of inverse spin hall effect from spin pumping in permalloy/normal metal bilayers. *Phys. Rev. B*, 82:214403, Dec 2010. Cited on p. 25.
- [94] A. H. Nayfeh and D. T. Mook. *Parametrically Excited Systems*, chapter 5, pages 258–364. Wiley-VCH Verlag GmbH, 2007. Cited on p. 15.
- [95] A. V. Nazarov, C. E. Patton, R. G. Cox, L. Chen, and P. Kabos. General spin wave instability theory for anisotropic ferromagnetic insulators at high microwave power levels. *Journal of Magnetism and Magnetic Materials*, 248(2):164 – 180, 2002. Cited on p. 21.
- [96] S. Neusser, B. Botters, and D. Grundler. Localization, confinement, and field-controlled propagation of spin waves in $\text{Ni}_{80}\text{Fe}_{20}$. *Physical Review B*, 78:054406, 2008. Cited on p. 1, 2.
- [97] S. Neusser and D. Grundler. Magnonics: Spin Waves on the Nanoscale. *Advanced Materials*, 21:1–6, 2009. Cited on p. 1.
- [98] P. Nowik-Boltyk, O. Dzyapko, V. E. Demidov, N. G. Berloff, and S. O. Demokritov. Spatially non-uniform ground state and quantized vortices in a two-component bose-einstein condensate of magnons. *Nature Scientific Reports*, 2:482, 2012. Cited on p. 23.
- [99] L. Nowotny and B. Hecht. *Principles of Nano-Optics*. Cambridge University Press, 2007. Cited on p. 34.
- [100] H. M. Olson, P. Krivosik, K. Srinivasan, and C. E. Patton. Ferromagnetic resonance saturation and second order suhl spin wave instability processes in thin permalloy films. *Journal of Applied Physics*, 102(2):023904, 2007. Cited on p. 62, 76, 77.
- [101] C. Pai, L. Liu, Y. Li, H. W. Tseng, D. C. Ralph, and R. A. Buhrman. Spin transfer torque devices utilizing the giant spin hall effect of tungsten. *Applied Physics Letters*, 101(12):122404, 2012. Cited on p. 25.

-
- [102] C. Pappas, E. Lelièvre-Berna, P. Falus, P. M. Bentley, E. Moskvina, S. Grigoriev, P. Fouquet, and B. Farago. Chiral paramagnetic skyrmion-like phase in mnsi. *Phys. Rev. Lett.*, 102:197202, May 2009. Cited on p. 1.
- [103] M. R. Pufall, W. H. Rippard, S. E. Russek, S. Kaka, and J. A. Katine. Electrical measurement of spin-wave interactions of proximate spin transfer nanooscillators. *Phys. Rev. Lett.*, 97:087206, Aug 2006. Cited on p. 2.
- [104] G. Rado and J. Weertman. Spin-wave resonance in a ferromagnetic metal. *Journal of Physics and Chemistry of Solids*, 11:315–333, 1959. Cited on p. 6.
- [105] J. O. Rantschler, R. D. McMichael, A. Castillo, A. J. Shapiro, W. F. Egelhoff, B. B. Maranville, D. Pulugurtha, A. P. Chen, and L. M. Connors. Effect of 3d, 4d, and 5d transition metal doping on damping in permalloy thin films. *Journal of Applied Physics*, 101(3):033911, 2007. Cited on p. 73.
- [106] W. H. Rippard, M. R. Pufall, S. Kaka, S. E. Russek, and T. J. Silva. Direct-current induced dynamics in $\text{Co}_{90}\text{Fe}_{10}/\text{Ni}_{80}\text{Fe}_{20}$ point contacts. *Phys. Rev. Lett.*, 92:027201, Jan 2004. Cited on p. 2, 28.
- [107] J. R. Sandercock. Trends in brillouin scattering: Studies of opaque materials, supported films, and central modes. In M. Cardona and G. Güntherodt, editors, *Light Scattering in Solids III*, volume 51 of *Topics in Applied Physics*, pages 173–206. Springer Berlin Heidelberg, 1982. Cited on p. 36.
- [108] Klaus D. Sattler, editor. *Handbook of Nanophysics: Functional Nanomaterials*. CRC Press, 2011. Cited on p. 26.
- [109] P. Seibt. Parametric excitation of spin waves in permalloy nanoellipses. Master’s thesis, WWU Muenster, 2012. Cited on p. 66, 68.
- [110] Y. Silberberg. Collapse of optical pulses. *Opt. Lett.*, 15(22):1282–1284, Nov 1990. Cited on p. 29, 30.
- [111] A. N. Slavin and V. Tiberkevich. Spin wave mode excited by spin-polarized current in a magnetic nanocontact is a standing self-localized wave bullet. *Phys. Rev. Lett.*, 95:237201, Nov 2005. Cited on p. 2, 29, 93, 97, 101, 103.
- [112] A. N. Slavin and V. Tiberkevich. Nonlinear auto-oscillator theory of microwave generation by spin-polarized current. *Magnetism, IEEE Transactions on*, 45(4):1875–1918, 2009. Cited on p. 88.

- [113] A. N. Slavin and V. S. Tiberkevich. Localized spin-wave modes excited by spin-polarized current. In S.O. Demokritov, editor, *Spin Wave Confinement*. Pan Stanford Publishing Pte. Ltd., 2009. Cited on p. 29.
- [114] J. C. Slonczewski. Current-driven excitation of magnetic multilayers. *Journal of Magnetism and Magnetic Materials*, 159(1-2):L1 – L7, 1996. Cited on p. 25.
- [115] J. C. Slonczewski. Excitation of spin waves by an electric current. *Journal of Magnetism and Magnetic Materials*, 195(2):L261 – L268, 1999. Cited on p. 29, 93.
- [116] J. Smit. The spontaneous hall effect in ferromagnetics {II}. *Physica*, 24(1-5):39–51, 1958. Cited on p. 24.
- [117] N. Smith. Modeling of thermal magnetization fluctuations in thin-film magnetic devices. *Journal of Applied Physics*, 90(11):5768–5773, 2001. Cited on p. 84.
- [118] H. Suhl. The theory of ferromagnetic resonance at high signal powers. *Journal of Physics and Chemistry of Solids*, 1(4):209 – 227, 1957. Cited on p. 3, 14, 20, 46.
- [119] H. Suhl. Note on the saturation of the main resonance in ferromagnetics. *Journal of Applied Physics*, 30:1961, 1959. Cited on p. 46.
- [120] S. Tacchi, M. Madami, G. Gubbiotti, G. Carlotti, H. Tanigawa, T. Ono, and M. P. Kostylev. Anisotropic dynamical coupling for propagating collective modes in a two-dimensional magnonic crystal consisting of interacting squared nanodots. *Phys. Rev. B*, 82:024401, Jul 2010. Cited on p. 2.
- [121] V. Tiberkevich and A. N. Slavin. Nonlinear phenomenological model of magnetic dissipation for large precession angles: Generalization of the gilbert model. *Phys. Rev. B*, 75:014440, Jan 2007. Cited on p. 28, 30, 61, 94.
- [122] H. Ulrichs, V. E. Demidov, and S. O. Demokritov. Micromagnetic study of auto-oscillation modes in spin-hall nano-oscillators. *Applied Physics Letters*, 104(4):042407, 2014. Cited on p. 78.
- [123] H. Ulrichs, V. E. Demidov, S. O. Demokritov, W. L. Lim, J. Melander, N. Ebrahim-Zadeh, and S. Urazhdin. Optimization of pt-based spin-hall-effect spintronic devices. *Applied Physics Letters*, 102(13):132402, 2013. Cited on p. 25.

-
- [124] H. Ulrichs, V. E. Demidov, S. O. Demokritov, A. V. Ognev, M. E. Stebliy, L. A. Chebotkevich, and A. S. Samardak. Linear and nonlinear collective modes in magnetic microstructures formed by coupled disks. *Phys. Rev. B*, 83:184403, May 2011. Cited on p. 61.
- [125] H. Ulrichs, V. E. Demidov, S. O. Demokritov, and S. Urazhdin. Parametric excitation of eigenmodes in microscopic magnetic dots. *Phys. Rev. B*, 84:094401, Sep 2011. Cited on p. 66.
- [126] H. Ulrichs, V. E. Demidov, S. O. Demokritov, and S. Urazhdin. Spin-torque nano-emitters for magnonic applications. *Applied Physics Letters*, 100(16):162406, 2012. Cited on p. 2, 62.
- [127] S. O. Valenzuela and M. Tinkham. Direct electronic measurement of the spin hall effect. *Nature*, 442:176, 2006. Cited on p. 23.
- [128] A. Vansteenkiste and B. Van de Wiele. Mumax: A new high-performance micromagnetic simulation tool. *Journal of Magnetism and Magnetic Materials*, 323(21):2585 – 2591, 2011. Cited on p. 39, 41, 93.
- [129] O. G. Vendik, B. A. Kalinikos, and D. N. Chartorizhskii. Instability of spin waves in tangentially magnetized ferromagnetic films. *Sov. Phys. Solid State*, 19:222, 1977. Cited on p. 7.
- [130] W. Wettling, M. G. Cottam, and J. R. Sandercock. The relation between one-magnon light scattering and the complex magneto-optic effects in yig. *Journal of Physics C: Solid State Physics*, 8(2):211, 1975. Cited on p. 31.
- [131] S. A. Wolf, D. D. Awschalom, R. A. Buhrman, J. M. Daughton, S. von Molnár, M. L. Roukes, A. Y. Chtchelkanova, and D. M. Treger. Spintronics: A spin-based electronics vision for the future. *Science*, 294(5546):1488–1495, 2001. Cited on p. 1.
- [132] J. Xiao and G. E. W. Bauer. Spin-wave excitation in magnetic insulators by spin-transfer torque. *Phys. Rev. Lett.*, 108:217204, May 2012. Cited on p. 25.
- [133] V. E. Zakharov, V. S. L’vov, and S. S. Starobinets. Stationary nonlinear theory of parametric excitation of waves. *Soviet Physics JETP*, 32:656–663, 1971. Cited on p. 15.

Bibliography

- [134] V. E. Zakharov, V. S. L’vov, and S. S. Starobinets. Spin-wave turbulence beyond the parametric excitation threshold. *Soviet Physics Uspekhi*, 17(6):896, 1975. Cited on p. 15.
- [135] S. Zhang. Spin hall effect in the presence of spin diffusion. *Phys. Rev. Lett.*, 85:393–396, Jul 2000. Cited on p. 25.

Danksagung

An dieser Stelle möchte ich allen danken, die es mir ermöglicht haben diese Arbeit anzufertigen. Als ich 2009 im Forschungszentrum Jülich zum ersten Mal S. O. Demokritov über seine Forschung vortragen hörte, war mir klar, dass ich sehr gerne in seiner Gruppe mitarbeiten würde. Für die tatsächliche Möglichkeit bin ich ihm sehr dankbar. Das praktische Handwerk konnte ich von V. E. Demidov lernen, dessen Methodik ich sehr zu schätzen weiß. Allen Mitarbeitern danke ich für tatkräftige Unterstützung bei der Forschungsarbeit, sowie für zahlreiche gute Gespräche, innerhalb und außerhalb eines wissenschaftlichen Kontextes. Zuletzt danke ich meiner Frau Hilke, die mich täglich motiviert und unterstützt, auch indem sie meinen Blick auf Wesentlicheres abseits der Physik zu lenken vermag.

Lebenslauf

Persönliche Daten

Name	Henning Ulrichs
Geburtsdatum	15.01.1984
Geburtsort	Oldenburg in Niedersachsen
Staatsangehörigkeit	Deutsch

Schulbildung

bis 06/2003	Teletta-Groß-Gymnasium, Leer Abschluss: allgemeine Hochschulreife Gesamtnote: 1,5 (sehr gut)
-------------	--

Zivildienst

07/2003 bis 04/2004	Individuelle Schwerbehindertenbetreuung Wohnstätte für Körperbehinderte des Vereins für Körperbehinderte e.V., Bunde
---------------------	--

Hochschulausbildung

10/2004 bis 03/2010	Studium der Physik an der Georg-August-Universität Göttingen Abschluss: Diplom-Physiker Gesamtnote: 1,0 (sehr gut)
---------------------	---

Promotionsstudium

10/2010 bis 04/2014	Studium am Institut für angewandte Physik der Westfälischen Wilhelms-Universität Münster, in der Arbeitsgruppe von Prof. Dr. S. O. Demokritov. Während dieser Zeit als wissenschaftlicher Mitarbeiter dort angestellt.
---------------------	--